MOTION COMPENSATION IN TURBO SPIN ECHO ANGIOGRAPHY

by

Jason Kraig Mendes

A dissertation submitted to the faculty of
The University of Utah
in partial fulfillment of the requirements for the degree of

Doctor of Philosophy

Department of Physics and Astronomy

The University of Utah

May 2011

The University of Utah Graduate School

STATEMENT OF DISSERTATION APPROVAL

The dissertation of **Jason Kraig Mendes**

has been approved by the following supervisory committee members:

Brian Saam	, Chair	**12/06/2010** Date Approved
Dennis L. Parker	, Member	**12/06/2010** Date Approved
Christoph Boehme	, Member	**12/06/2010** Date Approved
Gernot Laicher	, Member	**12/06/2010** Date Approved
Eun-Kee Jeong	, Member	**12/06/2010** Date Approved

and by **David Kieda**, Chair of the Department of **Physics and Astronomy**

and by Charles A. Wight, Dean of The Graduate School.

ABSTRACT

Each year in the United States, a quarter million cases of stroke are caused directly by atherosclerotic disease of the cervical carotid artery. This represents a significant portion of health care costs that could be avoided if high-risk carotid artery lesions could be detected early on in disease progression. There is mounting evidence that Magnetic Resonance Imaging of the carotid artery can better classify subjects who would benefit from interventions. Turbo Spin Echo sequences are a class of Magnetic Resonance Imaging sequences that provide a variety of tissue contrasts. While high resolution Turbo Spin Echo images have demonstrated important details of carotid artery morphology, it is evident that pulsatile blood and wall motion related to the cardiac cycle are still significant sources of image degradation. In addition, patient motion artifacts due to the relatively long scan times of Turbo Spin Echo sequences result in an unacceptable fraction of noninterpretable studies. This dissertation presents work done to detect and correct for types of voluntary and physiological patient motion.

To my wife and family who have been my greatest joy in life.

TABLE OF CONTENTS

LIST OF TABLES

ACKNOWLEDGMENTS

Foremost I am grateful to my wife and family for their support during my graduate studies. My supervisor, Dr. Dennis Parker, has been both knowledgeable and inspirational as a mentor in MR research. I appreciate the time invested by the rest of my committee, Dr. Brian Saam, Dr. Christoph Boehme, Dr. Gernot Laicher and Dr. E.K. Jeong. I had the pleasure to work with Dr. Seong-Eun Kim, Dr. Gerald Treiman, Dr. Eugene Kholmovski and Jordan Hulet as co-authors on several projects. In addition, Henry Buswell and Melody Johnson have been invaluable technicians in helping with our patient scans. This work has been supported by NIH grants HL48223 and HL57990, as well as grants from the Cumming Foundation, the Ben B. and Iris M. Margolis Foundation, and the Mark H. Huntsman Endowed Chair.

CHAPTER 1

INTRODUCTION

Each year in the United States, a quarter million cases of stroke are caused directly by atherosclerotic disease of the cervical carotid artery (1). This represents a significant portion of health care costs that could be avoided if high-risk carotid artery lesions could be detected early on in disease progression. There is mounting evidence that imaging the carotid artery can better classify subjects who would benefit from interventions (2-5). Although high resolution Turbo Spin Echo (TSE) images have demonstrated important details of carotid artery morphology, it is evident that pulsatile blood and wall motion related to the cardiac cycle are still significant sources of image degradation. In addition, patient motion artifacts that arise due to the relatively long scan times of TSE sequences may result in noninterpretable studies. This thesis presents work done to improve the diagnostic quality of Magnetic Resonance Imaging (MRI) by reducing the effects of patient motion.

This thesis is divided into seven chapters. Chapter 1 gives a brief overview of nuclear magnetic resonance and MRI. Chapter 2 describes the TSE sequence and some adaptations that are necessary when imaging the carotid artery. Basic pathology of carotid artery disease is also included. Images acquired with a TSE sequence are especially susceptible to artifacts caused by patient motion since they are acquired over a longer period of time than most other sequences. While many motion detection and

correction techniques for MRI have been proposed, their use is often limited by increased patient preparation, decreased patient comfort, additional scan time or the use of specialized sequences not available on many commercial scanners. For this reason we propose a simple self-navigating technique designed to detect motion in segmented sequences. One type of patient motion, rigid body translation, differs from most other types of motion in that it can be easily corrected during image reconstruction. An example of this type of motion might be a patient that lifts their head during a scan to get more comfortable. The detection and correction of this particular type of motion is described in Chapter 3. Another specific type of patient motion is in-plane rotation (such as small rotations of the head from side to side). Chapter 4 proposes an iterative technique to detect and quantify in-plane rotations. These two types of motion are very specific and account for only a small fraction of motion artifacts. More common types of voluntary motion include head nodding or swallowing. The correction of these types of motion are very difficult and the subject of numerous ongoing studies. However, even if correction is not an option, their detection is important so that corrupt data may be reacquired or removed prior to image reconstruction. This detection process is the focus of Chapter 5. In addition to voluntary motion, there are physiological types of motion such as cardiac motion. Since these types of motion are periodic in nature, it is possible to synchronize or gate the data acquisition to the patient's cardiac cycle. However, gating techniques are rarely used with TSE sequences because they increase scan time and produce other undesirable effects on image quality. Chapter 6 introduces a retrospective method of converting a conventional TSE acquisition into a cardiac cycle correlated cineTSE sequence. The cineTSE sequence generates a full sequence of images at each

slice location throughout the cardiac cycle in the same scan time that is conventionally used by standard TSE sequences to produce a single image at each slice location. Although much of this thesis utilizes a TSE sequence, the basic theory can be applied to other MRI sequences with little or no modifications. Conclusions and future work complete the dissertation in Chapter 7.

1.1 Nuclear Magnetic Resonance

Nuclear magnetic resonance (NMR) is a property where nuclei in a magnetic field absorb or radiate energy at a characteristic frequency. Electron spin resonance (ESR) and NMR differ fundamentally by the fact that the first considers unpaired electrons while the latter considers the atomic nucleus. Experiments with electron spin resonance are much more technically demanding than NMR, and ESR is not currently a viable method for clinical human applications (6). One of the earliest publications relating to NMR was by Isaac Isidor Rabi in 1939 (7). Rabi measured nuclear magnetic moments using an atomic beam and was awarded the 1944 Nobel Prize in Physics for his work. Despite this early work, the discovery of NMR is commonly credited to two independent groups working under Felix Bloch and Edward Purcell. In 1946, Bloch and Purcell published papers on the application of NMR to liquids (water) and solids (paraffin wax) respectively (8, 9). This work earned them the shared 1952 Nobel Prize in Physics. The following sections outline some basic principles of NMR with more detail found in sources (10-13).

1.1.1 Spin Magnetic Moment

Classical descriptions of the atom suggest that electron orbits are randomly and continuously distributed. However, in 1913 Niels Bohr combined the concepts of Max

Plank's quanta, Albert Einstein's photons and Ernest Rutherford's nuclear atom to suggest that electrons exist in orbits of well-defined size and shape (14-17). With both the classical and Bohr model, the angular momentum of the electrons will have an associated magnetic moment:

$$\boldsymbol{\mu} = \gamma \boldsymbol{I} \qquad [1.1]$$

where $\boldsymbol{\mu}$ is the magnetic moment, $\boldsymbol{I}$ is the angular momentum and γ is a scalar called the gyromagnetic ratio. In 1921, Otto Stern suggested the magnetic moment of atoms could be measured by observing their deflection when passed through an inhomogeneous magnetic field. If the classical model was correct, a beam of atoms should be deflected continuously over a single, symmetric region centered at the point of no deflection. If the Bohr model was correct, the atoms should be deflected into multiple distinct regions. A refined experiment in 1922 by Otto Stern and Walter Gerlach demonstrated that a beam of silver atoms passed through an inhomogeneous magnetic field is split into two distinct components (18).

This experiment verified the quantization of magnetic moment, but it was not completely consistent with Bohr's quantization of angular momentum. Consider the square of the orbital angular momentum operator:

$$\boldsymbol{L}^2 = L_x^2 + L_y^2 + L_z^2 . \qquad [1.2]$$

The components L_x, L_y and L_z of $\boldsymbol{L}$ are Hermitian operators that satisfy the commutation relations:

$$\left[L_x, L_y\right] = i\hbar L_z \quad \left[L_y, L_z\right] = i\hbar L_x \quad \left[L_z, L_x\right] = i\hbar L_y . \qquad [1.3]$$

Using Eqs. [1.2] and [1.3], it can be shown that $\boldsymbol{L}^2$ commutes with each component of $\boldsymbol{L}$ and therefore simultaneous eigenkets and eigenvalues can be specified for $\boldsymbol{L}^2$ and any one

component of $\boldsymbol{L}$. By convention we choose L_z and note that the eigenvalues of $\boldsymbol{L}^2$ will be $l(l+1)$ while the eigenvalues of L_z are $m=-l,-l+1,\ldots,l$ (19-21). The orbital angular momentum quantum number, l, is either a positive integer or zero. It was therefore expected that the Stern-Gerlach experiment, which measures a component of angular momentum, would yield an odd number $(2l+1)$ of components. This was inconsistent with the experimental results, which yielded two components for silver atoms. Similar results were obtained for atoms of copper, gold, sodium, potassium, cesium and even hydrogen.

Samuel Goudsmit and George Uhlenbeck gave an explanation of this result in 1925. They proposed that electrons must have a quantized, intrinsic magnetic moment in addition to the magnetic moment produced by orbital motion (22). The intrinsic magnetic moment is often labeled as *spin magnetic moment*. We must now consider the total angular momentum operator:

$$\boldsymbol{I} = \boldsymbol{L} + \boldsymbol{S} \qquad [1.4]$$

where $\boldsymbol{L}$ is the orbital angular momentum operator and $\boldsymbol{S}$ is the spin angular momentum operator (23). Similar to $\boldsymbol{L}^2$, $\boldsymbol{S}^2$ has eigenvalues $s(s+1)$ except that s, the spin quantum number or *spin*, can be both integer and half-odd-integer values (11, 19). Bosons are particles with integer spin ($s=0,1,2,\ldots$) while fermions are those with half-odd-integer spin ($s=1/2,3/2,\ldots$). Silver atoms are composed of a nucleus and 47 electrons, 46 of which form spherically symmetric orbits with no net angular momentum. The silver atom has a net angular momentum that is due solely to the spin ($s=½$) of the 47^{th} electron. The total number of expected components in the Stern-Gerlach experiment is then correctly predicted as $(2s+1)=2$.

1.1.2 Spin Behavior in a Static Magnetic Field

A nucleus that possesses primarily spin magnetic moment is often labeled generally as *a spin*. Hence *a spin* refers to the nucleus and *spin* refers to the spin quantum number. A spin placed in a static magnetic field, $\boldsymbol{H}$, has a Hamiltonian:

$$\mathcal{H} = -\boldsymbol{\mu} \cdot \boldsymbol{H} . \qquad [1.5]$$

By convention we take the static magnetic field to be H_0 along the z-direction. The Hamiltonian then reduces to:

$$\mathcal{H} = -\gamma\hbar H_0 I_z . \qquad [1.6]$$

Since we consider the spin to only posses spin angular momentum, the eigenvalues of I_z are m=-s,-s+1,…,s and the eigenstates are described in Dirac's *bra* and *ket* notation as $|s,m\rangle$. The eigenvalues of the Hamiltonian in Eq. [1.6] are simply multiples of the eigenvalues of the operator I_z:

$$E_m = -\gamma\hbar H_0 m . \qquad [1.7]$$

The time-dependent solution to the Schrödinger equation for a particular value of m is (19-21):

$$\psi_m(t) = |s,m\rangle e^{-\frac{i}{\hbar}E_m t} . \qquad [1.8]$$

A general solution is formed from a linear combination of the particular solutions in Eq. [1.8] as:

$$\psi(t) = \sum_{m=-s}^{s} c_m \psi_m(t). \qquad [1.9]$$

Immanuel Estermann and Otto Stern demonstrated in 1933 that a proton, like an electron, exhibits a spin of ½ (24). Although there are several biologically important nuclei used in human NMR, hydrogen nuclei are used most routinely due to their high abundance in

tissue (see Table 1.1). As a result, the remainder of this thesis will be based on ^{1}H MRI.

For ^{1}H there are two eigenstates which can be denoted $|\uparrow\rangle$ and $|\downarrow\rangle$. The eigenstate $|\uparrow\rangle$ is called *spin-up* and corresponds to spins which have a z-component of spin angular momentum parallel to the static magnetic field H_0. The eigenstate $|\downarrow\rangle$ is called *spin-down* and corresponds to spins that have a z-component of spin angular momentum anti-parallel to the static magnetic field. The spin-down state (m=-½) has a higher energy than the spin-up state (m=½) as given by Eq. [1.7] and shown in Fig. 1.1. The difference between the two energy levels is the Zeeman energy:

$$\Delta E = \hbar\omega_0 \qquad [1.10]$$

where $\omega_0=\gamma H_0$ is called the Larmor frequency.

To get a sense of how a spin behaves in a static magnetic field, we can determine the expectation value of the magnetic moment:

$$\langle \boldsymbol{\mu} \rangle = \langle \psi | \boldsymbol{\mu} | \psi \rangle . \qquad [1.11]$$

If we express the complex constants in Eq. [1.9] as

$$c_{\frac{1}{2}} = ae^{i\alpha} \qquad [1.12]$$

$$c_{-\frac{1}{2}} = be^{i\beta} \qquad [1.13]$$

Table 1.1: List of selected nuclei

Nucleus	Spin	γ	Abundance[a] in the Human Body
Hydrogen (^{1}H)	½	42.58 MHz/T	88M
Sodium (^{23}Na)	3/2	11.27 MHz/T	80mM
Phosphorus (^{31}P)	½	17.25 MHz/T	75mM
Oxygen (^{17}O)	5/2	-5.77 MHz/T	16mM
Fluorine (^{19}F)	½	40.08 MHz/T	4μM

[a]Relative body abundance (1M = 1 mole/liter). Hydrogen molarity of water is 110M.

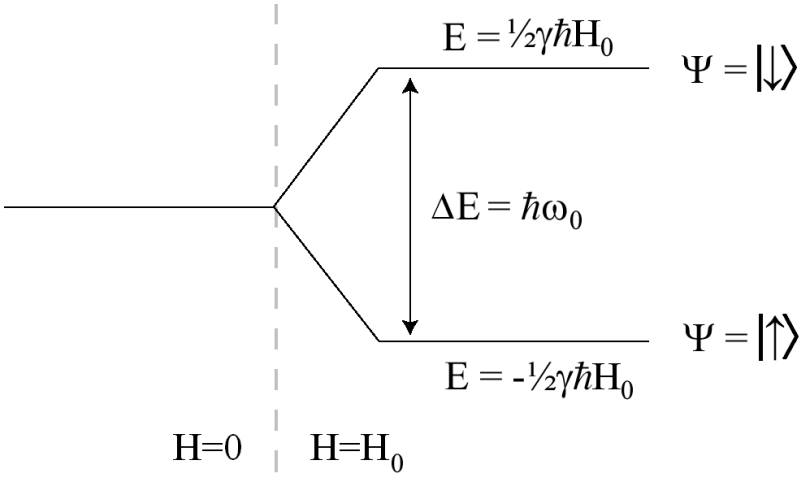

Figure 1.1: Energy eigenvalues for a spin ½ nucleus in a static magnetic field. When no magnetic field is present, the nucleus has one energy level, but when a magnetic field is introduced, the energy level splits into two levels separated by the Zeeman energy.

then Eq. [1.11] has solutions:

$$\langle \mu_x \rangle = \frac{\gamma\hbar}{2} \sin\theta \cos\phi \qquad [1.14]$$

$$\langle \mu_y \rangle = \frac{\gamma\hbar}{2} \sin\theta \sin\phi \qquad [1.15]$$

$$\langle \mu_z \rangle = \frac{\gamma\hbar}{2} \cos\theta \qquad [1.16]$$

provided

$$\phi = \beta - \alpha - \omega_0 t \qquad [1.17]$$

$$a^2 = \frac{1+\cos\theta}{2}. \qquad [1.18]$$

The result is that the expectation value of magnetic moment behaves like a vector precessing at the Larmor frequency in the negative ϕ direction. In fact, since most clinical applications of NMR are concerned with macroscopic quantities, it is often sufficient to take a classical approach in analyzing the behavior of magnetic moments. That is, we need only consider the macroscopic magnetization vector for each volume or

voxel of spins as:

$$\boldsymbol{M} = \sum_{voxel} \boldsymbol{\mu} \,. \qquad [1.19]$$

1.1.3 Thermal Equilibrium Magnetization

In equilibrium, a voxel will have $N_\uparrow$ spins aligned parallel to the static magnetic field and $N_\downarrow$ spins aligned anti-parallel to produce a net magnetization:

$$M_0 = \frac{\gamma\hbar\left(N_\uparrow - N_\downarrow\right)}{2V}\hat{z} \qquad [1.20]$$

where V is the voxel volume. The distribution of spins between the two energy levels is governed by Boltzmann statistics (25, 26):

$$\frac{N_\uparrow}{N_\downarrow} = e^{\frac{\Delta E}{kT}} \qquad [1.21]$$

where k is the Boltzmann constant and T is the absolute temperature of the voxel. At a normal human body temperature and a magnetic field strength of 3 Tesla, the ratio of $\Delta E/kT$ for ^{1}H is about 0.00002. The population difference can then be calculated as:

$$N_\uparrow - N_\downarrow = N \cdot \tanh\left(\frac{\Delta E}{2kT}\right) \approx N\frac{\Delta E}{2kT} \qquad [1.22]$$

where $N = N_\uparrow + N_\downarrow$ is the total number of spins in the voxel and *tanh( )* is the hyperbolic tangent function, which is approximately linear for $\Delta E << kT$. Using Eqs. [1.10], [1.20] and [1.22], the net magnetization can be approximated as:

$$M_0 \approx \frac{N\gamma^2\hbar^2 H_0}{4kTV}\hat{z}\,. \qquad [1.23]$$

The magnetization is proportional to the number of spins and inversely proportional to the temperature. The more applicable result is that if the strength of the static field

doubles, such as the trend of clinical MRI scanners moving from 1.5 Tesla to 3 Tesla, the equilibrium magnetization is expected to double. This will have important consequences when we consider measures of image quality such as signal-to-noise ratios or image resolution.

1.1.4 Signal Detection

A magnetic moment will experience a torque when exposed to an external magnetic field. The torque placed on the magnetic moment defines the time rate of change of angular momentum:

$$\frac{d\boldsymbol{I}}{dt} = \boldsymbol{\mu} \times \boldsymbol{H} \,. \qquad [1.24]$$

Using Eq. [1.1], [1.19] and [1.24] we get the effect of an external magnetic field on our magnetization:

$$\frac{d\mathbf{M}}{dt} = \gamma \mathbf{M} \times \mathbf{H} \,. \qquad [1.25]$$

In a static magnetic field, H_0 along the z-axis, the differential Eq. [1.25] has solutions:

$$M_z(t) = M_z(0) \qquad [1.26]$$

$$M_{xy}(t) = M_{xy}(0) e^{-i\omega_0 t} \qquad [1.27]$$

where M_z, the *longitudinal magnetization*, is the component of magnetization along the z-axis and M_{xy}, the *transverse magnetization*, is defined as:

$$M_{xy}(t) = M_x(t) + iM_y(t) \,. \qquad [1.28]$$

In Eq. [1.26], the longitudinal component of magnetization remains unchanged while the transverse component in Eq. [1.27] precesses at the Larmor frequency.

Faraday's law of induction describes the electromotive force (EMF) that is induced in

a coil due to a magnetic flux experienced by the coil (27, 28):

$$\varepsilon = -\frac{d\phi_M}{dt} \qquad [1.29]$$

where ε is the EMF and ϕ_M is the magnetization flux through the coil defined as:

$$\phi_M = \int_{coil} \boldsymbol{M} \cdot \boldsymbol{dA} \qquad [1.30]$$

The longitudinal component of magnetization in Eq. [1.26] does not change in time and therefore does not induce an EMF. However, the transverse component of magnetization can induce an EMF in a suitably oriented coil. A signal induced in the coil due to magnetic resonance is often denoted as a *free induction decay* or FID.

1.1.5 Spin Excitation

In the previous section it was stated that the transverse component of magnetization could be detected with a nearby coil. However, no mention was made as to how a transverse component of magnetization arises when only a longitudinal component exists in thermal equilibrium (as given by Eq. [1.23]). Consider a time dependent magnetic field:

$$H_1(t)\cdot\left[\cos(\omega_1 t+\phi)\hat{x}-\sin(\omega_1 t+\phi)\hat{y}\right] \qquad [1.31]$$

applied perpendicular to the static magnetic field. $H_1(t)$ is called the envelope function because it modulates the sinusoidal wave. The net magnetic field experienced by a voxel of spins is now:

$$H(t)=H_1(t)\cdot\left[\cos(\omega_1 t+\phi)\hat{x}-\sin(\omega_1 t+\phi)\hat{y}\right]+H_0\hat{z}\,. \qquad [1.32]$$

the differential Eq. [1.25] now becomes:

$$\frac{dM_x}{dt}=\gamma\left[M_y H_0+M_z H_1(t)\sin(\omega_1 t+\phi)\right] \qquad [1.33]$$

$$\frac{dM_y}{dt} = \gamma\left[M_z H_1(t)\cos(\omega_1 t + \phi) - M_x H_0\right] \quad [1.34]$$

$$\frac{dM_z}{dt} = -\gamma H_1(t)\left[M_x \sin(\omega_1 t + \phi) + M_y \cos(\omega_1 t + \phi)\right]. \quad [1.35]$$

Although a closed form solution is not available for an arbitrary envelope function, $H_1(t)$, we can visualize what is happening with the concept of a rotating reference frame (29).

In the rotating reference frame, the z-axis remains unchanged but the coordinates perpendicular to the z-axis rotate at the Larmor frequency (Fig. 1.2a). The new coordinate system is:

$$\hat{x}' = \cos(\omega_0 t)\hat{x} - \sin(\omega_0 t)\hat{y} \quad [1.36]$$

$$\hat{y}' = \sin(\omega_0 t)\hat{x} + \cos(\omega_0 t)\hat{y} \quad [1.37]$$

$$\hat{z}' = \hat{z}\,. \quad [1.38]$$

The effective magnetization in the rotating reference frame is:

$$H_{eff}(t) = H_1(t)\cdot\left[\cos(\phi)\hat{x}' - \sin(\phi)\hat{y}'\right] + \left(H_0 - \frac{\omega_1}{\gamma}\right)\hat{z}'\,. \quad [1.39]$$

According to Eq. [1.25], the component of magnetization that is parallel to the effective magnetic field will remain unchanged while the component that is perpendicular to $H_{eff}(t)$ will precess about the effective field at the angular frequency:

$$\omega_{eff}(t) = \gamma\left|H_{eff}(t)\right|. \quad [1.40]$$

The trajectory of the magnetization in the rotating reference frame is along the surface of a cone (see the example in Fig. 1.2b). In order to excite the magnetization vector, a time varying magnetic field is applied for a finite time to allow the magnetization to rotate partially around the cone. When the time varying field is switched off, the magnetization vector may now have a component transverse to the static magnetic field.

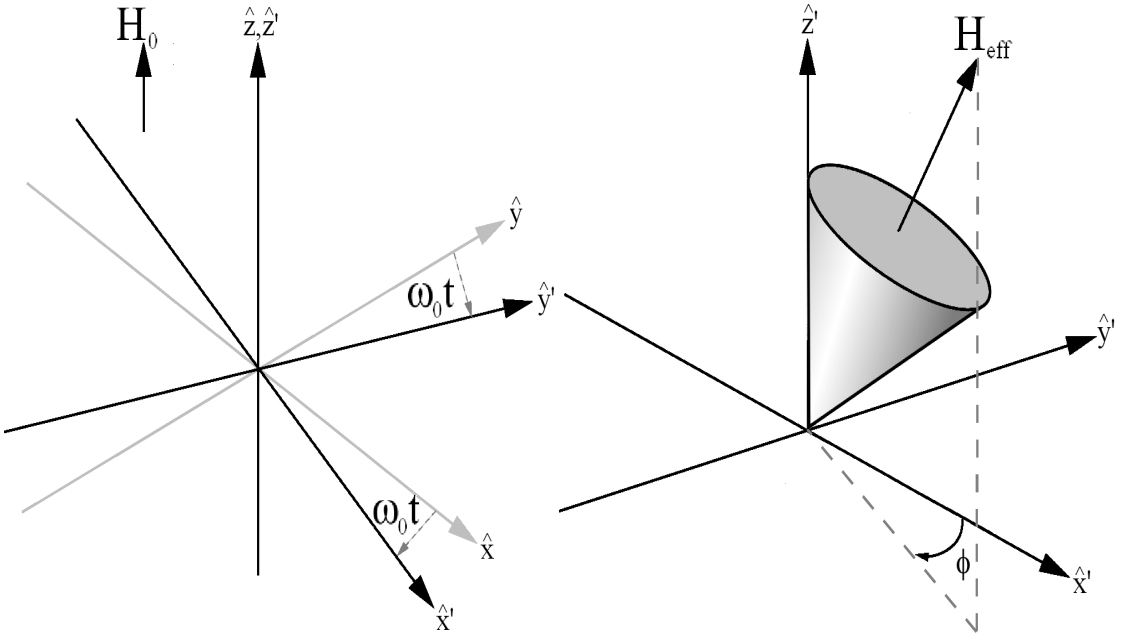

(a) (b)

Figure 1.2: Spin excitation in the rotating reference frame. The relation between the rotating and the laboratory reference frame is shown in (a). The cone of precession in the rotating field (b) is shown for an off resonance time varying magnetic field.

A few important points should be made about this cone of precession. First, as the frequency of the time varying magnetic field approaches zero, the cone collapses to the z'-axis. The physical meaning is that no excitation is possible when ω_1=0. When the frequency of the time varying field matches the Larmor frequency of the static field, then the cone spreads into a plane (Fig. 1.3). This is the only time when it is possible to excite the magnetization vector to lie along the negative z'-axis (also known as inversion). In most cases the time varying field is applied on resonance ($\omega_0=\omega_1$). Since human clinical MRI is typically performed with a static field strength of a few Tesla, an on resonance pulse will have a frequency in the radio frequency (RF) range. As a result, the time varying magnetic field is often referred to as a RF pulse. Both the magnitude and the duration of the RF pulse determine how much the magnetization vector precesses or flips

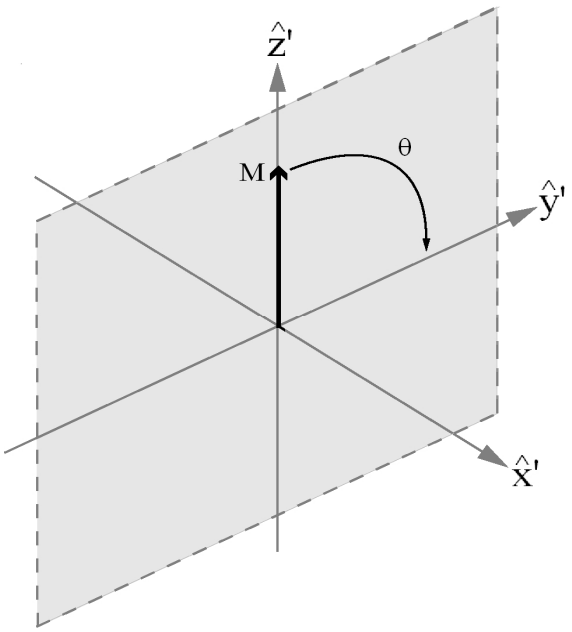

Figure 1.3: The cone of precession for an on resonance RF pulse. The cone flattens into a plane when the RF pulse is applied on resonance. In this case, the RF pulse is applied along the x'-axis (ϕ=0). The magnetization will rotate an angle θ (flip angle) in the y'z'-plane.

in the rotating reference frame. The flip angle is defined as:

$$\theta = \int_{pulse} \gamma H_1(t) dt \,. \qquad [1.41]$$

A flip angle of 90° would rotate a magnetization vector from along the z'-axis into the transverse plane (excitation). A flip angle of 180° would invert a magnetization vector from along the z'-axis to the negative z'-axis (inversion). Both of these RF pulses play a critical role in TSE sequences. For pulses of arbitrary flip angles, it is useful to have a set of equations to determine what the magnetization vector will be after experiencing a RF pulse with a given phase and flip angle (30):

$$M_{x'}^{+} = M_{x'}^{-}\left[\cos(\theta)\sin^2(\phi)+\cos^2(\phi)\right]+M_{y'}^{-}\left[\sin^2\left(\tfrac{1}{2}\theta\right)\sin(2\phi)\right]-M_{z'}^{-}\left[\sin(\theta)\sin(\phi)\right]. \qquad [1.42]$$

$$M_{y'}^{+} = M_{x'}^{-}\left[\sin^2\left(\tfrac{1}{2}\theta\right)\sin(2\phi)\right]+M_{y'}^{-}\left[\cos(\theta)\cos^2(\phi)+\sin^2(\phi)\right]+M_{z'}^{-}\left[\sin(\theta)\cos(\phi)\right] \qquad [1.43]$$

$$M_{z'}^{+} = M_{x'}^{-}[\sin(\theta)\sin(\phi)] - M_{y'}^{-}[\sin(\theta)\cos(\phi)] + M_{z'}^{-}[\cos(\theta)]. \quad [1.44]$$

The "+" superscripts indicate the values just after the RF pulse and the "-" superscripts indicate the values just prior to the RF pulse.

In addition to modifying the magnetization vector, a RF pulse also deposits energy into any conducting tissue. To a first order approximation the total RF energy deposited into a sphere of conducting media is (31):

$$P = \frac{\sigma\pi\omega_1^2 H_1^2 R^5}{15} \quad [1.45]$$

where σ is the conductivity of the tissue and R is the radius of the sphere. The specific absorption rate (SAR) is defined as the energy per unit volume per unit time that is delivered to a sample. Using the same spherical sample from Eq. [1.45] the average SAR is defined as (32):

$$SAR = \frac{\sigma D\omega_1^2 H_1^2 R^2}{20\rho} \quad [1.46]$$

where ρ is the density of the sample and D is the RF duty cycle. The SAR is a critical factor in determining the amount of sample heating that will occur as a result of a RF excitation. Governing agencies such as the FDA Center for Devices and Radiological Health place restrictions on the SAR. At the time this thesis was written, the current FDA guidelines prevent a specific absorption rate greater than:

a) 4 W/kg averaged over the whole body for any period of 15 minutes; or

b) 3 W/kg averaged over the head for any period of 10 minutes; or

c) 8 W/kg in any gram of tissue in the head or torso, or 12 W/kg in any gram of tissue in the extremities, for any period of 5 minutes;

A couple of important points should be made in regard to SAR limitations. First, since

the flip angle is linear with the RF amplitude, the SAR varies as the square of the flip angle. A 180° RF pulse has a SAR four times that of a 90° RF pulse. The second thing to note is that the SAR varies as the square of the Larmor frequency and consequently as the square of the static magnetic field. A RF pulse at 3 Tesla deposits four times more energy than the equivalent RF pulse at 1.5 Tesla.

1.1.6 Relaxation

Relaxation is a process that describes how a displaced magnetization vector returns to thermal equilibrium. In particular, longitudinal relaxation is how the longitudinal component of the magnetization vector returns to its thermal equilibrium value M_0. The mechanism behind longitudinal relaxation is an energy exchange between resonant nuclei and the surrounding molecular lattice (33, 34). Bloch and Purcell demonstrated that the longitudinal relaxation rate is related to the degree that M_z has been displaced from thermal equilibrium:

$$\frac{dM_z}{dt} = \frac{M_0 - M_z(t)}{T_1} \qquad [1.47]$$

where T_1 is the spin-lattice relaxation time and is dependent on both the sample type and the static magnetic field strength (35). In addition to the longitudinal component returning to M_0, thermal equilibrium also requires there to be no transverse magnetization. The decay of transverse magnetization to zero is known as transverse relaxation and involves both reversible and non-reversible processes (11). The relaxation of transverse magnetization is governed by the following differential equation:

$$\frac{dM_{xy}}{dt} = \frac{-M_{xy}(t)}{T_2^*} \qquad [1.48]$$

where

$$M_{xy} = M_x + iM_y \qquad [1.49]$$

and T_2^* is the transverse relaxation time including both reversible and non-reversible contributions. The transverse relaxation time can be separated into these two different contributions as:

$$\frac{1}{T_2^*} = \frac{1}{T_2} + \frac{1}{T_2'} \qquad [1.50]$$

where T_2 characterizes the non-reversible contributions arising from mechanisms such as spin-spin interactions and T_2' characterizes reversible contributions arising from magnetic field inhomogeneities and susceptibility effects. The longitudinal and transverse relaxation times for various tissues at common field strengths are given in Table 1.2. Combining Eq. [1.25], [1.47] and [1.48] we get the general form of the well known Bloch differential equation:

$$\frac{d\mathbf{M}}{dt} = \gamma \mathbf{M} \times \mathbf{H} - \frac{M_x \hat{x} + M_y \hat{y}}{T_2^*} + \frac{M_0 - M_z}{T_1} \hat{z} \qquad [1.51]$$

which, in a static magnetic field H_0, has solutions:

$$M_z(t) = M_0 + [M_z(0) - M_0] e^{\frac{-t}{T_1}}. \qquad [1.52]$$

$$M_{xy}(t) = M_{xy}(0) e^{-\left(i\omega_0 + \frac{1}{T_2^*}\right)t}. \qquad [1.53]$$

Figure 1.4 illustrates the return to thermal equilibrium for fat and muscle samples, at 3 Tesla, after the magnetization has been excited into the transverse plane.

Table 1.2: Approximate relaxation times of selected tissues

	T_1 (ms)		T_2 (ms)	
Tissue	1.5 Tesla	3.0 Tesla	1.5 Tesla	3.0 Tesla
Gray Matter[b]	1000	1450	100	110
White Matter[b]	550	800	80	80
CSF[b]	4250	4150	2200	2200
Liver[a]	600	800	50	40
Spleen[a]	1050	1400	80	60
Pancreas[a]	600	750	50	50
Muscle[a]	850	900	30	40
Fat[a]	350	400	60	70
Prostate[a]	1350	1600	90	80

[a]Source (36) [b]Source (37, 38).

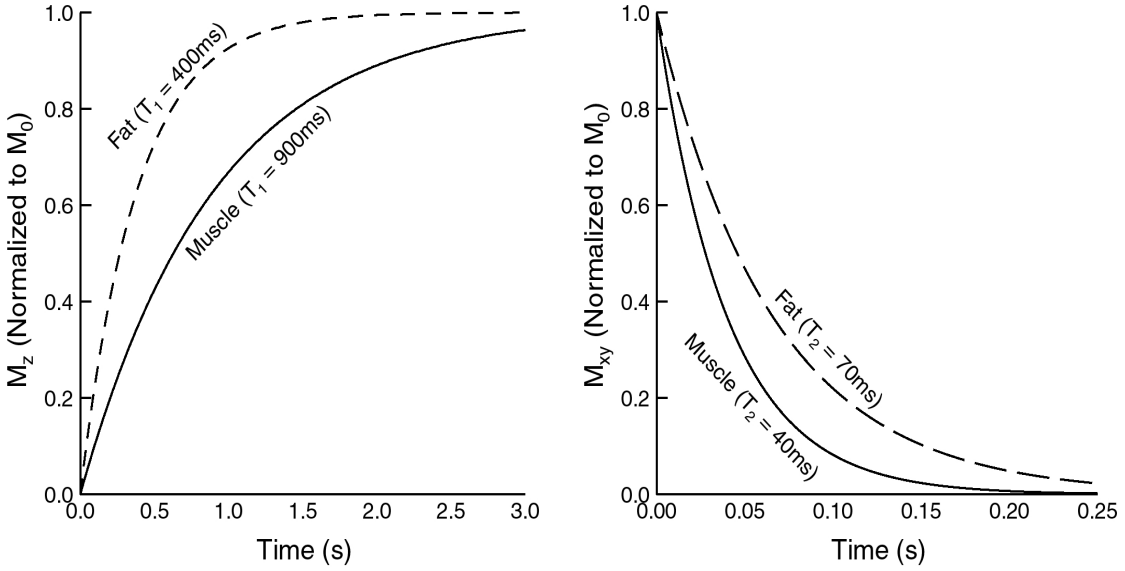

Figure 1.4: A magnetization vector excited into the transverse plane will return to thermal equilibrium through (a) longitudinal relaxation and (b) transverse relaxation. The transverse relaxation time in (b) is the nonreversible component T_2.

1.2 Magnetic Resonance Imaging

Nearly 30 years after the NMR publications by Bloch and Purcell, Paul Lauterbur localized the source of the NMR signal using spatially varying magnetic field gradients (39). Shortly thereafter, Peter Mansfield related the spin density with the Fourier Transform of the detected signal (40). For this early work in signal localization, Lauterbur and Mansfield shared the 2003 Nobel Prize in Physiology or Medicine. In 1975, Anil Kumar, Dieter Welti and Richard Ernst extended these localization ideas with a 2D Fourier Imaging method which is still commonly used in NMR image reconstruction (41). Because the term *nuclear* often creates public relation concerns, the imaging community refers to nuclear magnetic resonance imaging simply as magnetic resonance imaging or MRI. The following sections outline some basic principles of MRI with more detail found in sources (30, 37, 42, 43).

1.2.1 Radio Frequency Coils

An ideal RF coil should be able to transmit a transverse, circularly polarized magnetic field that is uniform in both amplitude and phase across the functional volume of the coil (44-46). Transmission and reception in NMR experiments are typically accomplished with either surface or volume coils or a combination of the two (47-50). The sensitivity of a surface coil falls off quickly along the axial direction and the coil is only sensitive for a fraction of the loop diameter (51). If the region of interest lies near the surface of the sample then a surface coil will provide advantages over a volume coil (52). For deep lying structures or when large regions of interest are needed, a volume coil is a more appropriate selection (53-57). The birdcage coil remains one of the most popular volume coil designs (58). In this work, the excitation of spins is accomplished with a large

volume coil that surrounds the entire patient. The detection of signal is accomplished with one of three coils shown in Fig. 1.5.

1.2.2 Gradient Magnetic Fields

A *gradient* in MRI is a spatially dependent magnetic field. An ideal gradient will vary linearly with position across a volume of interest. The magnitude of the gradient field is typically much less than the main static magnetic field. For example, on the Siemens 3.0 Tesla Trio scanner used to acquire data for this thesis, the gradients have a maximum strength of 40 mT/m. Most imaging occurs within half a meter from isocenter making the gradients less than 1% of the total magnetic field. As a result, any component of a gradient field that is perpendicular to the static magnetic field will have little effect on the magnetization. The net magnetic field can then be approximated as:

$$H(t) = \left[\mathbf{G}(t) \cdot \mathbf{r}(t) + H_0\right]\hat{z} \qquad [1.54]$$

where $\boldsymbol{G}(t)=[G_x(t),G_y(t),G_z(t)]$ is the strength of the gradient fields (typically measured in mT/m for clinical MRI) and $\boldsymbol{r}(t)=[x(t),y(t),z(t)]$ is the position of the spin measured from

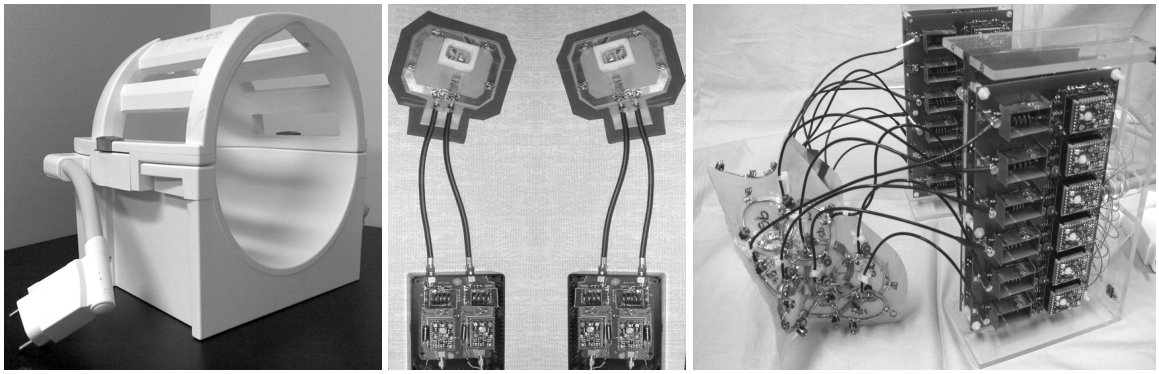

(a) (b) (c)

Figure 1.5: Receive coils used to collect data presented in this thesis. A 12-channel commercial birdcage coil (Siemens Medical) is shown in (a) and is typically used for head imaging and phantom tests. The 4-element surface array (b) and 16-element carotid coil (c) provide advantages over volume coils for neck imaging applications (59, 60).

the MRI scanner isocenter. In contrast to labeling gradients by their physical axis (G_x, G_y and G_z), gradients are often labeled with respect to the orientation of the current slice as G_s (slice direction), G_r (readout direction) and G_p (phase encode direction). This simplifies gradient design when considering slices at different orientations.

A gradient may be turned off and on and applied at varying strengths during a MRI experiment. The behavior of a gradient during an experiment is expressed in a gradient diagram. Figure 1.6 shows a simple gradient diagram and the corresponding magnetic field expected. The equations of motion describing a magnetization vector in a static magnetic field (Eq. [1.52]) are still valid when gradients are applied; however, the precession frequency of the transverse magnetization is now spatially dependent. As a result, a spin off-isocenter will acquire a phase difference from a spin on-isocenter after a gradient pulse has been applied

$$\phi = \gamma \int \mathbf{G}(t) \cdot \mathbf{r}(t) dt \,. \qquad [1.55]$$

The equation of motion can be generalized as a series:

$$\mathbf{r}(t) = \sum_n \frac{1}{n!} \mathbf{r}_n t^n \qquad [1.56]$$

where the nth term in the series is called the nth moment of motion and r_0 is the initial position, r_1 is the velocity, r_2 is the acceleration etc.... The phase acquired due to the nth moment of motion is called the nth gradient moment:

$$\phi^n = \frac{\gamma}{n!} \int \mathbf{G}(t) \cdot \mathbf{r}_n t^n dt \,. \qquad [1.57]$$

The concept of gradient moment nulling, setting Eq. [1.57] to zero for specific values of n, is particularly important in many MRI applications (61).

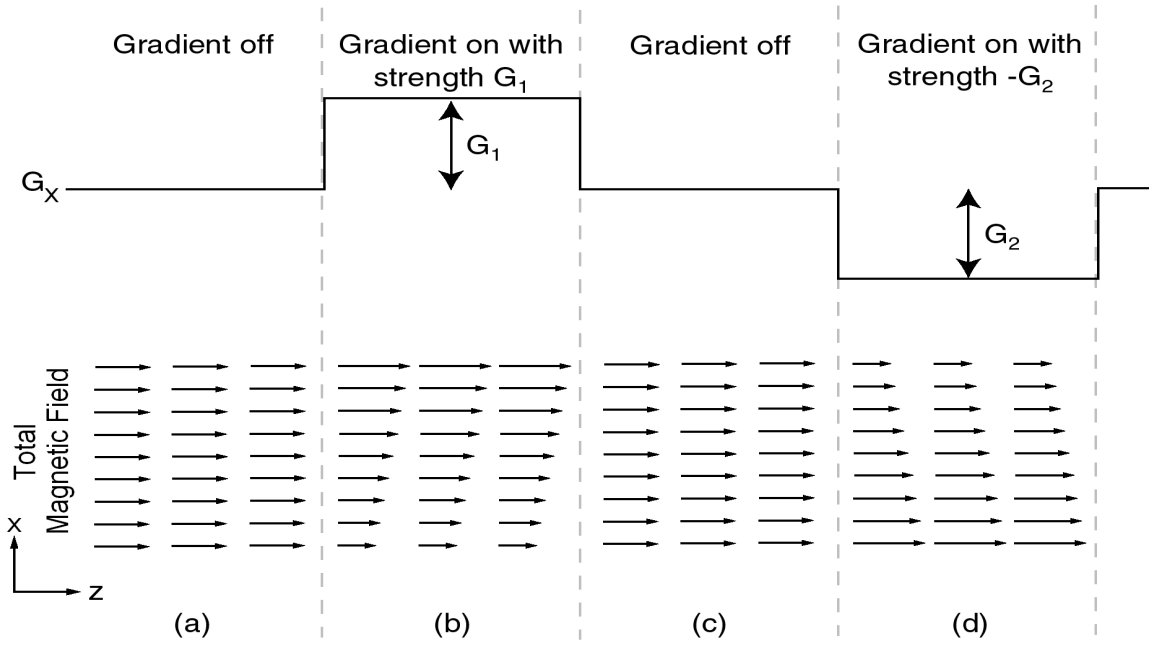

Figure 1.6: A gradient diagram containing two gradient pulses. During (a) and (c) there are no applied gradients and the magnetic field is the uniform H_0 field. During (b) and (d), a gradient pulse is applied and the resulting magnetic field is a superposition of H_0 and the gradient field. The strength of the gradient fields has been exaggerated for illustration purposes.

1.2.3 Slice Selection

The details of how a MR image may be obtained from a particular cut or slice through an object are contained in the process of slice selection. Slice selection involves the simultaneous application of a gradient magnetic field in the slice direction and a RF pulse to selectively excite a slice of spins. Any finite duration RF pulse applied in a MRI experiment will have a distribution of spectral frequencies and a corresponding bandwidth (BW). The application of the slice gradient during the RF pulse will cause a linear distribution of Larmor frequencies across the slice. Spins with a Larmor frequency within the distribution of frequencies (frequency band) of the RF pulse will be excited. Spins that are outside the frequency band (outside the desired slice) are not appreciably excited because they have Larmor frequencies too different from the RF pulse spectrum.

A RF pulse whose spectrum contains a range of frequencies will therefore excite a range of spins (Fig. 1.7). The ideal excitation profile of the slice is uniform inside the slice boundaries and null everywhere else. In practice, however, the profile is a complex function of pulse design (62, 63). A good estimate of the profile can be made by observing the spectrum of the RF pulse envelope. Typically some sort of filtered sinc() function is used as the RF envelope. Figure 1.8 shows a filtered sinc() pulse and the corresponding spectrum.

During the application of the RF pulse and slice gradient, spins at different spatial locations precess at different angular frequencies. Accordingly, the phase of each spin at the end of the RF pulse will be spatially dependent. Since the FID signal is a superposition of all the spins, any phase dispersion will lead to destructive interference.

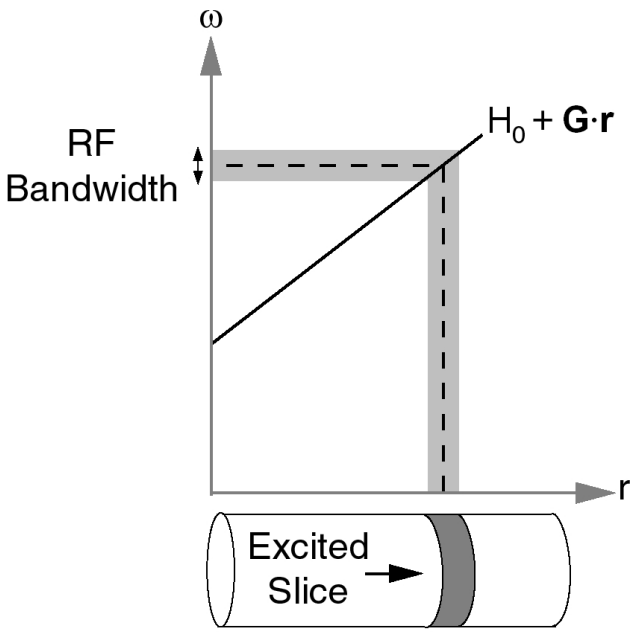

Figure 1.7: Basic principle of gradient slice selection. With an applied gradient field there is a linear distribution of Larmor frequencies across the sample. Spins with a Larmor frequency within the distribution of frequencies (frequency band) of the RF pulse will be excited.

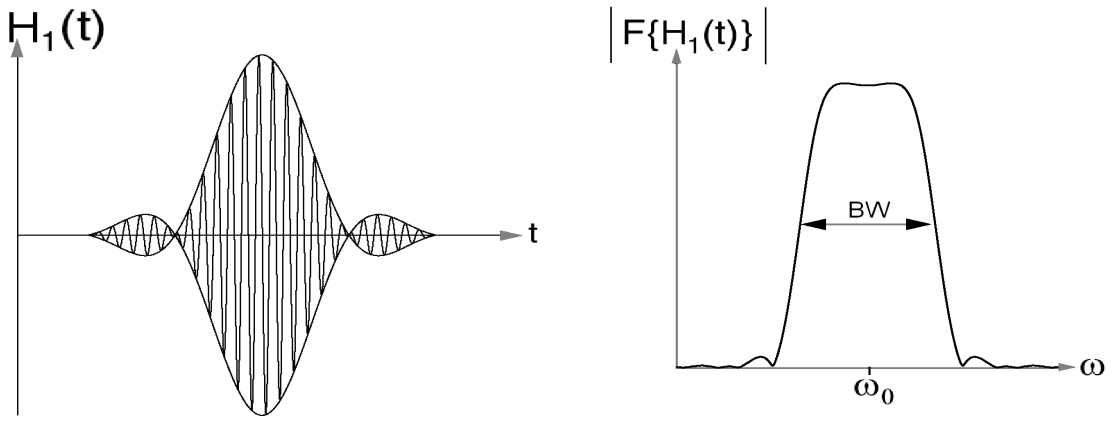

(a) (b)

Figure 1.8: Excitation pulse profile. A filtered three lobe sinc RF pulse (a) has the corresponding spectrum shown in (b). The excitation profile approximately correlates with the RF spectrum.

In general the phase distribution is intricate and must be found through solutions of the Bloch equations. Fortunately, for small rotations (even up to 90 degrees), the phase distribution is approximately linear and will be nearly eliminated with the application of a second gradient (Fig. 1.9).

1.2.4 Spatial Encoding

After slice excitation and spin rephasing, such as shown in Fig. 1.9, all the spins in the slice are assumed to be approximately in phase. Spatial encoding occurs when we apply gradients in directions perpendicular to the slice direction. These gradients effectively encode spatial information into the FID. The spatial information can be extracted using a mathematical tool called a Fourier transform (64). The Fourier transform of a signal m(x) is defined as:

$$\Im[m(x)] = M(k_x) = \int_{-\infty}^{\infty} m(x) e^{-2\pi i k_x x} dx \qquad [1.58]$$

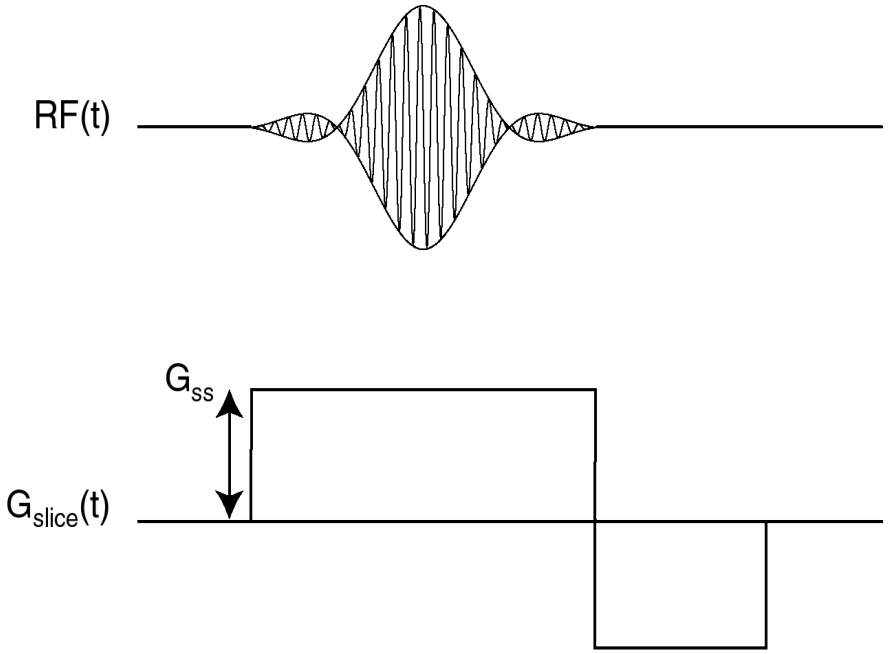

Figure 1.9: Typical slice selection RF and gradient waveforms.

with an inverse Fourier transform:

$$\Im^{-1}\left[M\left(k_x\right)\right] = m\left(x\right) = \tfrac{1}{2\pi}\int_{-\infty}^{\infty} M\left(k_x\right)e^{2\pi i k_x x}dk_x \,. \qquad [1.59]$$

An object can be thought of as a distribution of magnetization vectors. After excitation, each magnetization vector has some transverse component described as ***m****(x,y,z)*. Initially we assume that the static magnetic field is uniform, that we use a receive coil that is uniform over the entire object and that relaxation effects are negligible. Under such circumstances, the induced EMF is proportional to the integration of magnetization vectors over the entire excited volume:

$$\varepsilon\left(t\right) \propto \int_x\int_y\int_z \mathbf{m}\left(x,y,z\right)e^{-i\omega_0 t}dxdydz \,. \qquad [1.60]$$

A typical practice is to demodulate our received signal to remove the effect of the static ω_0 (65). If we allow time dependent gradients to be applied to the object, each

magnetization vector acquires a time dependent phase according to Eq. [1.55]:

$$\mathbf{m}(x,y,z) \rightarrow \mathbf{m}(x,y,z)e^{-i\gamma\int_0^t [G_x(\tau)x+G_y(\tau)y+G_z(\tau)z]d\tau}. \quad [1.61]$$

If the following definitions are used:

$$k_x(t) = \frac{\gamma}{2\pi}\int_0^t G_x(\tau)d\tau \quad [1.62]$$

$$k_y(t) = \frac{\gamma}{2\pi}\int_0^t G_y(\tau)d\tau \quad [1.63]$$

$$k_z(t) = \frac{\gamma}{2\pi}\int_0^t G_z(\tau)d\tau \quad [1.64]$$

the demodulated measured signal becomes:

$$\varepsilon(t) \propto \int_x\int_y\int_z \mathbf{m}(x,y,z)e^{-2\pi i(k_x x+k_y y+k_z z)}dxdydz. \quad [1.65]$$

Comparing with Eq. [1.58], we see that:

$$\varepsilon(t) \propto \mathbf{M}(k_x,k_y,k_z). \quad [1.66]$$

At any given time, the signal $\varepsilon(t)$ is proportional to a particular value of the Fourier transform of $\boldsymbol{m}(x,y,z)$. The location of this point in the Fourier transform space (called k-space) is controlled by the application of localization gradients given by Eqs. [1.62]-[1.64]. Consequently, with the appropriate selection of localizing gradients between samples of $\varepsilon(t)$, a trajectory of data points through k-space can be filled. When a sufficient amount of k-space data has been collected the inverse Fourier transform is applied to the k-space data to recover the distribution of magnetization vectors and the corresponding image of the object. Figure 1.10 demonstrates the trajectories through k-space for a basic 2D Cartesian imaging sequence. Each time the segment is applied, a

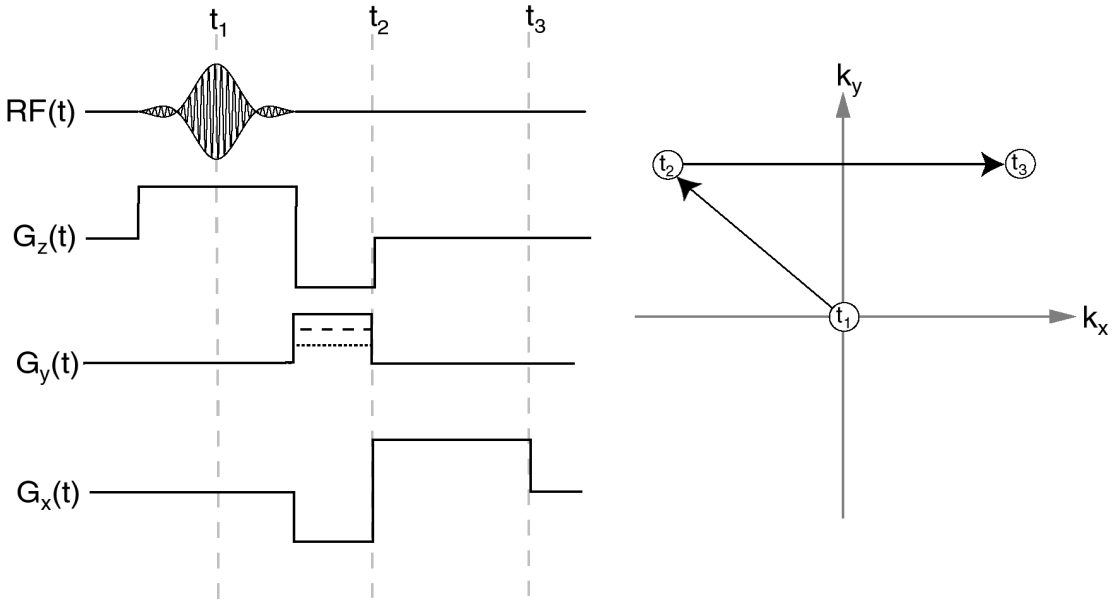

Figure 1.10: Example of a basic 2D Cartesian imaging sequence. At time t_1, the magnetization vectors are excited from the z-axis into the transverse plane. Between t_1 and t_2, the negative slice gradient corrects the phase distribution the magnetization vectors acquired during excitation. The phase gradient (applied in the y-direction) has a variable strength that is used to set the k_y position in k-space. During this same interval, the negative read gradient (x-direction) positions k_x. The data is sampled between t_2 and t_3. During data acquisition, the read gradient is turned on such that k_x moves across a line in k-space while data is being sampled. At the end of t_3, one line of data has been acquired in k-space.

single line of k-space data is acquired. To acquire other data lines, the entire segment is repeated with a different phase encode value (dashed and dotted lines in Fig. 1.10).

1.2.5 Data Sampling

The trajectory through k-space, determined by Eqs. [1.62]-[1.64], is a continuous function but data sampling is generally performed with a discrete system. The effect of sampling discretely in the Fourier domain (k-space) amounts to replication in the image domain. The distance between samples in k-space determines the FOV in image space as:

$$\Delta k_x = \frac{1}{FOV_x}, \quad \Delta k_y = \frac{1}{FOV_y}, \quad \Delta k_z = \frac{1}{FOV_z}. \qquad [1.67]$$

If samples are sampled too far apart, then the FOV shrinks and aliased copies of the object appear in the image. A mathematical theory governing sample spacing to achieve a desired FOV is known as Nyquist Sampling (65). In addition to sample spacing, the number of k-space samples will effectively determine the final resolution of the reconstructed image. Both of these are important considerations in sequence design.

Although the majority of clinical MRI sequences utilize Cartesian sampling patterns, a number of other k-space trajectories such as radial or spiral are available. However, since the purpose of this dissertation is to propose techniques that easily integrate to existing infrastructure, only a Cartesian based sequence will be considered.

1.2.6 Noise

Noise in MR images consists of thermal noise from the sample, quantization noise in A/D devices, preamp/electronic noise and thermal noise in the RF coil. Of all these, when the electronics are properly designed, thermal noise in the sample is the dominant source of noise in a MR experiment. One major consideration is that any part of the sample visible to the receive coil contributes noise rather than just the imaged slice. A common metric of noise in MRI is the use of the signal-to-noise ratio (SNR). The SNR is a complicated function of many values but a useful form is given as (43, 66, 67):

$$SNR \propto \Delta x \Delta y \Delta z \sqrt{t_{acq}} f\left(\rho, T_1, T_{2,\ldots}\right) \qquad [1.68]$$

where $\Delta x \Delta y \Delta z$ is the volume of the imaging voxel, t_{acq} is the total time data is sampled (not necessarily the total sequence time) and $f(\rho, T_1, T_2, \ldots)$ is a function which depends on many parameters including spin density and relaxation times. Equation [1.68] demonstrates that increasing the resolution of our images or reducing scan time, both desirable characteristics, has the unfortunate effect of decreasing the SNR.

1.3 References

1. Fisher M, Paganini-Hill A, Martin A, Cosgrove M, Toole JF, Barnett HJ, Norris J. Carotid plaque pathology: thrombosis, ulceration and stroke pathogenesis. Stroke 2005;36:253-257.

2. Fox AJ. How to measure carotid stenosis. Radiology 1993;186:316-318.

3. North American Symptomatic Carotid Endarterectomy Trial Collaborators. Beneficial effect of carotid endarterectomy in symptomatic patients with high-grade carotid stenosis. N. Engl. J. Med. 1991;325:445-453.

4. European Carotid Surgery Trialists' Collaborative Group. MRC European carotid surgery trial: interim results for symptomatic patients with severe (70-99%) or with mild (0-29%) carotid stenosis. Lancet 1991;337:1235-1243.

5. Executive Committee for the Asymptomatic Carotid Atherosclerosis Study. Endarterectomy for asymptomatic carotid artery stenosis. JAMA 1995;273:1421-1428.

6. Lurie DJ. Commentary: electron spin resonance imaging studies of biological systems. BRIT J RADIOL 1996;69:983-984.

7. Rabi II, Millman S, Kusch P, Zacharias JR. The molecular beam resonance method for measuring nuclear magnetic moments.. Phys Rev 1939;55:526-535.

8. Purcell EM, Torrey HC, Pound RV. Resonance absorption by nuclear magnetic moments in a solid. Phys Rev 1946;69:37-38.

9. Bloch F, Hansen WW, Packard M. Nuclear induction. Phys Rev 1946;69:127.

10. Abragam A. The Principles of Nuclear Magnetism: The international series of monographs on physics. Oxford: Clarendon Press; 1961. 599p.

11. Slichter CP. Principles of magnetic resonance - third edition. New York: Springer-Verlag; 1989. 655p.

12. Ernst RR, Bodenhausen G, Wokaun A. Principles of nuclear magnetic resonance in one and two dimensions. Oxford: Oxford University Press; 1987. 610p.

13. Fukushima E, Roeder SBW. Experimental pulse NMR: a nuts and bolts approach. Reading: Addison Wesley; 1982. 539p.

14. Bohr N. On the constitution of atoms and molecules. Philos 1913;26:1-25.

15. Rutherford E. The scattering of α and β particles by matter and the structure of the atom. Philos 1911;21:669-688.

16. Einstein A. Über einen die erzeugung und verwandlung des lichtes betreffenden heuristischen gesichtspunkt. Ann Phys 1905;17:132-148.

17. Planck M. Ueber das gesetz der energieverteilung im normalspectrum. Ann Phys 1901;4:553-563.

18. Gerlach W, Stern O. Der experimentelle nachweis der richtungsquantelung im magnetfeld. Z Phys A 1922;9:349-352.

19. Sakurai JJ. Modern quantum mechanics. New York: Addison Wesley; 1994. 508p.

20. Bransden BH, Joachain CJ. Introduction to quantum mechanics. Essex: Longman; 1989. 707p.

21. Griffiths DJ. Introduction to quantum mechanics - first edition. Upper Saddle River: Prentice Hall; 1995. 394p.

22. Uhlenbeck GE, Goudsmit SA. Ersetzung der hypothese vom unmechanischen zwang durch eine forderung bezüglich des inneren verhaltens jedes einzelnen elektrons. Naturwiss 1925;13:953-954.

23. Bransden BH, Joachain CJ. Introduction to quantum mechanics. Essex: Longman; 1989. 246-306p.

24. Estermann I, Stern O. Magnetic moment of the proton. Phys Rev 1933;52:535-545.

25. Mandl F. Statistical physics. Trowbridge: John Wiley & Sons; 1971. 385p.

26. Mattis DC. Statistical physics made simple. River Edge: World Scientific Publishing; 2003. 253p.

27. Jackson JD. Classical electrodynamics - third edition. New York: John Wiley & Sons; 1998. 808p.

28. Griffiths DJ. Introduction to electrodynamics. Upper Saddle River: Prentice-Hall; 1989. 532p.

29. Rabi II, Ramsey NF, Schwinger J. Use of rotating coordinates in magnetic Resonance problems. Rev Mod Phys 1954;26:167-171.

30. Liang ZP, Lauterbur PC. Principles of magnetic resonance imaging. New York: IEEE Press; 2000. 416p.

31. Bottomley PA, Andrew ER. RF magnetic field penetration, phase shift and power dissipation in biological tissue: implications for NMR imaging. Phys Biol Med 1978;23:630-643.

32. Schaefer DJ. Bioeffects of MRI and patient safety - AAPM summer school Proceedings. Woodbury: American Institute of Physics; 1993. 607-646p.

33. Solomon I. Relaxation processes in a system of two spins. Phys Rev 1955;99:559-565.

34. Bloembergen N, Purcell EM, Pound RV. Relaxation effects in nuclear magnetic resonance absorption. Phys Rev 1948;73:679-712.

35. Korb J, Bryant RG. Magnetic field dependence of proton spin-lattice relaxation times. Magn Reson Med 2002;48:21-26.

36. Bazelaire C, Duhamel G, Alsop D. NMR relaxation times in human abdominal tissues at 3.0 tesla. In Proceedings of the International Society for Magnetic Resonance in Medicine, Honolulu, Hawaii, 2002. p. 2292.

37. Haacke EM, Brown RW, Thompson MR, Venkatesan R. Magnetic resonance imaging - physical principles and sequence design. New York: John Wiley & Sons; 1999. 914p.

38. Chen L, Bernstein M, Huston J, Fain S. Measurements of T1 relaxation times at 3.0 T: implications for clinical MRA. In Proceedings of the International Society for Magnetic Resonance in Medicine, Glasgow, Scotland, 2001. p. 1391.

39. Lauterbur PC. Image formation by induced local interactions: examples employing nuclear magnetic resonance. Nature 1973;242:190-191.

40. Mansfield P, Grannell PK. NMR 'diffraction' in solids?. J Phys C 1973;6:422-426.

41. Kumar A, Welti D, Ernst RR. NMR fourier zeugmatography. J. Magn. Reson. 1975;18:69-83.

42. Brown MA, Semelka RC. MRI basic principles and applications. New York: John Wiley & Sons; 1995. 264p.

43. Nishimura DG. Magnetic resonance imaging. Stanford: Stanford University; 1996. 223p.

44. Hoult DI. The NMR receiver: a description and analysis of design. J Magn Reson Imaging 2000;12:46-67.

45. Alsop DC, Connick TJ, Mizsei G. A spiral volume coil for improved RF field homogeneity at high static magnetic field strengths. Magn Reson Med 1998;40:49-54.

46. Welch WJ. Reciprocity theorems for electromagnetic fields whose time dependence is arbitrary. IEEE Trans Antenna Propag 1960;8:68-73.

47. Jin J. Electromagnetic analysis and design. New York: CRC Press; 1999. 282p.

48. Sank VJ, Chen CN, Hoult DI. A quadrature coil for the adult human head. J. Magn. Reson. 1986;69:236-242.

49. Kramer J. Production of homogeneous fields. Brit J Appl Phys 1967;18:1815-1818.

50. Hoult DI, Phil D. Sensitivity and power deposition in a high-field imaging experiment. J Magon Reson Imaging 2000;45:46-67.

51. Kelter JR, Carlson JW, Roos MS, Wong STS, Wong TL, Budinger TF. Electromagnetic fields of surface coil in vivo NMR at high frequencies. Magn Reson Med 1991;22:467-480.

52. Edelstein WA, Foster TH, Schenck JF. The relative sensitivity of surface coils to deep lying tissues. In Proceedings of the International Society for Magnetic Resonance in Medicine, London, UK, 1985. p. 964-965.

53. Schneider HJ, Dullenkopf P. Slotted tube resonator: a new NMR head probe at high observing frequencies. Rev Sci Instrum 1977;48:68-73.

54. Sotgiu A, Gualtieri G, Passariello R. Highly homogeneous circularly polarized RF field for whole body NMR imaging. Magn Reson Imaging 1988;6:249-254.

55. Hayes CE, Edelstein WA, Schenck JF, Mueller OM, Eash M. An efficient highly homogeneous radiofrequency coil for whole body NMR imaging. J. Magn. Reson. 1985;63:622-628.

56. Baertlein BA, Ozbay O, Ibrahim T, Lee R, Yu Y, Kangarlu A, Robitaille PML. Theoretical model for an MRI radio frequency resonator. IEEE Trans BioMed Eng 2000;47:535-546.

57. Ginsberg DM, Melchner MJ. Optimum geometry of saddle shaped coils for generating a uniform magnetic field. Rev Sci Instrum 1970;41:122.

58. Tropp J. The theory of the bird cage resonator. J. Magn. Reson. 1989;82:51-62.

59. Tate Q, Bell LC, Kim SE, Minalga E, Parker DL, Hadley JR. A 16 channel radio frequency anterior neck coil for imaging of the cervical carotid bifurcation. In Proceedings of the International Society for Magnetic Resonance in Medicine, Stockholm, Sweden, 2010. p. 3841.

60. Hadley JR, Roberts JA, Goodrich KC, Buswell HR, Parker DL. Relative RF coil performance in carotid imaging. Magn Reson Imaging 2005;23:629-639.

61. Hinks RS, Constable RT. Gradient moment nulling in fast spin echo. Magn Reson Med 1994;32:698-706.

62. Pauly J, Le Roux P, Nishimura D, Macovski A. Parameter relations for the Shinnar-Le Roux selective excitation pulse design algorithm. IEEE Trans Med Imaging 1991;10:53-65.

63. Freeman R. Shaped radiofrequency pulses in high resolution NMR. J NMR Spect 1998;32:59-106.

64. Oppenheim AV, Schafer RW. Discrete time signal processing. Englewood Cliffs: Prentice Hall; 1989. 870p.

65. Roden MS. Analog and digital communication systems. Upper Saddle River: Prentice Hall; 1996. 560p.

66. Macovski, A. Noise in MRI. Magn Reson Med 1996;36:494-497.

67. Hoult DI, Lauterbur, PC. The sensitivity of the zeugmatographic experiments involving human sample. J Magn Reson 1979;34:425-433.

CHAPTER 2

TURBO SPIN ECHO ANGIOGRAPHY

Accurate identification of carotid atherosclerotic plaque composition can better identify those individuals at higher risk for subsequent cerebral embolization and neuralgic symptoms (1-4). MRI presents an advance over x-ray techniques, including Computed Tomography, because it produces images with a variety of different tissue contrasts. Because MRI can better discriminate soft tissue types, it offers improved discrimination of atherosclerotic plaque components such as hemorrhage, disrupted fibrous cap, lipid/necrotic core, calcification and ulceration. Turbo Spin Echo pulse sequences, with efficient acquisition of T1, T2 and proton density weighted images, have become useful in the evaluation of cervical carotid artery disease (5-7).

2.1 Turbo Spin Echo Sequences

Spin echo sequences, first described by Hahn in 1950, have the ability to refocus phase shifts caused by field inhomogeneities (8). A spin echo sequence is capable of providing proton density (PD), T1 (longitudinal relaxation) weighted and T2 (transverse relaxation) weighted images (9, 10). However, because spin echo sequences acquire just a single line of data with each excitation (every few seconds), the scan time is significantly longer than most other MRI sequences. One method of decreasing scan time is to acquire multiple lines in k-space after a single excitation while maintaining the

benefit of refocusing field inhomogeneities. The resulting sequence is known under different names as Rapid Acquisition with Relaxation Enhancement (RARE), fast spin echo (FSE) or, as it will be referred to in this thesis, turbo spin echo (TSE) (11, 12).

2.1.1 Spin Echo

The FID observed in a MRI experiment has contributions from numerous spins within the field of view of the receiver coil. A maximum signal will be observed only if all the contributing magnetization vectors are in phase with each other. Any phase distribution across the sample will cause destructive interference and the magnetization vectors must regain phase coherence to restore the FID to a maximum (Fig. 2.1). Except for some

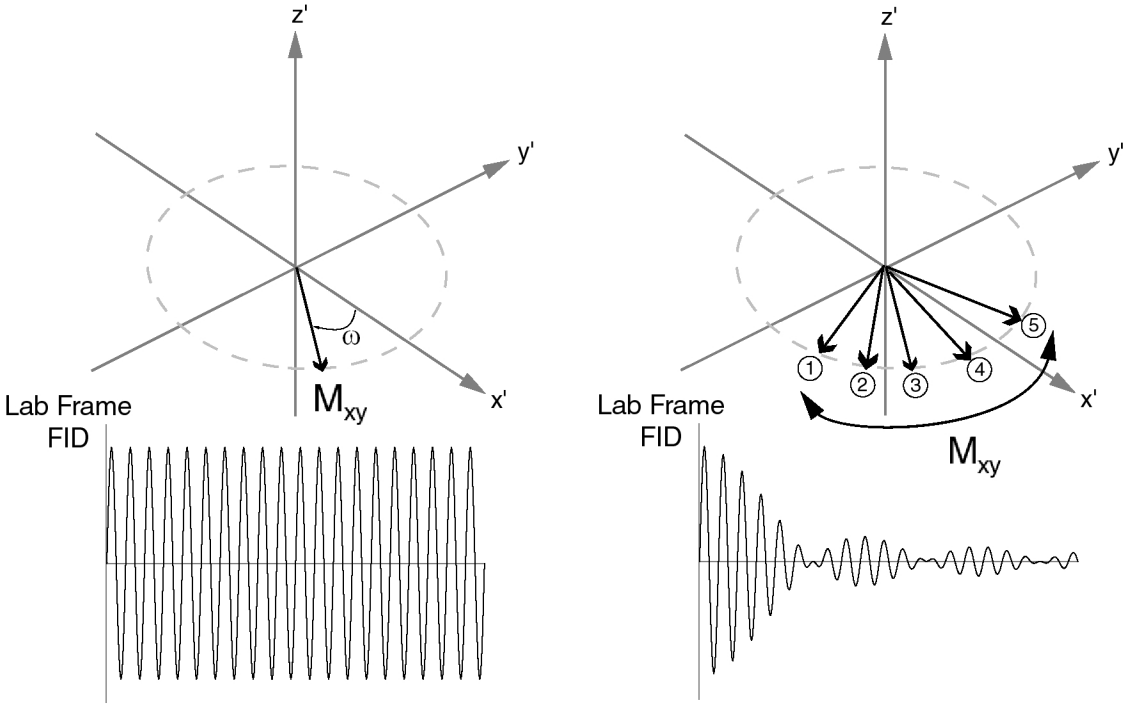

Figure 2.1: Dephasing of spins due to field inhomogenity. Neglecting T2 relaxation, when all the magnetization vectors are in phase (a) the FID signal does not suffer from any degradation over time. In contrast, when the magnetization vectors acquire a uniform phase distribution over time (b) the vectors destructively interfere producing the degraded FID signal shown.

irreversible relaxation, the rephased FID signal will resemble the original FID and is said to be an *echo* of the original signal. If the phase distribution is caused by the application of a gradient, then the phase distribution may be undone with a negative gradient and the resulting echo is labeled a *gradient echo*. A *spin echo* is formed when a phase distribution caused by magnetic field inhomogeneities or chemical shift is rephased. Since the field inhomogeneities and chemical shift mechanisms cannot be reversed like a gradient field, another method of rephasing the magnetization vectors is required. In this case a refocusing (180°) RF pulse is applied to the spins. The RF pulse has the effect of reversing any phase accumulation each spin acquired prior to the pulse (Fig. 2.2a). The

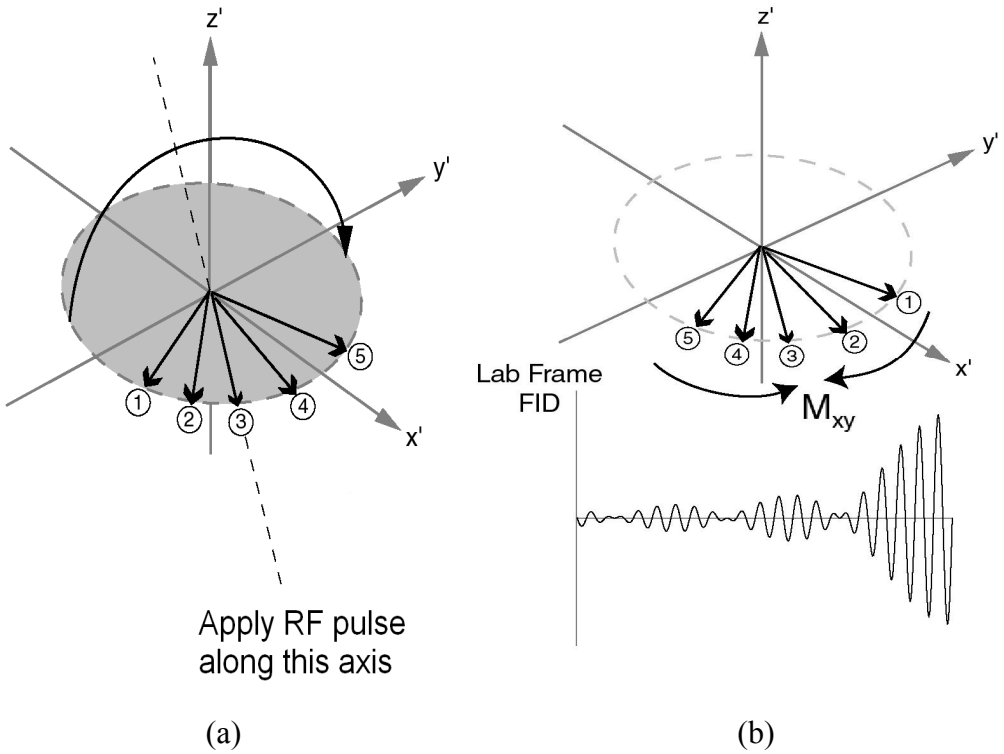

Figure 2.2: Rephasing of spins due to a refocusing RF pulse. The magnetization vectors ① through ⑤ have a phase distribution acquired over some time, τ (see Fig. 1.11b). A refocus RF pulse effectively flips the transverse plane along the dashed line in (a). The magnetization vectors have any acquired phase inverted. As the magnetization vectors continue to acquire phase they will rephase a time period τ after the refocus pulse.

field inhomogeneity remains unchanged such that spins precessing faster than ω_0 before the RF pulse will continue to precess faster. Over time the spins will rephase and a maximum FID, or echo, will be formed (Fig. 2.2b).

2.1.2 Multiple Echoes

Once the magnetization vectors rephase, they will continue acquiring phase and once again the FID signal will degrade. The FID signal can be rephased back to a maximum value by repeating the whole procedure with another refocusing pulse. However, transverse relaxation is a nonreversible process and is not negligible in a MRI experiment. Consequently, although the reversible component of relaxation is undone when an echo is formed, each successive echo will still suffer from the effects of the non-reversible T_2 relaxation (Fig 2.3). The ability of a spin echo to refocus the phase distribution caused by local field inhomogeneities make it a desirable mechanism in MRI experiments. Typically, each time the phase distribution of spins is refocused another line of k-space data is acquired.

A sequence that utilizes a full excitation pulse ($\pi/2$ or 90° flip angle) followed by a train of π refocus pulses (180° flip angle) with the same phase as the excitation pulse is labeled a Carr-Purcell sequence (13). In practice, all of the spins within the excited volume see a range of flip angles. Repeated application of non-perfect refocus pulses will lead to cumulative errors that can be lessened with the use of a phase cycling scheme. This correction is implemented by shifting the phase of the RF refocus pulses by $\pi/2$ from the excitation pulse and labeled a Carr-Purcell-Meiboom-Gill (CPMG) sequence (14). Despite the improved performance, a CPMG sequence is not immune to the effects of varying refocus flip angles.

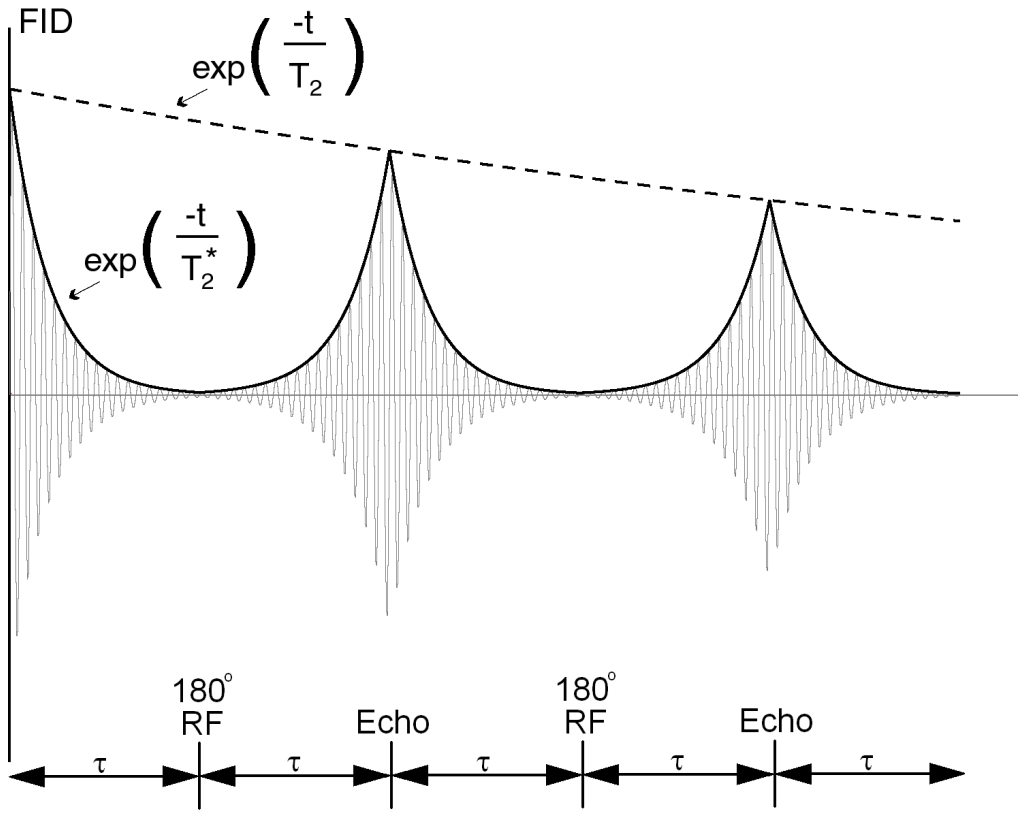

Figure 2.3: FID from repeated formation of spin echoes. The FID signal has a decay envelope that is governed by the time constant T_2^*. This envelope has reversible (T_2') and non-reversible (T_2) components. The reversible component can be rephased and the lost signal can be recovered through an echo. Diffusion effects have been neglected.

2.1.3 Stimulated Echoes

Although each additional RF refocus pulse is able to create a spin echo, phase memory will lead to the creation of additional stimulated echoes (15). Phase memory is a mechanism in which the phase of a magnetization vector at some previous time period is retained and later recalled. An example of how this might occur is shown in Fig. 2.4. The total number of echoes, both stimulated and spin, produced by N_{RF} pulses is (16):

$$N_{echo} = \frac{3^{N_{RF}} - 2N_{RF} - 1}{4}. \qquad [2.1]$$

For example, a MRI experiment with 3 RF pulses can produce a total of five echoes (four

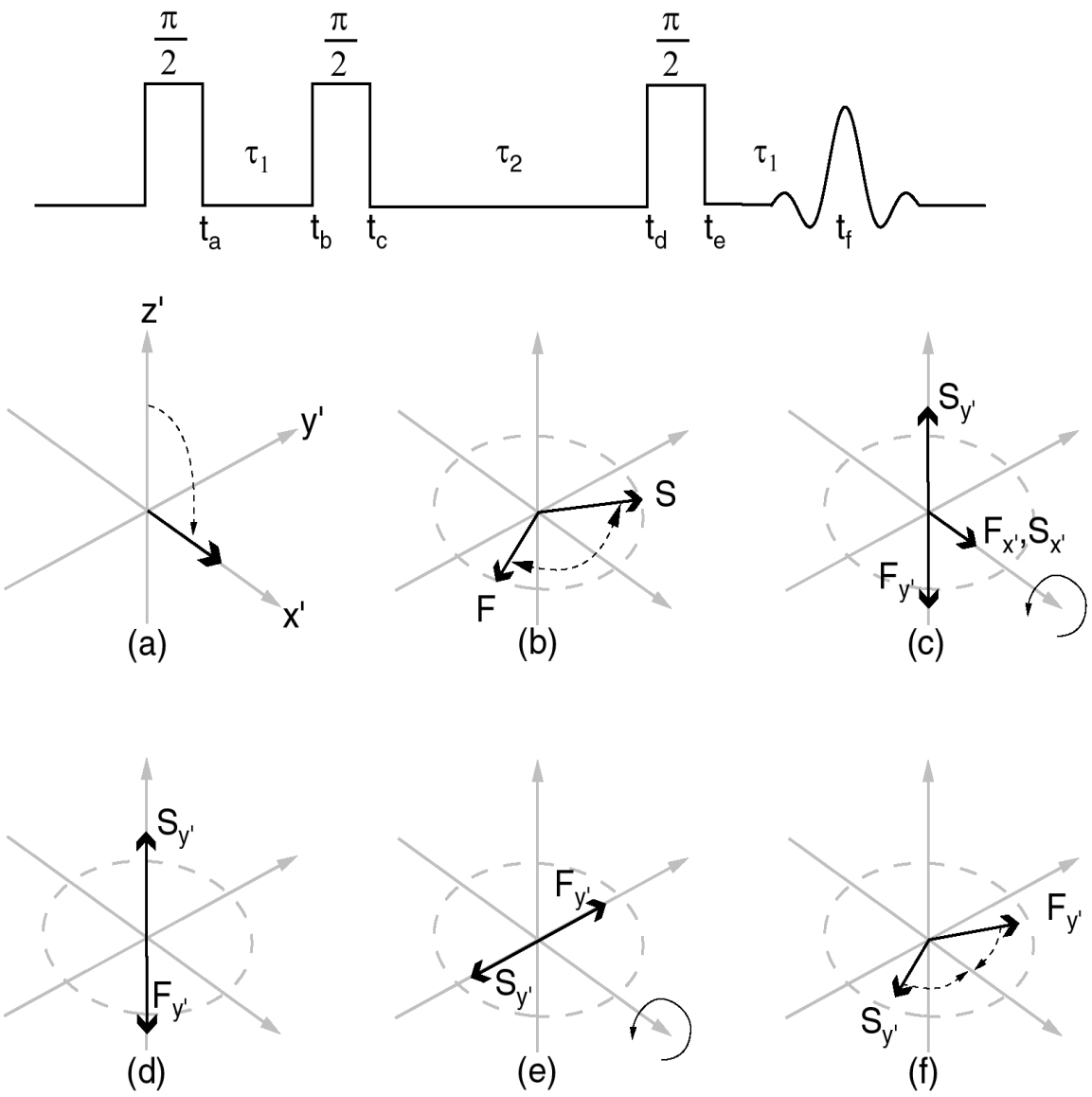

Figure 2.4: A NMR experiment with three π/2 RF pulses will create both stimulated and spin echoes. The first RF pulse excites the magnetization along the x'-axis (a). During the first time period τ_1 (b) a fast spin (F) and slow spin (S) will acquire and lose phase in the rotating frame respectively. A second RF pulse in (c) will flip the y'-components of the spins along the z'-axis leaving the x'-components in the transverse plane. For the period of time τ_2 both the transverse and longitudinal components will relax with their corresponding relaxation times. Considering just the y'-components (d), when the third RF pulse is applied, the y'-components will be brought back into the transverse plane (e). The fast spin will continue to acquire phase and the slow spin will continue to lose phase and the spins will rephase a time τ_1 later producing a stimulated echo (f).

spin echoes and one stimulated echo). Figure 2.5 shows the location of the five echoes. The number of RF pulses in a TSE sequence could easily be as high as 16 or more. In this case the number of potential echoes is 10761672 and special care must be taken in sequence design to prevent such echoes from creating problems. One method to reduce the effect of stimulated echoes is to create a large gradient moment just before a refocus pulse and then undo that moment just after the pulse. However, it is also possible to design a sequence that allows the stimulated echoes to constructively add to the spin echoes.

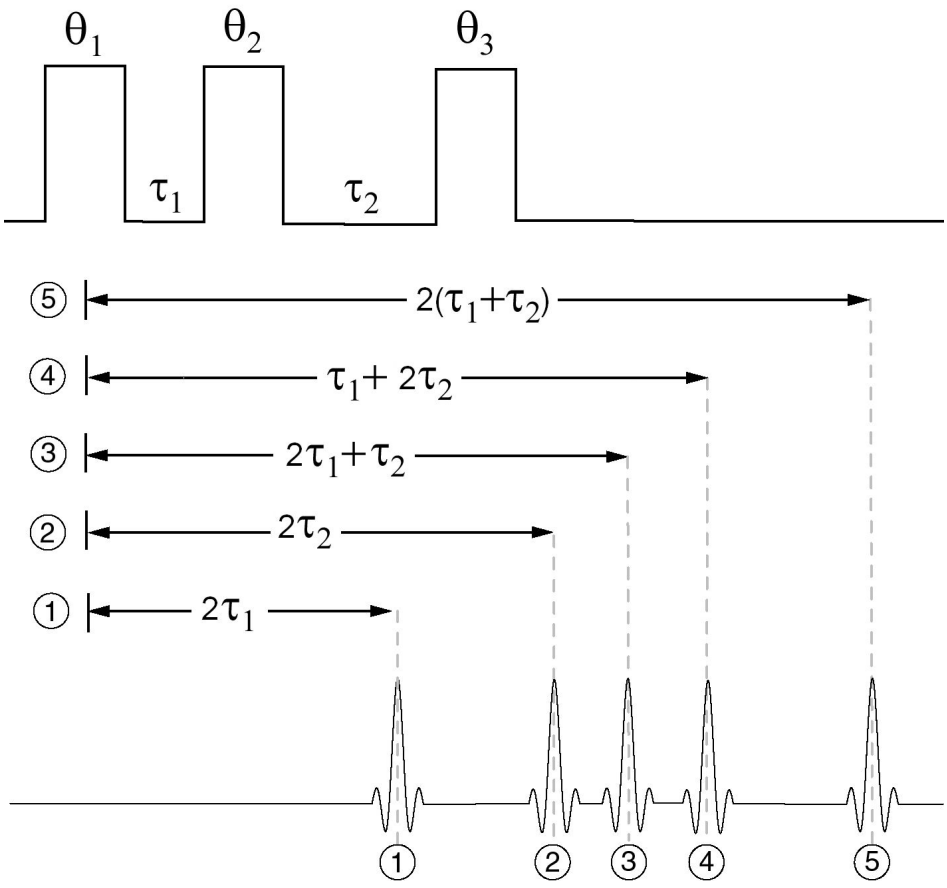

Figure 2.5: Echo generation in a MRI experiment. Three RF pulses can generate as many as five echoes. The magnitude of the various echoes depends on the flip angle of the RF pulses. If the last two pulses are perfect refocusing pulses, then only two spin echoes will remain.

2.1.4 Gradient Moment Nulling

If the gradient waveform is selected such that:

$$\phi^n = \frac{\gamma}{n!}\int \mathbf{G}(t)\cdot \mathbf{r}_n t^n dt = 0 \qquad [2.2]$$

then the n^{th} moment of the gradient is said to be nulled (17). If the n^{th} moment of the gradient is nulled, then a spin will not have any gradient induced phase shifts due to the n^{th} moment of motion. In many MR applications the tissue is assumed to either be stationary or to have an approximately constant velocity. Consequently only the 0^{th} and 1^{st} gradient moments are normally given attention. In addition, a gradient is designed to be nulled at a certain point in time, typically during the middle of the acquisition window or at the moment of the refocus RF pulse. Gradient moment nulling can be used to maximize/minimize the signal from stationary or moving tissue. For example, if gradients are designed to only have a nulled 0^{th} moment, moving tissue such as flowing blood will become dephased and have minimized signal. This makes gradient moment nulling an important design concept in MR sequences used in angiography.

2.1.5 Gradient Configurations

Figures 2.6 through 2.8 indicate how gradient timings would coordinate with the RF excitation and refocus pulses along with the data acquisition (often labeled as ADC for Analog to Digital Converter). In each case only two echoes are shown but the process could be continued for as many echoes as desired (typically 7-12 echoes).

Figure 2.6 shows some slice gradient configurations. The primary purpose of the slice gradient is to perform selective excitation and refocusing of tissue. In 3D sequences, the slice gradient also performs spatial encoding in the slice direction. The

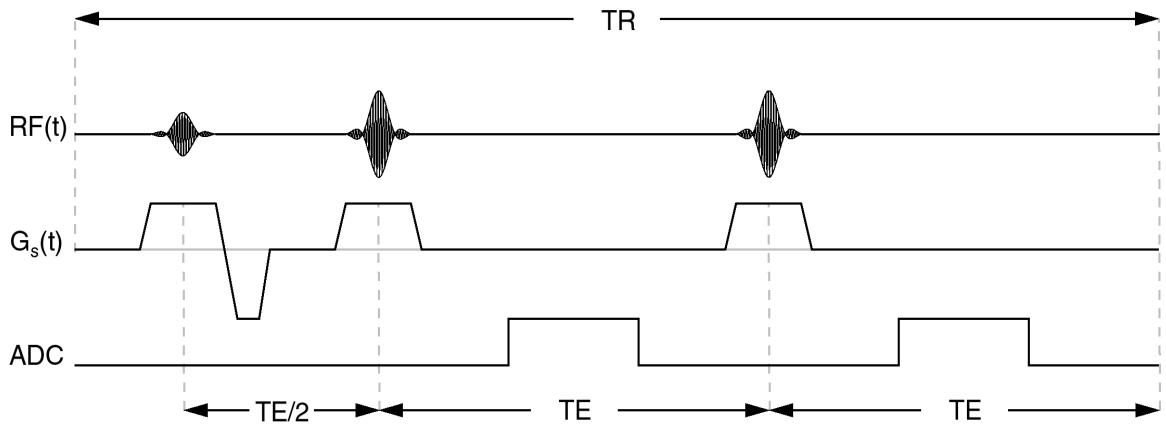

(a)

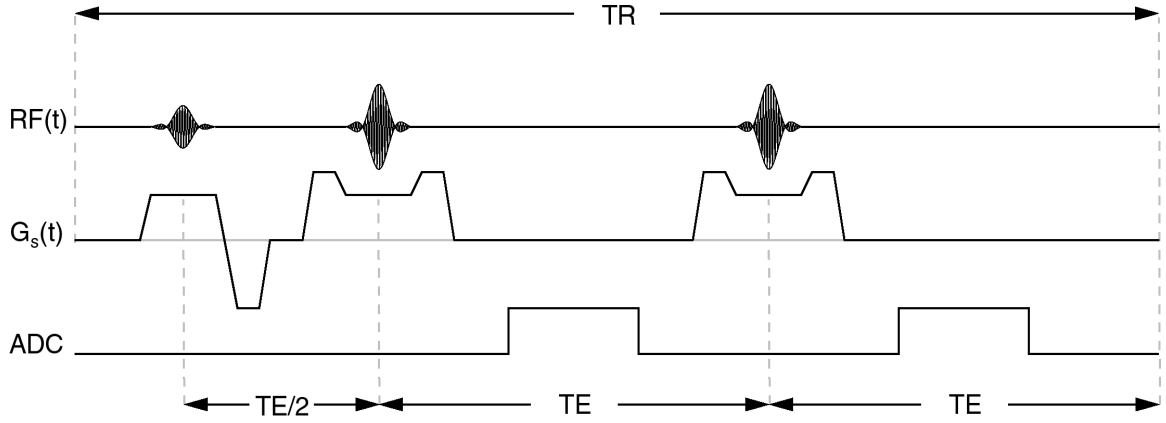

(b)

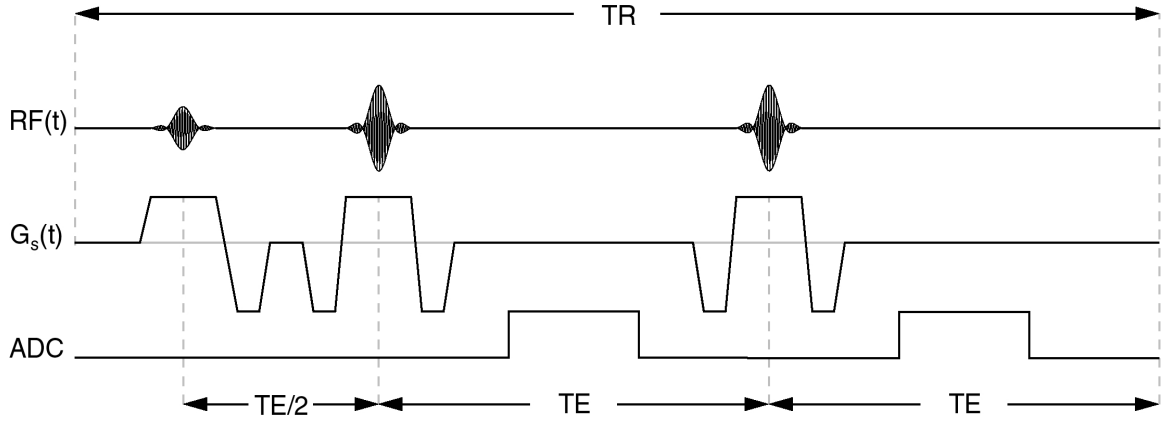

(c)

Figure 2.6: Basic slice select gradient configurations. The most basic configuration is shown in (a). In (b), crusher gradients are added with flow compensated crushers shown in (c).

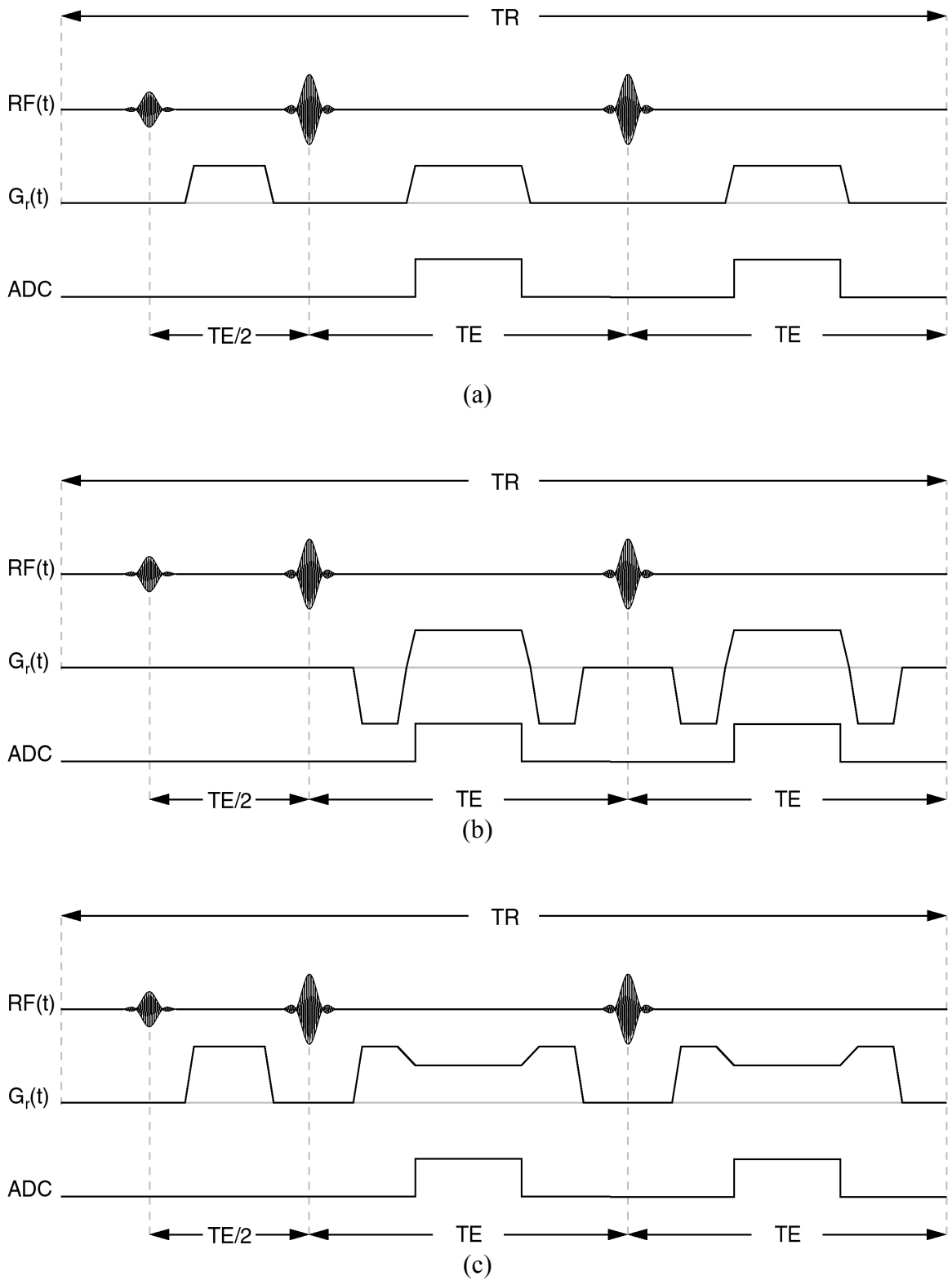

Figure 2.7: Basic read gradient configurations. The most basic configuration is shown in (a). In (b) the read gradients are flow compensated and in (c) crusher gradients are added to suppress signal from flowing spins.

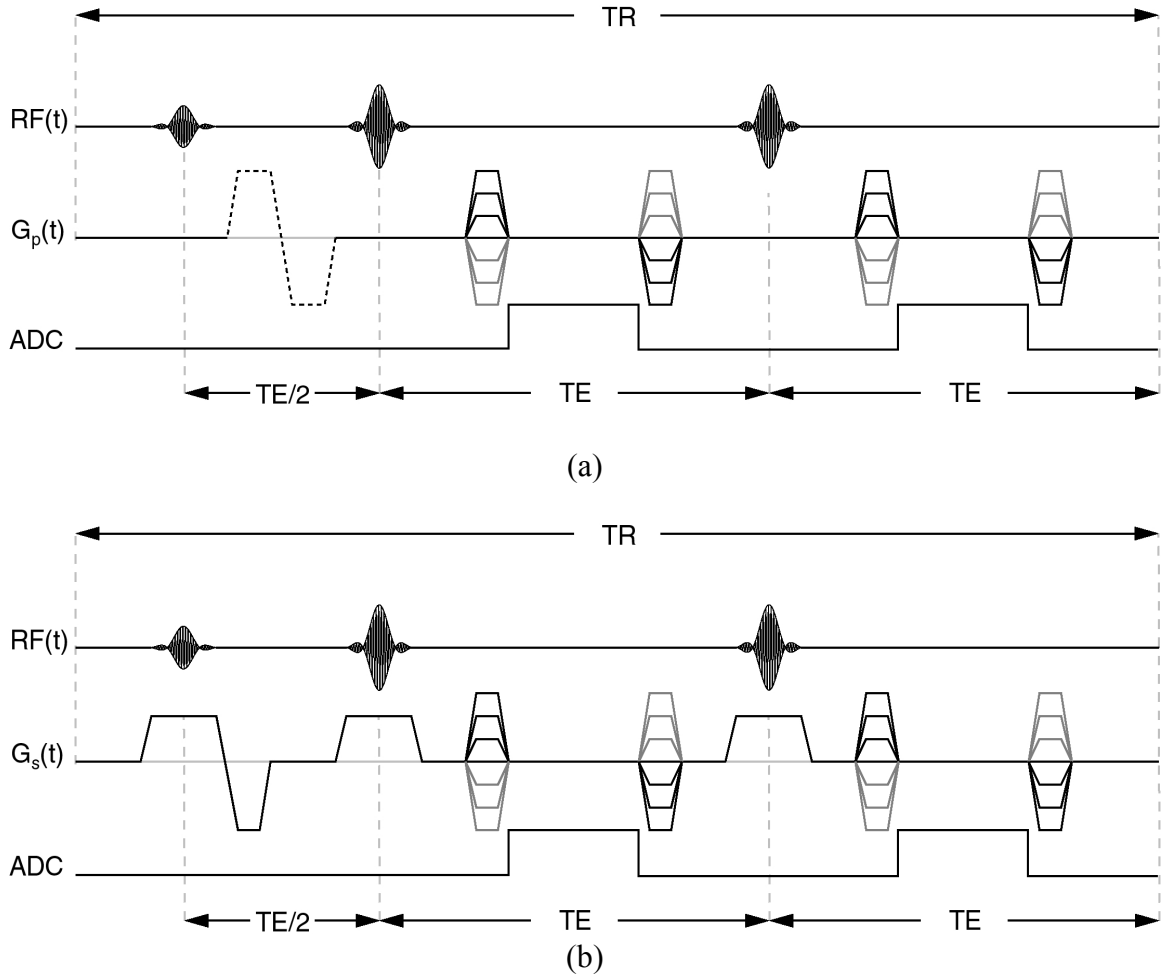

Figure 2.8: Phase encode gradients for a TSE sequence. The basic phase encode gradients are shown in (a). For 3D sequences, spatial information must also be encoded in the slice direction as shown in (b). For comparison, see the slice gradient without spatial encoding in Fig. 2.6a.

most basic configuration, and the one allowing for the shortest echo spacing, is shown in Fig. 2.6a. However, due to imperfect RF pulses, this configuration is rarely employed. In Fig. 2.6b, crusher gradients help reduce the effect of non-perfect slice profiles. The crusher gradients in Fig. 2.6b are not flow compensated and would tend to also suppress signal from moving spins such as blood. The final slice configuration, Fig. 2.6c, shows the implementation of crusher gradients that are flow compensated. This configuration

helps preserve the signal from flowing spins.

Figure 2.7 shows some read gradient configurations. The primary purpose of the readout gradient is for frequency encoding (spatial localization). Again, the most basic configuration, and the one allowing for the shortest echo spacing, is shown in Fig. 2.7a. In Fig. 2.7b, the readout is flow compensated while in Fig. 2.7c the crusher gradients will suppress signal from moving spins during data acquisition. Finally, the basic phase encode gradients are shown in Fig. 2.8a. The optional bipolar pulse (dashed line in Fig. 2.8a) is useful to help suppress signal from flowing spins. For 3D sequences, spatial information must also be encoded in the slice direction as shown in Fig. 2.8b.

2.2 Carotid Artery Imaging

Atherosclerosis is a thickening of an artery wall as the result of a build-up of fatty materials. Carotid atherosclerotic disease has been proven to increase the risk of ipsilateral ocular or cerebral stroke (18). Stroke is the leading cause of adult neurological disability and the third leading cause of death in the United States (18). Between 1940 and 1990 the death rate due to stroke in North America doubled and continues to increase. The plaque components in a diseased artery have been found to correlate with the incidence or risk of cerebral symptoms (19, 20). As a result, this thesis is aimed particularly on improving the ability to image the carotid artery.

2.2.1 Basic Anatomy

The carotid arteries are the main arteries in the neck that supply oxygenated blood to the brain (Fig. 2.9). The left and right arteries have different origins but are otherwise paired structures. The left carotid artery originates from the aortic arch while the right

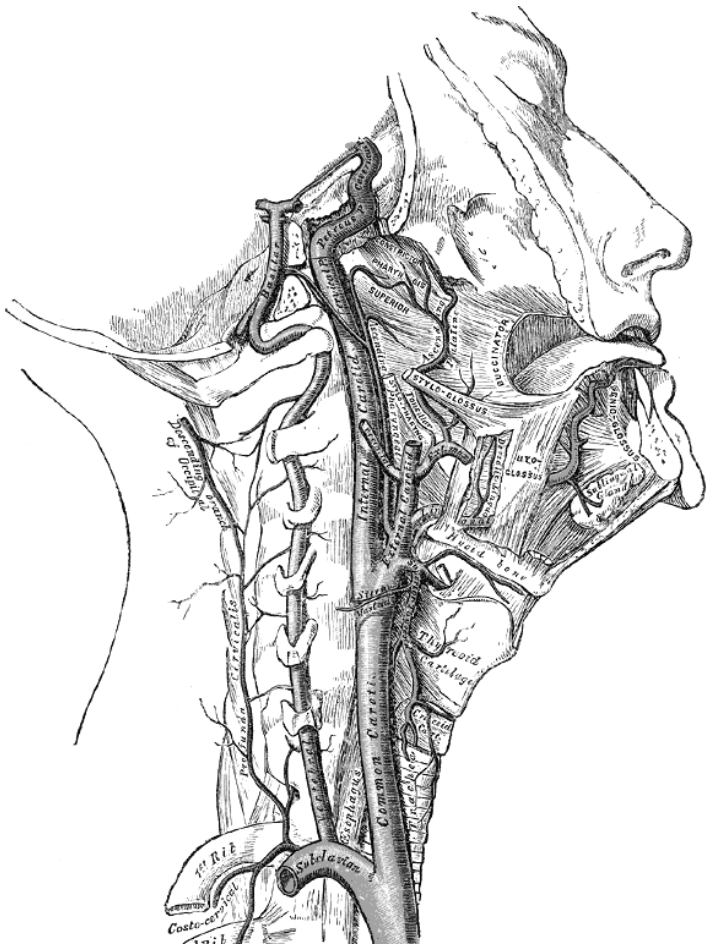

Figure 2.9: Carotid artery engraving from Gray's Anatomy of the Human Body 1918 edition (public domain).

carotid originates in the neck from the brachiocephalic trunk. The common carotid artery branches into an internal and an external branch near the fourth cervical vertebra. The internal carotid primarily supplies blood to the brain while the external carotid supplies blood to the neck and face.

2.2.2 Disease Progression

Atherosclerosis begins when low-density lipoprotein molecules (LDL) invade the endothelium of the normal artery wall (Fig. 2.10a) and become oxidized (21). This initial

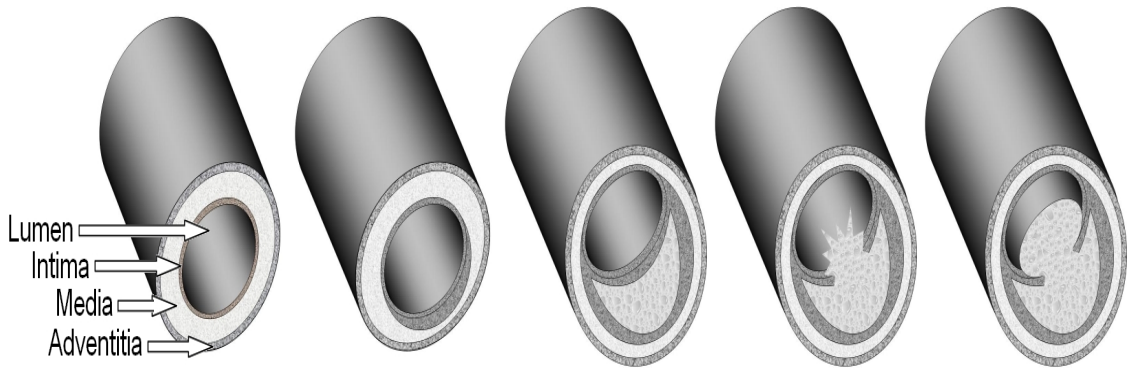

(a) (b) (c) (d) (e)

Figure 2.10: Cross section of an artery in various stages of carotid disease. A normal artery (a) first obtains fatty streaks (b) followed by expansion to compensate for the fatty deposit (c). The plaque may then rupture (d) and if progression continues the rupture will seal off with a fibrous cap causing a greater stenosis (e).

damage creates an inflammatory response attracting monocytes into the wall. These monocytes differentiate into macrophages which absorb the oxidized LDL to become foam cells. This lesion of foam cells appears as a fatty streak (Fig. 2.10b). Foam cells are not able to process the oxidized LDL and eventually die releasing the stored oxidized LDL. This propagates the inflammatory response of the endothelial cells in the artery wall. A protective fibrous cap forms between the fatty deposits and the artery lining. The trapped fatty deposits encourage production of enzymes that cause the artery to expand to maintain a normal artery diameter (Fig. 2.10c) (22). Eventually the artery can't expand anymore and the plaque may rupture (Fig. 2.10d). If the plaque ruptures, there is immediate clotting at the site of the ulceration which may obstruct blood flow and result in a stroke. If the disease is allowed to progress, a fibrous cap will seal the rupture but lead to a narrowing of the artery known as stenosis (Fig. 2.10e). Areas of the artery with changes in shear stress and blood pressure may cause a delay in the transport of atherogenic particles (such LDL). As such, there is more time for these particles to penetrate into the artery wall and contribute to plaque formation. Because the carotid

bifurcation is such an area with complex flow, it is a region of interest when examining carotid disease.

2.2.3 Generating Contrast

The trajectory along which k-space data is acquired is referred to as the *phase encode order*. The central portion of k-space will contribute primarily to the contrast of the MR image while the outer portion will primarily contribute to the resolution and detail of the image. Thus, encoding certain echoes to be near the center of k-space is one of several methods used to obtain contrast in TSE sequences (9, 23). Figure 2.11 shows the expected transverse signal of muscle and fat for each of seven echoes (represented by the dotted vertical lines) in an echo train. If the first echo (①) were used to encode the central portion of k-space, the fat and muscle intensities would be similar and little T2 contrast would be present in the final image. If, however, the 5th echo (⑤) were used to encode the center of k-space, the fat intensity would be about twice that of muscle.

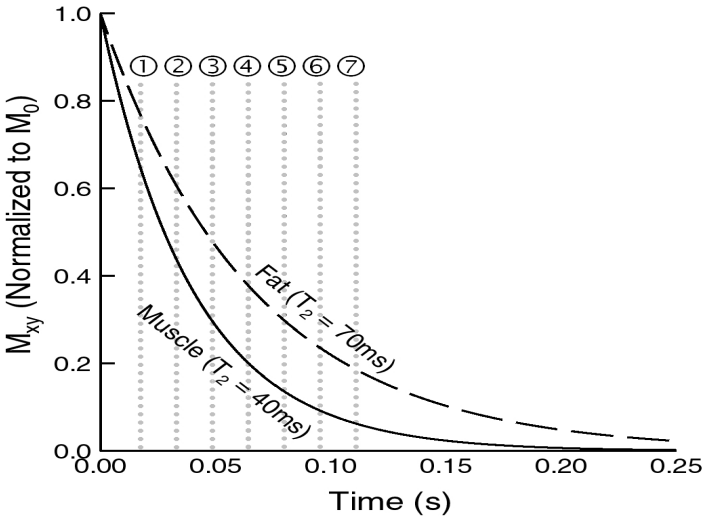

Figure 2.11: Phase encode order for T2 contrast. If the 1st echo, labeled ①, encodes the central portion of k-space there will be little T2 contrast. Increased contrast would result by instead choosing the 5th echo, labeled ⑤, to encode the central portion of k-space.

Figure 2.12 demonstrates how varying the echo time changes the contrast in a TSE head image. Analogously, the time allowed for tissue to return to thermal equilibrium before the next excitation is important. For example, gray matter (T1=1.45s @ 3T) will recover to equilibrium slower than white matter (T1=0.8s @ 3T). If the time between excitations is kept short (< 1s) then white matter will have more signal intensity than gray matter in the images. Consequently, two important parameters in TSE sequences that vary contrast are the repetition time (TR) and the echo spacing (TE). The TR is the time between echo trains and determines how long the magnetization is allowed to return to thermal equilibrium before another excitation begins. The TE is the time between the initial excitation and the time the central portion of k-space is encoded. For proton density images, TR is kept long to prevent T1 contrast and TE is kept short to prevent T2 contrast. A T1 weighted image is obtained with a short TR and TE. A T2 weighted image is obtained with a long TR and an increased TE. Hence, a TSE sequence can be

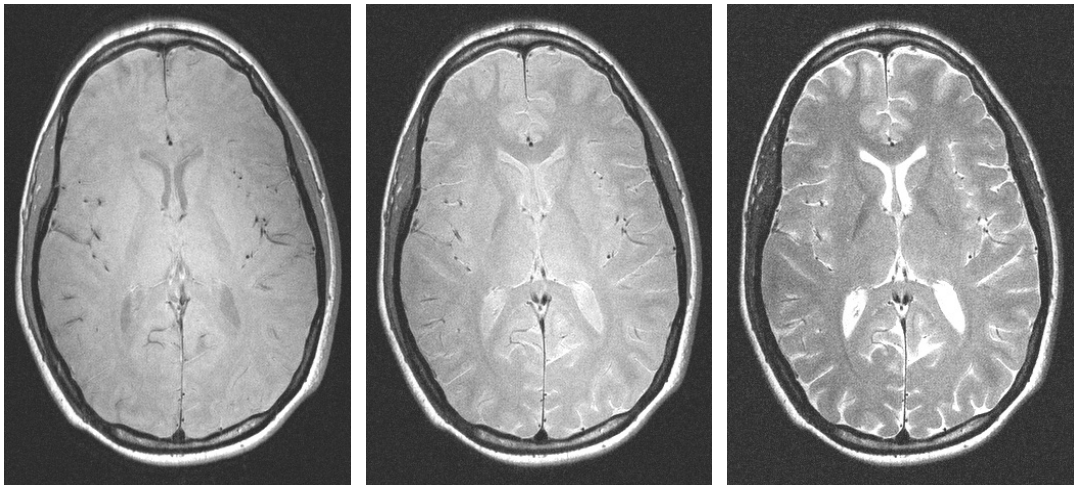

(a) (b) (c)

Figure 2.12: Tissue contrast as a function of echo time. The TSE brain images were acquired with (a) TE=10ms, (b) TE=40ms and (c) TE=80ms.

tailored to provide optimum contrast for specific tissues based on their relaxation times. The relaxation times for select plaque components are given in Table 2.1.

In addition to determining which echo should encode the central portion of k-space, the modulation of signal across k-space is an important factor. If the phase encode order was linear across k-space, then the signal modulation would be similar to that in Fig. 2.13. This modulation would create artifacts in the reconstructed image and needs to be avoided. To overcome this problem, the views are phase encoded in an order such that echoes with similar amplitudes are encoded next to each other in k-space. This results in a smoother modulation of the k-space data and a significant reduction in the amount of image ghosting. It is possible to perform this grouping and still specify TE (which echo should encode the central portion of k-space). Figure 2.14 shows three situations with smooth k-space modulations and varying echo times.

2.2.4 Black Blood Imaging

The color label of a MRA technique refers to the signal intensity of the blood in the image. MR images are usually displayed with a gray scale that associates white with the highest signal intensity and black with the lowest signal intensity. White blood images result from blood vessels that have maximum signal intensity with surrounding tissue saturated to a minimum value. Black blood images attempt to reduce the blood signal as

Table 2.1: MR relaxation constants of select plaque components

Component	T_1 (ms)	T2 (ms)	$T2^*$ (ms)
Fibrous Cap[a]	560	30	26
Loose Matrix[a]	1070	43	29
Lipid Rich Necrotic Core[a]	820	34	19
Intra-Plaque Hemorrhage[a]	120	16	8

[a]Source (24).

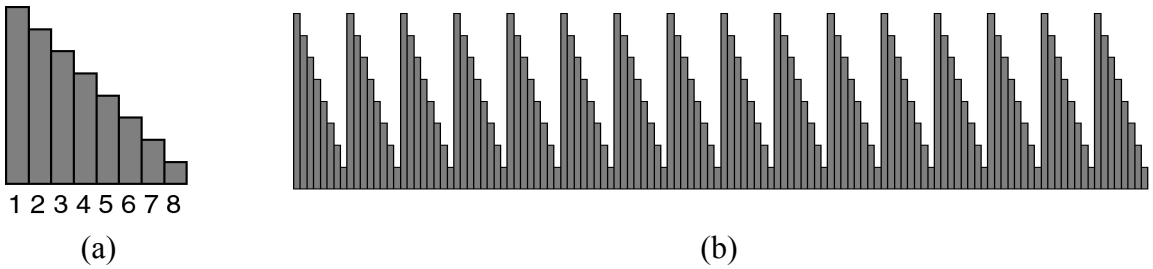

Figure 2.13: K-space modulations due to a linear phase encode order. The amplitude of each echo in an echo train is shown in (a) with the resulting k-space modulation from a linear encode order (b).

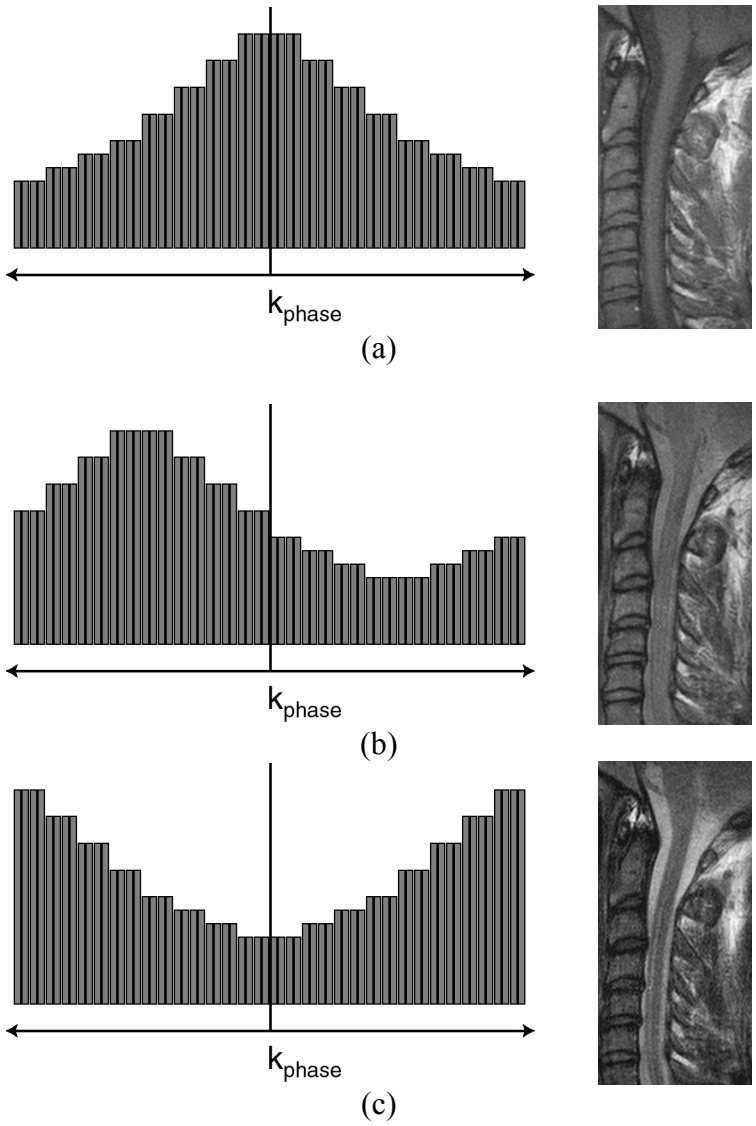

Figure 2.14: K-space modulations and resulting TSE spine images. The echo times were (a) TE=9.7ms, (b) TE=33.8ms and (c) TE=77.6ms.

much as possible while maintaining a maximum signal from the background (Fig. 2.15). The black blood technique is particularly useful for vessel wall imaging as it preserves the signal from the surrounding tissue (25-29). Black blood techniques usually rely on suppression of blood through gradient dephasing (30), saturation and inversion preparation techniques or a combination of these (31).

2.2.5 Blood Signal Saturation

Once a magnetization vector is excited, there is a necessary time period governed by T1 for the magnetization to return to thermal equilibrium. If the magnetization vector is excited before it returns to thermal equilibrium then the resulting transverse magnetization will only be a fraction of the thermal equilibrium value. A spin is saturated if little or no signal results from an excitation because the spin is still recovering from a previous excitation. In Angiography, saturation involves exciting a slice of spins

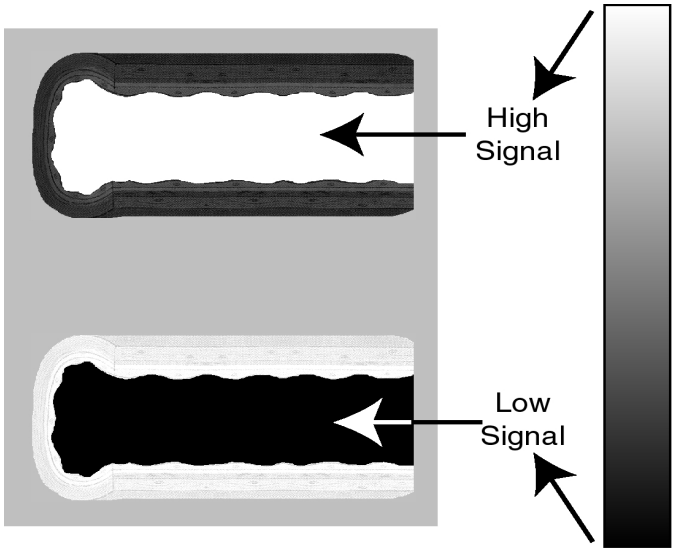

Figure 2.15: Black versus white blood imaging. The right bar indicates the range of gray scale colors used to represent high and low signal intensities in the images on the left. In a white blood image (top) the high intensity blood signal is contrasted with the reduced signal of the saturated background tissue. The black blood image (bottom) has bright surrounding tissue while the signal from blood is reduced to a minimum.

offset from the imaging slice in a direction opposite the blood flow. There is then a time delay to allow the saturated blood spins to flow into the imaging slice at which time the image slice is excited. The spins from the blood have not fully recovered from the previous saturation pulse and will consequently have a lowered transverse magnetization (Fig. 2.16). One problem with relying solely on saturation bands for blood suppression is that only the saturated spins within a specified range of velocities will appear inside the image slice during excitation. Spins with slower flow will not make it to the image slice while spins with greater velocities will pass completely through the image slice. The range of velocities that are saturated can be tailored by the size and placement of the saturation band.

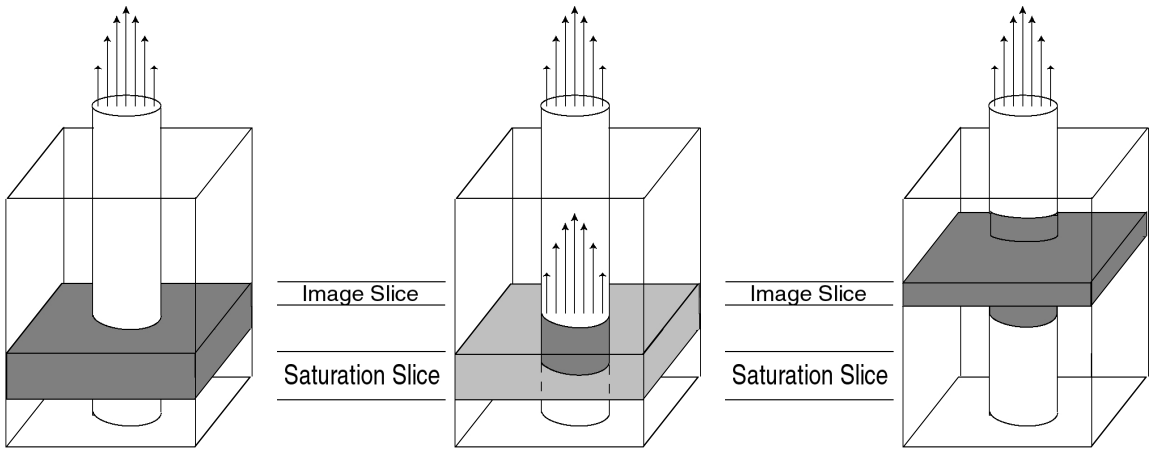

Figure 2.16: Suppression of blood using a saturation band. In (a) a slice of spins are fully excited by a saturation pulse. The saturated spins are then allowed to flow into the image slice (b). After the short delay, the slice is imaged as normal. The spins in the stationary tissue did not receive the saturation RF pulse and will have full signal intensity. The spins from the blood that received the saturation pulse will have not fully recovered and will have reduced signal.

2.2.6 Inversion Preparation

The relaxation time of blood is longer than most other surrounding tissues. This property can be exploited to suppress the signal from blood using inversion recovery. The basic technique employs an inversion pulse to align the magnetization of all tissue along the negative z'axis. Each tissue will then recover to thermal equilibrium according to its longitudinal relaxation time. At a characteristic time, called the inversion time (TI), the magnetization is excited. If TI is chosen as:

$$TI = \ln(2) \cdot T1_{Blood} \qquad [2.3]$$

then the signal from blood will be nulled at the expense of reduced signal from other tissues (Fig. 2.17). To be effective in nulling flowing blood, the inversion pulses are non-selective (they invert all the spins in the object). The negative consequence is that after an echo train of data is acquired, all the spins need time to return to thermal equilibrium and no interleaving of slices can be done.

To overcome the limitation of reduced signal from inversion recovery, a double inversion technique can be utilized (6). In this case, the entire object is inverted and then the image slice is immediately inverted back to equilibrium. The same inversion time is used to null the blood. The stipulation in this case is that the small amount of blood in the image slice flow out of the slice during the inversion time. This technique is still inherently inefficient since the entire object is inverted and must return to equilibrium between each echo train. Some variations have been proposed to interleave a small number of slices, but the scan time is still significantly longer than a nonprepared TSE sequence (32). Another setback of double inversion recovery is that only spins with a single relaxation time can be nulled. The T1 of blood varies with temperature, hematocrit

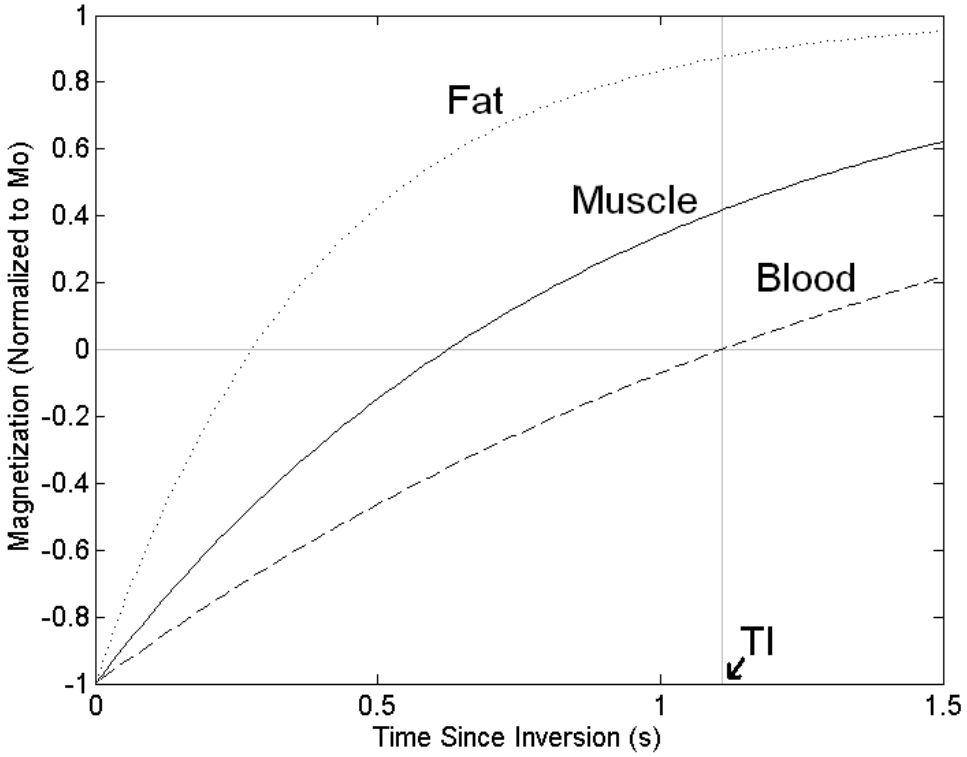

Figure 2.17: Inversion recovery preparation to suppress blood. A system of spins that is inverted will recover according to individual relaxation times. After a time TI, the spins are re-inverted with the blood signal remaining nulled.

fraction and injection of contrast media making it tough to design an optimal inversion time for clinical use (33). Quadruple inversion recovery is a technique that aims to null spins with a range of T1 times (34).

2.2.7 Fat Saturation

In addition to the static magnetic field, a nucleus also experiences local magnetic fields caused by its chemical environment. Orbiting electrons produce a magnetic field that, in general, opposes the main static magnetic field. Since the resonant frequency of a nucleus is dependent on the net magnetic field, this shielding of H_0 will result in a lowered resonant frequency. This phenomenon is called chemical shift and is measured

using a ppm (parts per million) ratio:

$$\delta = \frac{\omega - \omega_{ref}}{\omega_{ref}} 10^6 \qquad [2.4]$$

where δ is the field-independent scalar ratio (in ppm) between the resonant frequency of interest ω and a reference frequency ω_{ref} (35). The hydrogen nuclei in water are bound to a single oxygen atom while the hydrogen nuclei in fat are bound to a carbon atom. The oxygen atom more strongly attracts the electrons of the hydrogen nuclei, compared to the carbon atom, resulting in less electron shielding of the hydrogen atoms. Consequently, protons in the hydrogen atoms bound to oxygen see a higher magnetic field and have a higher Larmor frequency. At 3.0 Tesla the resonant frequency of hydrogen nuclei in water is approximately 440 Hertz above the resonant frequency of hydrogen in lipid. This frequency offset is small enough that both lipid and hydrogen nuclei will be excited during slice selection, although there is a small shift in the slice selection direction for lipids relative to water depending on the bandwidth of the RF pulse. Consequently, there is a shift between the excited water and fat slices given as:

$$\Delta z = \frac{SliceThickness}{BW_{RF}} \cdot FatOffset \qquad [2.5]$$

In addition, during frequency encoding this shift frequency will lead to a displacement of the fat relative to the water in the images. This is one of the reasons why a wide array of MR techniques have been designed to reduce or remove the fat signal from an image (36, 37).

One common technique is spectral saturation. This method of fat suppression requires just one additional RF pulse, applied with the appropriate frequency offset, prior to the imaging block of the sequence. The off-resonance pulse saturates the fat signal but

leaves the water signal relatively unchanged.

2.3 References

1. Fox AJ. How to measure carotid stenosis. Radiology 1993;186:316-318.

2. North American Symptomatic Carotid Endarterectomy Trial Collaborators. Beneficial effect of carotid endarterectomy in symptomatic patients with high-grade carotid stenosis. N. Engl. J. Med. 1991;325:445-453.

3. European Carotid Surgery Trialists' Collaborative Group. MRC European carotid surgery trial: interim results for symptomatic patients with severe (70-99%) or with mild (0-29%) carotid stenosis. Lancet 1991;337:1235-1243.

4. Executive Committee for the Asymptomatic Carotid Atherosclerosis Study. Endarterectomy for asymptomatic carotid artery stenosis. JAMA 1995;273:1421-1428.

5. Fayad ZA, Fuster V, Nikolaou K, Becker C. Computed tomography and magnetic resonance imaging for noninvasive coronary angiography and plaque imaging: current and potential future concepts. Circulation 2002;106:2026-2034.

6. Edelman RR, Chien D, Kim D. Fast selective black blood MR imaging. Radiology 1991;181:655-660.

7. Edelman RR, Mattle HP, Wallner B, Bajakian R, Kleefield J, Kent C, Skillman JJ, Mendel JB, Atkinson DJ. Extracranial carotid arteries: evaluation with "black blood" MR angiography. Radiology 1990;177:45-50.

8. Hahn EL. Spin echoes. Phys Rev 1950;80:580-594.

9. Constable RT, Anderson AW, Zhong J, Gore JC. Factors influencing contrast in fast spin-echo MR imaging. Magn Reson Imaging 1992;10:497-511.

10. Melki P, Mulkern RV, Dacher JN, Hélénon O, Higuchi N, Oshio K, Einstein S, Jolesz F, Pourcelot L. Fast spin echo MRI techniques: contrast characteristics and clinical potentials. J Radiol 1993;74:179-190.

11. Hennig J, Nauerth A, Friedburg H. RARE imaging: a fast imaging method for clinical MR. Magn Reson Med 1986;3:823-833.

12. Hennig J, Friedburg H. Clinical applications and methodological developments of the RARE technique. Magn Reson Imaging 1988;6:391-395.

13. Carr HY, Purcell EM. Effects of diffusion on free precession in nuclear magnetic resonance experiments. Phys Rev 1954;94:630-638.

14. Meiboom S, Gill D. Modified spin-echo method for measuring nuclear relaxation times. Rev Sci Instr 1958;29:688-691.

15. Plewes DB, Bishop J. Spin-echo MR imaging - AAPM summer school proceedings. Woodbury: American Institute of Physics; 1993. 166-187p.

16. Hennig J. Echoes - how to generate, recognize, use or avoid them in MRI sequences - part I. Concepts in Magn Reson 1991;3:125-143.

17. Hinks RS, Constable RT. Gradient moment nulling in fast spin echo. Magn Reson Med 1994;32:698-706.

18. Chu B, Ferguson MS, Underhill H, Takaya N, Cai J, Kliot M, Yuan C, Hatsukami TS. Images in cardiovascular medicine: detection of carotid atherosclerotic plaque ulceration, calcification, and thrombosis by multicontrast weighted magnetic resonance imaging. Circulation 2005;112:e3-4.

19. Saam T, Hatsukami TS, Takaya N, Chu B, Underhill H, Kerwin WS, Cai J, Ferguson MS, Yuan C. The vulnerable, or high-risk, atherosclerotic plaque: noninvasive MR imaging for characterization and assessment. Radiology 2007;244:64-77.

20. Takaya N, Yuan C, Chu B, Saam T, Underhill H, Cai J, Tran N, Polissar NL, Isaac C, Ferguson MS, Garden GA, Cramer SC, Maravilla KR, Hashimoto B, Hatsukami TS. Association between carotid plaque characteristics and subsequent ischemic cerebrovascular events: a prospective assessment with MRI--initial results. Stroke 2006;37:818-823.

21. Lusis AJ. Atherosclerosis. Nature 2000;407:233-241.

22. Glagov S, Weisenberg E, Zarins CK, Stankunavicius R, Kolettis GJ. Compensatory enlargement of human atherosclerotic coronary arteries. N. Engl. J. Med. 1987;316:1371-1375.

23. Fautz HP, Buchert M, Husstedt H, Laubenberger J, Hennig J. TSE sequences with spin echo contrast. Magn Reson Med 2000;43:577-582.

24. Rui L, Sun J, Ferguson MS, Yuan C. Quantitative measurements of MR constants in carotid plaque at 3T. In Program of the 22nd Annual International Conference on Magnetic Resonance Angiography, Seoul, Korea, 2010. p. 108.

25. Alexander AL, Buswell HR, Sun Y, Chapman BE, Tsuruda JS, Parker DL. Intracranial black-blood MR angiography with high-resolution 3D fast spin echo. Magn Reson Med 1998;40:298-310.

26. Fayad ZA, Fuster V, Fallon JT, Jayasundera T, Worthley SG, Helft G, Aguinaldo JG, Badimon JJ, Sharma SK. Noninvasive in vivo human coronary artery lumen and wall imaging using black-blood magnetic resonance imaging. Circulation 2000;102:506-510.

27. Yuan C, Tsuruda JS, Beach KN, Hayes CE, Ferguson MS, Alpers CE, Foo TK, Strandness DE. Techniques for high-resolution MR imaging of atherosclerotic plaque. J Magn Reson Imaging 1994;4:43-49.

28. Steinman DA, Rutt BK. On the nature and reduction of plaque-mimicking flow artifacts in black blood MRI of the carotid bifurcation. Magn Reson Med 1998;39:635-641.

29. Martin AJ, Gotlieb AI, Henkelman RM. High-resolution MR imaging of human arteries. J Magn Reson Imaging 1995;5:93-100.

30. Wang J, Yarnykh VL, Hatsukami T, Chu B, Balu N, Yuan C. Improved suppression of plaque-mimicking artifacts in black-blood carotid atherosclerosis imaging using a multislice motion-sensitized driven-equilibrium (MSDE) turbo spin-echo (TSE) sequence. Magn Reson Med 2007;58:973-981.

31. Kim S, Kholmovski EG, Jeong E, Buswell HR, Tsuruda JS, Parker DL. Triple contrast technique for black blood imaging with double inversion preparation. Magn Reson Med 2004;52:1379-1387.

32. Parker DL, Goodrich KC, Masiker M, Tsuruda JS, Katzman GL. Improved efficiency in double-inversion fast spin-echo imaging. Magn Reson Med 2002;47:1017-1021.

33. Lu H, Clingman C, Golay X, Zijl P. Determining the longitudinal relaxation time (T1) of blood at 3.0 Tesla. Magn Reson Med 2004;52:679-682.

34. Yarnykh VL, Yuan C. T1-insensitive flow supression using quadruple inversion-recovery. Magn Reson Med 2002;48:899-905.

35. Abragam A. The principles of nuclear magnetism: The International Series of Monographs on Physics.. Oxford: Clarendon Press; 1961. 599p.

36. Block W, Pauly J, Kerr A, Nishimura D. Consistent fat suppression with compensated spectral spatial pulses. Magn Reson Med 1997;38:198-206.

37. Higuchi N, Hiramatsu K, Mulkern RV. A novel method for fat suppression in RARE sequences. Magn Reson Med 1992;27:107-117.

CHAPTER 3

RIGID BODY MOTION CORRECTION WITH SELF NAVIGATION MRI[1]

The use of phase correlation to detect rigid-body translational motion is reviewed and applied to individual echo trains in turbo-spin-echo data acquisition. It is shown that when the same echo train is acquired twice, the subsampled correlation provides an array of delta-functions, from which the motion that occurred between the acquisitions of the two echo trains can be measured. It is shown further that a similar correlation can be found between two sets of equally spaced measurements that are adjacent in k-space. By measuring the motion between all adjacent pairs of k-space subgroups, the complete motion history of a subject can be determined and the motion artifacts in the image can be corrected. Some of the limiting factors in using this technique are investigated with turbo-spin-echo head and hand images.

3.1 Introduction

Turbo/fast spin echo (TSE/FSE) sequences (1-5) were developed initially to increase the efficiency of spin echo sequences by allowing many measurements (lines of k-space) to be acquired with a single excitation. These sequences are now widely used in clinical

---

[1]Reprinted with Permission from Magnetic Resonance in Medicine 2009:61:739-747

practice as one of the fast acquisition methods in Magnetic Resonance Imaging. Often these sequences are applied with multiple averages for each line of k-space to improve the image signal to noise ratio (SNR). Rather than sampling the same line of k-space multiple times, it is possible to obtain the same increase in SNR by increasing the field of view (FOV) in the phase encoding direction. This is equivalent to spacing the sampled lines of k-space more closely in the phase encoding direction.

Whether multiple averages or more finely spaced measurements are acquired, the increased SNR comes at a cost of increased imaging time, and a greater potential for subject motion during the acquisition. Usually, very little motion occurs during the short acquisition time of any one echo-train. The fact that only a single excitation is used for each echo-train also helps to reduce (although it cannot eliminate) the effects of motion during an echo-train.

Motion artifacts in a variety of MRI applications can be reduced using navigator echoes (6-16) to identify motion-corrupted measurements and either correct these measurements or reacquire them when the anatomy is close to the baseline position (17,18). Motion correction with navigators can come at the expense of a substantial increase in scan time. A more time efficient method is to extract information of in-plane and through-plane displacements from the navigator echoes so that k-space data can be retrospectively corrected (19-21). However, navigator displacement measurements require a priori knowledge of the type of motion so that the navigator can be tailored to the specific type of motion. For example, spherical (22) or orbital navigators (23) are often used to detect bulk translation and rotation. Pencil-beam navigators can be used to detect local translational motion (24). PROPELLER MRI (25) proposed by Pipe is a type

of self-navigated data acquisition technique, in which k-space data are acquired in blades to produce oversampling at the center of k-space. The oversampled k-space center acts as an inherent "navigator" to allow correction for in-plane bulk translation as well as rotation.

The potential of parallel imaging techniques for tackling motion problems has also been investigated (26). Bydder et al. (27) use SENSE (28) or SMASH (29) to regenerate fully sampled k-space data sets from subsampled copies of the original k-space and detect motion-corrupted phase encoding views from the difference between different sets of regenerated k-space data. The detected inconsistent views are discarded and replaced with synthesized data using generalized-SMASH reconstruction (30). This data regeneration method detects occasional motion (such as coughing and twitching). The data regeneration method does not require multiaverage scans, but the data must be from multiple coils. The method works well when motion is constrained to a small number of k-space lines and the lines are distributed throughout k-space. More extended motions would cause problems in both the detection and correction processes.

Another interesting motion correction technique was presented by Kadah, et al. (31). In this technique, a single line of k-space which is offset from k_y=0 (a floating navigator or FNAV), is acquired repeatedly during image acquisition. Motion in the readout direction is obtained by correlating the magnitudes of the Fourier transforms of subsequent FNAV's. Motion in the phase encoding direction is measured from the phase shift at the center of the FNAV. This technique was applied in the case of simulated experimental data. The technique can be applied to TSE sequences by using a single echo in the echo train to repeatedly sample the same line of k-space.

In this work we explore the possibility of self-navigation in a conventional TSE sequence using the correlation of adjacent sets of k-space lines. The method relies on the assumption that very little motion occurs during a single echotrain and that an extended FOV in the phase encoding direction has been acquired. Further, it requires that the phase encoding order of each echotrain be related by a simple shift in k-space. This technique could very easily supplement the technique of Kadah, et al.(31). In the following, we present the theory and justification of this technique. We present data on some of the limits of this technique and give an example of motion correction for TSE images of a head and hand.

3.2 Theory

3.2.1 Subsampled Cross Correlation

Rigid-body motion between two images m_1 and m_2 can be detected using the cross-correlation function:

$$c(x,y) = m_1(x,y) \otimes m_2^*(-x,-y) \qquad [3.1]$$

where $\otimes$ is the 2D convolution operator. This cross correlation can be written in the Fourier domain as:

$$C(k_x,k_y) = M_1(k_x,k_y)M_2^*(k_x,k_y) \qquad [3.2]$$

If m_2 is just a shifted version of m_1 (with offsets x_0 and y_0) then:

$$C(k_x,k_y) = \left|M_1(k_x,k_y)\right|^2 e^{i(k_x x_0 + k_y y_0)}. \qquad [3.3]$$

The offsets x_0 and y_0 can be measured from the phase of the correlation function in k-space. The transform of $C(k_x,k_y)$ is a Dirac delta function (offset from the origin by x_0 and y_0) convolved with the transform of the magnitude squared of $M_1(k_x,k_y)$.

$$c(x,y) = \delta(x - x_0, y - y_0) \otimes \Im\left(\left|M_1\right|^2\right) \quad [3.4]$$

where $\Im()$ is the 2D Fourier transform. Usually *c(x,y)* would be peaked at an offset showing the motion x_0 and y_0, however, $\Im(|M_1|^2)$ may actually blur or distort that position. The Dirac delta function is found more directly when $\Im(|M_1|^2)$ is removed from the correlation function as:

$$C_w(k_x,k_y) = e^{i\cdot\arg\left[C\left(k_x,k_y\right)\right]} = e^{i(k_x x_0 + k_y y_0)} \quad [3.5]$$

where arg() is the argument function that extracts the angular component of a complex number or function.

It can be shown that if $C_w(k_x,k_y)$ is computed from an incomplete set of regularly spaced k-space measurements (e.g. the same echo train sampled twice as in Fig. 3.1a), the resulting $c_w(x,y)$ will still show the original delta function, but will also show a set of aliased delta functions (Fig. 3.1b). Let $S_L(k_x,k_y)$ be the sampling function that selects the

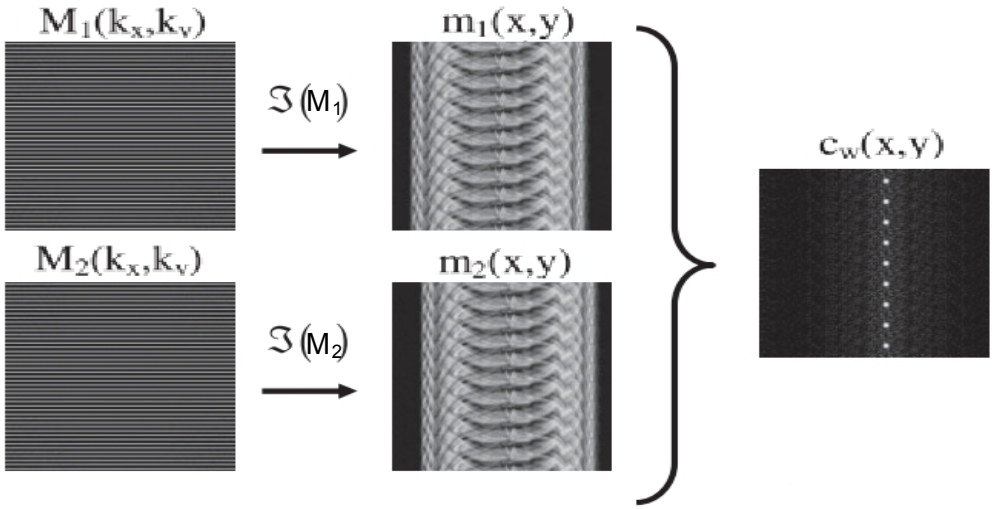

(a) (b)

Figure 3.1: Shown in (a) are repeated, subsampled acquisition of k-space (such as acquiring the same echo train twice) and the corresponding aliased images. The phase correlation, $c_w(x,y)$ shown in (b) is obtained from the cross correlation of the aliased images. The cross correlation shows the replicated delta functions offset from the zero-offset position.

k-space measurements for the L^{th} echotrain:

$$S_L(k_x,k_y)=\sum_{j=0}^{N_e-1}\delta\left(k_y-\left(L+jN_{et}\right)\Delta k_y\right) \qquad [3.6]$$

where N_e is the number of echoes in the echo train (or the echo train length) and N_{et} is the total number of echo trains used to acquire a full k-space. If the same echo train is sampled a second time after some time delay, the correlation between the two echo trains can be written as:

$$c_L(x,y)=\Im\left(S_L(k_x,k_y)\cdot C_w\left(k_x,k_y\right)\right)=\Im\left(S_L(k_x,k_y)\right)\otimes c_w\left(x,y\right). \qquad [3.7]$$

This correlation can be expressed in convolution integral as:

$$c_L(x,y)=\int_{-\infty}^{\infty}c_w(x,y-y')e^{\frac{i\pi y'}{N\Delta y}(2L-N+N_{et})}\frac{\sin(\pi y'/\Delta y)}{\sin(\pi y'/N_e\Delta y)}dy' \qquad [3.8]$$

where Δy is the spacing between voxels. After some algebra this becomes:

$$c_L(x,y)=\sum_{j=0}^{N_{et}-1}N_e e^{i\pi\left(\frac{2L}{N_{et}}+N_e-1\right)j}c_w(x,y-jN_e\Delta y). \qquad [3.9]$$

Thus, $c_w(x,y)$ is replicated with spacing $N_e\Delta y$ (the number of echoes in each echo train times the voxel spacing) with a phase that depends on the shift (L) of the k-space measurements. If the motion in the y-direction (y_L) occurring between two acquisitions of the same subset (L^{th} echo train acquired twice) is smaller than the aliasing distance:

$$y_L<\left|\frac{N_e\Delta y}{2}\right| \qquad [3.10]$$

then two repeated subsets (echo trains) rather than two samplings of full k-space can be used to detect the motion of the object.

3.2.2 Correlation of Adjacent Lines

In this work, we carry this observation one step further to show that it is possible to detect motion between two adjacent sets of k-space measurements. Suppose an image is reconstructed using equally spaced measurements from a single echo train with all other measurements set to zero. In that case a highly aliased version of the original image is obtained, as shown in Fig. 3.2a. Interestingly, a second image reconstructed from an adjacent set of equally spaced lines in k-space has some similarity to the first aliased image (Fig. 3.2b). If the object were to shift between acquisitions, one would expect that similar structures in both aliased images would also shift. In fact, one might naively assume that a cross-correlation of these two aliased images could be used to determine the shift. Unfortunately cross-correlation in image space corresponds to a multiplication in k-space. Since each echo train is a different set of k-space lines, the multiplication in k-space is identically zero and no information about motion between the two aliased images is available. Instead, consider what happens if we physically shift each k-space line in the first echo train by $\frac{1}{2}\Delta k_y$ and each line in the adjacent echo train by $-\frac{1}{2}\Delta k_y$. If a cross correlation is then taken, the correlation function described in Eq. [3.3] is modified as:

$$C(k_x, k_y + \tfrac{1}{2}) = \left|M_1(k_x, k_y)\right| \cdot \left|M_1(k_x, k_y + 1)\right| e^{i\phi_1(k_x,k_y) - i\phi_1(k_x,k_y+1)} e^{i(k_x x_L + (k_y+\frac{1}{2})y_L)} \qquad [3.11]$$

where the phase function $\phi_1(k_x,k_y)=\arg(M_1(k_x,k_y))$ is the phase of each k-space point in the absence of any motion. The weighted correlation function becomes:

$$C_w(k_x, k_y + \tfrac{1}{2}) = e^{i\cdot\arg\left[C(k_x,k_y+\frac{1}{2})\right]} = e^{i(k_x x_L + (k_y+\frac{1}{2})y_L) + i\phi_{Err}(k_x,k_y)} \qquad [3.12]$$

where $\phi_{Err}(k_x,k_y)= \phi_1(k_x,k_y)-\phi_1(k_x,k_y+1)$ is the phase error term and is caused by the fact

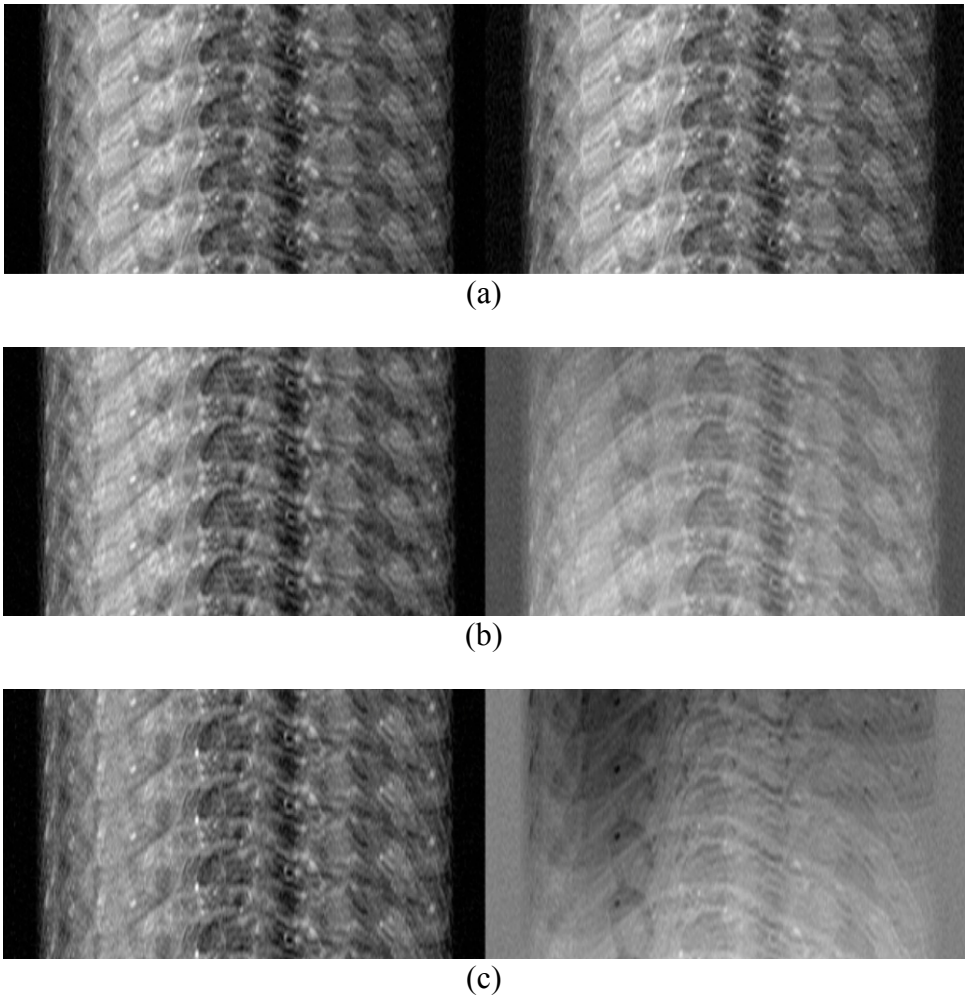

(a)

(b)

(c)

Figure 3.2: 2D TSE hand images reconstructed from a single echo train (N_e=17 and N_{et}=31). The images correspond to 3 adjacent sets of equally spaced k-space lines from the (a) 15_{th}, (b) 16_{th} and (c) 17_{th} echo trains. The left side is the magnitude image and the right side is the real image. The real image shows the slow variation in phase caused by the shift in the k-space sampling pattern.

that adjacent k-space lines are not perfectly correlated.

If an object fills less than the measured field of view in the phase encoding direction (i.e., an extended FOV is acquired), then it can be shown that there is at least some correlation between adjacent measurements in k-space. An object having a finite region of support is equivalent to multiplication by a rectangular window in image space, or convolution with a sinc-function in k-space. The width of the sinc-function in k-space is

inversely related to the width of the image support. Therefore, as the measured FOV increases and the sinc-function broadens, the correlation between adjacent k-space lines increases and the phase error term is reduced. In practice we will use a finite FOV and so there will always be some residual phase error. The transform of the correlation function will still contain a delta function offset from the origin by x_L and y_L but will now be convolved with an error term due to $\phi_{Err}(k_x,k_y)$.

$$c_w(x,y) = \delta(x - x_l, y - y_l) \otimes \Im\left(e^{i\phi_{Err}}\right) \qquad [3.13]$$

Any linear component of the phase error term will cause a shift in the delta function and will directly affect the accuracy of the motion estimates. The higher order terms of the phase error tend to blur and distort the delta function making it difficult to accurately locate the delta peak.

To the extent that the phase error term is small, it is then possible to detect the motion between adjacent groups of lines of k-space. By using this technique to measure the incremental motion between every pair of adjacent echo trains, the complete motion history during a scan can be obtained. The absolute position of the object at the time of each echo train is obtained by adding the shifts:

$$x_{Shift}(t) = \sum_{L=1}^{t} x_L \qquad [3.14]$$

and the same for the y direction. This motion history can then be used to correct a TSE MRI acquisition for nonrotational rigid-body motion. Motion correction is accomplished by applying the appropriate linear phase shift for each echo train. It is shown in the following sections that a reasonable FOV can be selected such that the phase error is small enough to produce motion corrected images.

3.3 Methods

Ten data sets of 2D TSE head images were obtained on a Siemens Trio 3T MRI scanner from a volunteer using a single channel head coil. Each data set was acquired at a different FOV but imaging parameters were selected to keep resolution, SNR and contrast as constant as possible across all data sets (Table 3.1). Five slice locations were acquired in each data set. Each image has a resolution of 0.5mm x 0.5mm x 2mm, TR=3s, TE=13ms and 11 echoes per echo train.

Motion artifacts were introduced by applying varying linear phase shifts to each echo train taking into account the slice interleaving and phase encoding order used to acquire the images. The amount of motion between two successive echo trains was randomly selected with the maximum value constrained to satisfy Eq. [3.10]. For the rotation experiments, the object was rotated (post acquisition) back and forth by a fixed value between each echo train.

To test the algorithm in conjunction with actual motion, 11 high resolution 2D

Table 3.1: Imaging parameters[a] used to acquire 2D TSE head images

Samples	FOV	% FOV (PE Direction)	BW/Pixel
418x418	209 mm^2	105	130
462x462	231 mm^2	116	144
506x506	253 mm^2	126	157
550x550	275 mm^2	138	172
594x594	297 mm^2	149	183
638x638	319 mm^2	160	196
682x682	341 mm^2	171	209
726x726	363 mm^2	182	222
770x770	385 mm^2	193	241
814x814	407 mm^2	204	256

[a]Parameters were selected to hold the resolution, SNR and contrast constant while allowing for a variable FOV in the phase encoding direction. Five interleaved slices were acquired with a 0.5mm x 0.5mm x 2mm resolution, ETL=11, TR=3s and TE=13ms.

TSE images of a human hand were acquired on a Siemens Trio 3T MRI scanner using a single channel wrist coil. The images were acquired with a TR/TE = 4000/60 ms, ETL (N_e) = 17 and 31 echo trains (N_{et}). The acquisition FOV = 120mm, slice thickness = 3mm, N_{aqx} = 640, N_{aqy} = 527, giving a spatial resolution of 0.1875 mm and 0.2277 mm in the x and y respectively. The hand filled about 1/3 of the imaged FOV. During the acquisition, the subject moved his hand occasionally.

All human studies were approved by the institutional review board and informed consent was obtained from the volunteers.

3.4 Results

The motion detected for the TSE head images with a FOV twice the object size is shown in Fig. 3.3. The solid line in Fig. 3.3a and 3.3b shows the actual motion applied to the head images and the dots represent the motion calculated using the self navigating technique proposed in this work. It has been assumed that the typical motion of an object will follow some relatively smooth time course. This smooth time course was accomplished by multiplying the Fourier transform of the detected objects motion in time by a low pass filter. The error between this band-limited curve and the actual motion is shown in Fig. 3.3c. For this TSE data set, the maximum error is less than 0.4 mm in either direction.

The images obtained from these motion estimates are shown in Fig. 3.4. Each of the five columns represent one of the five acquired slice locations. Fig 3.4c shows the corrected images when no band-limited curve is fit to the data (i.e. motion represented by the dots in Fig. 3.3a and 3.3b). Although the images offer a significant improvement over the motion corrupted images (Fig 3.4b) there is still some unwanted motion artifact.

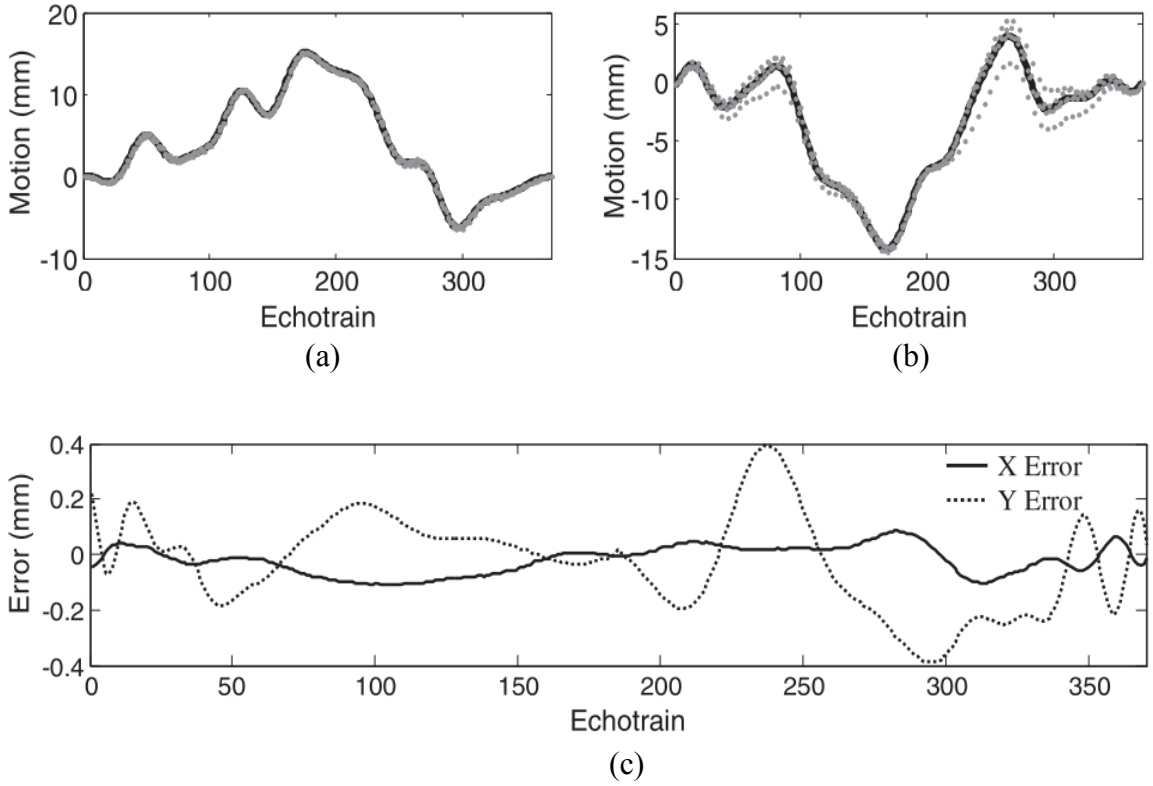

Figure 3.3: Simulated motion tracking on TSE head images with a FOV double the object size, five interleaved slices with a 0.5mm x 0.5mm x 2mm resolution, ETL=11, TR=3s and TE=13ms. The top graphs show motion detection in the (a) readout or x direction and (b) phase encode or y direction. The grey dots represent the motion calculated using self navigation and the solid line is the actual motion. The Fourier Transform of the calculated data is multiplied by a low pass filter to produce a smoothed line for the objects motion. A smoothed line is then fit to the calculated data and compared to the actual motion in (c). The solid line is the error in the x (readout) direction while the dashed line is error in the y (phase encode) direction.

This residual artifact is reduced when the motion is constrained to be band-limited (Fig. 3.4d).

The effect of varying the FOV on motion artifact reduction is demonstrated in Fig. 3.5. When the FOV approaches the size of the object, the self navigating technique is not able to fully correct the motion artifacts (Fig. 3.5a). However, if we acquire a FOV of 126% the object size (Fig. 3.5c), many of the motion artifacts are eliminated. With a larger FOV of 171% the object size almost all the motion artifacts have been removed.

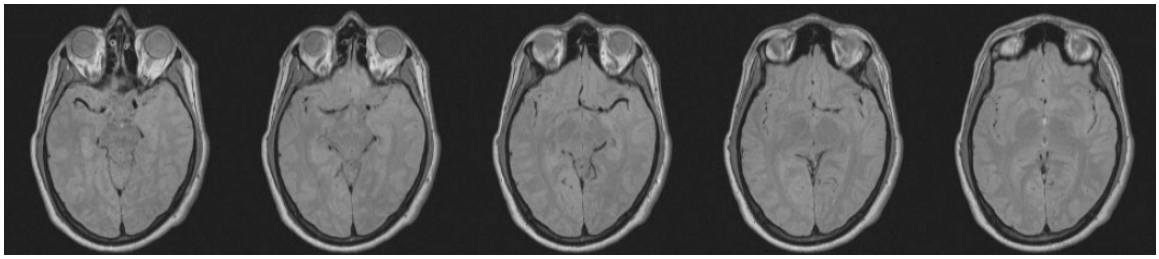

(a)

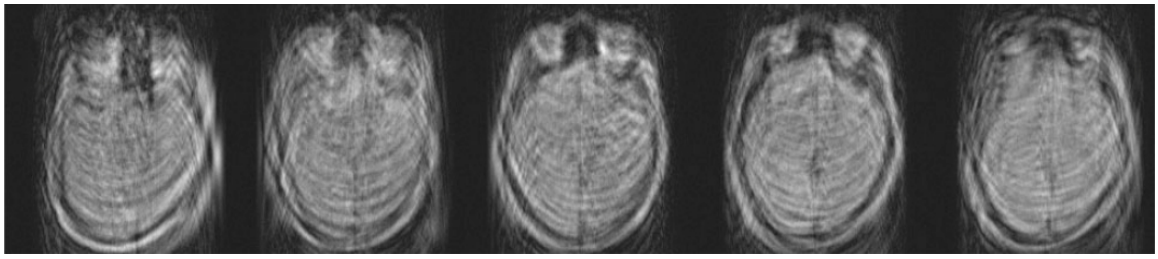

(b)

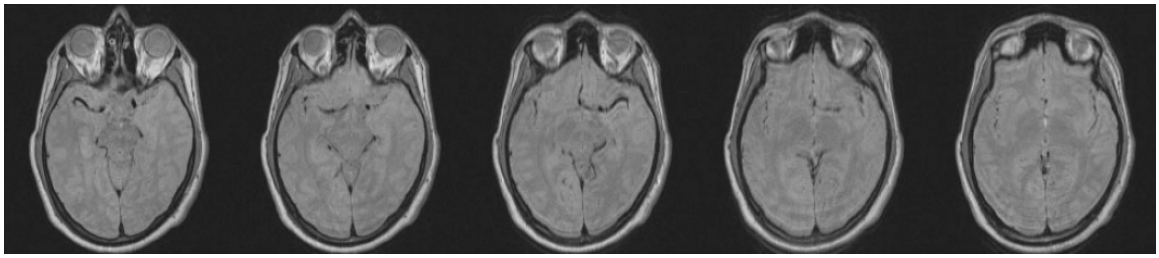

(c)

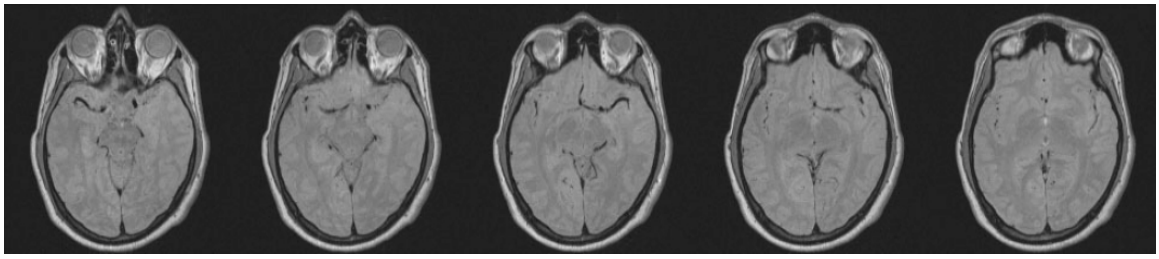

(d)

Figure 3.4: TSE head images acquired with the parameters in Table 3.1 and the motion correction shown in Figure 3.3. Each vertical column represents a different slice location. The images without motion artifacts are shown in (a), the motion corrupted images in (b), images corrected individually in (c) and with constrained motion using all five slices in (d).

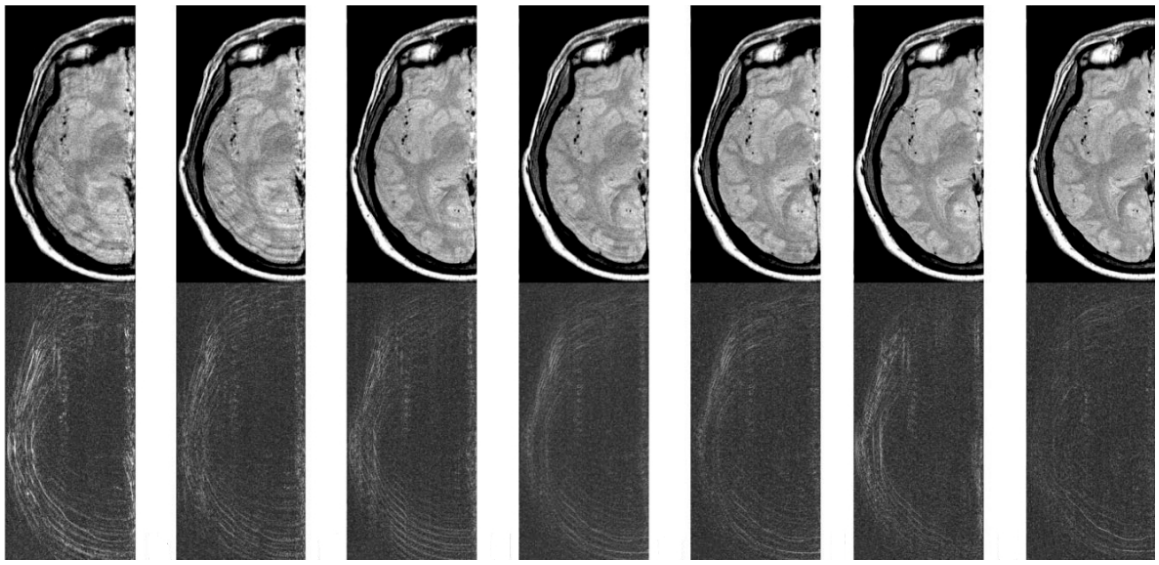

(a) (b) (c) (d) (e) (f) (g)

Figure 3.5: TSE motion corrected head images with varying FOV. The top row contains images corrected using the proposed self navigating technique and the bottom row shows the difference images (compared to the original motion free image). Each column represents a different FOV with (a) 105%, (b) 116%, (c) 126%, (d) 138%, (e) 149%, (f) 160% and (g) 171% of the objects region of support.

This is supported when one looks at the coefficient of variation of the motion corrected images compared with the original motion free images as shown in Fig. 3.7. Images obtained at a FOV of 126% have a coefficient of variation which is half the value for images obtained at a FOV of 100% the object size. For data sets with a FOV larger than 171% (the object size) the improvement continues but at a slower rate.

The ability to accurately detect motion with minor rotations is shown in Fig. 3.6 and 3.7. The goal is not to correct for the rotation artifacts, but simply to show that the motion artifacts themselves can be corrected in the presence of small rotations. For both the 126% and 171% FOV data sets, it is shown that if the rotation of the object is less than two degrees between successive echo trains in a slice, the motion correction is still successful (Fig. 3.6.). Even when the rotation is two degrees between each echo train in a

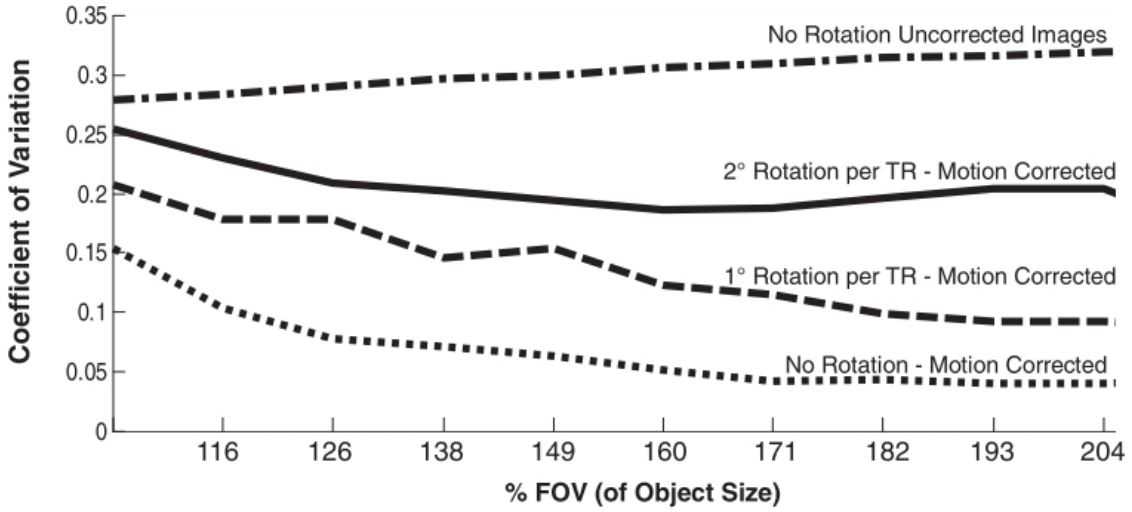

Figure 3.6: Coefficient of variation with the original motion free images for varying FOV. The dot-dashed line compares the uncorrected images, the solid line represents corrected images with a 2° degree rotation between echo trains, the dashed line is corrected images with a 1° rotation between echo trains and the dotted line is corrected images with no object rotation during acquisition.

slice, there is still a reduction to the motion artifacts using the self navigation technique, just to a lesser extent (Fig. 3.7).

An image of the hand with occasional motion during the acquisition is shown in Fig. 3.8a. The aliased images reconstructed from echo-trains 15, 16, and 17 out of 31 are shown in Fig. 3.2. For comparison, the image after correction using the technique of this work is shown in Fig. 3.8b. Nine of the 11 slices of the acquisition contained signal and similar results were observed in each of these. Because the slices are acquired in an interleaved fashion, one would expect the measured shift in each image to follow some relatively smooth time course. In Fig. 3.9, the thick line plots the shift in the "y" direction for the nine slices in chronological order. It can be seen that the shifts are relatively smooth, as expected, and show nine movements in the negative direction. Also plotted in Fig. 3.9 is the corresponding shift in the "x" direction (thin line).

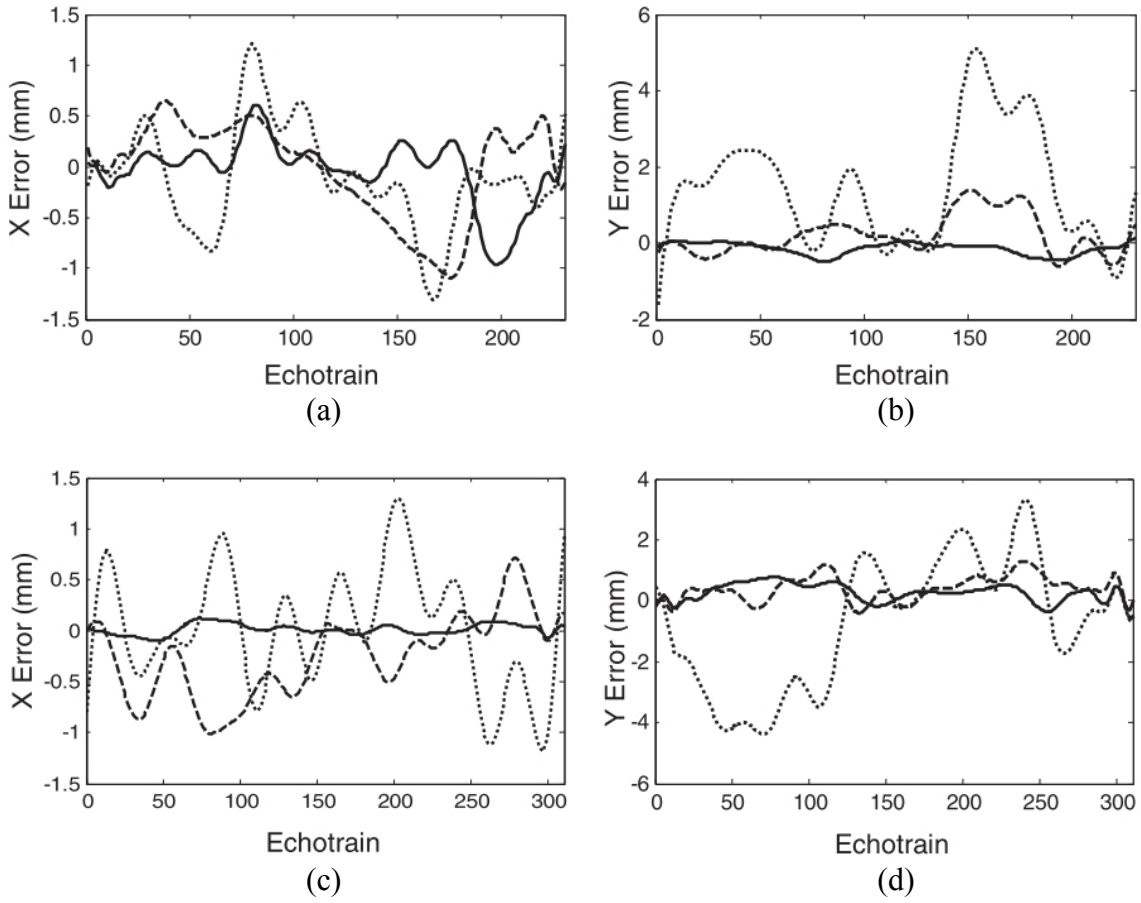

Figure 3.7: Error in motion correction using the proposed self navigation technique in the presence of small object rotations. The top row shows the (a) X motion error and (b) Y motion error when the FOV is 126% the object size. The bottom row shows the (c) X motion error and (d) Y motion error when the FOV is 171% the object size. The solid lines represent no object rotation, the dashed line is a 1° rotation between any two adjacent data sets and the dotted line is a 2° rotation between any two adjacent data sets.

3.5 Discussion

It has been demonstrated that MRI data can be self-navigating under the circumstances that subsets of k-space measurements are acquired closely enough in time to limit motion and rotation between successive acquisitions and that a FOV be selected such that adjacent subsets of measurements have an adequate amount of correlation. The technique differs with the technique presented by Kadah, et al. (31) where floating

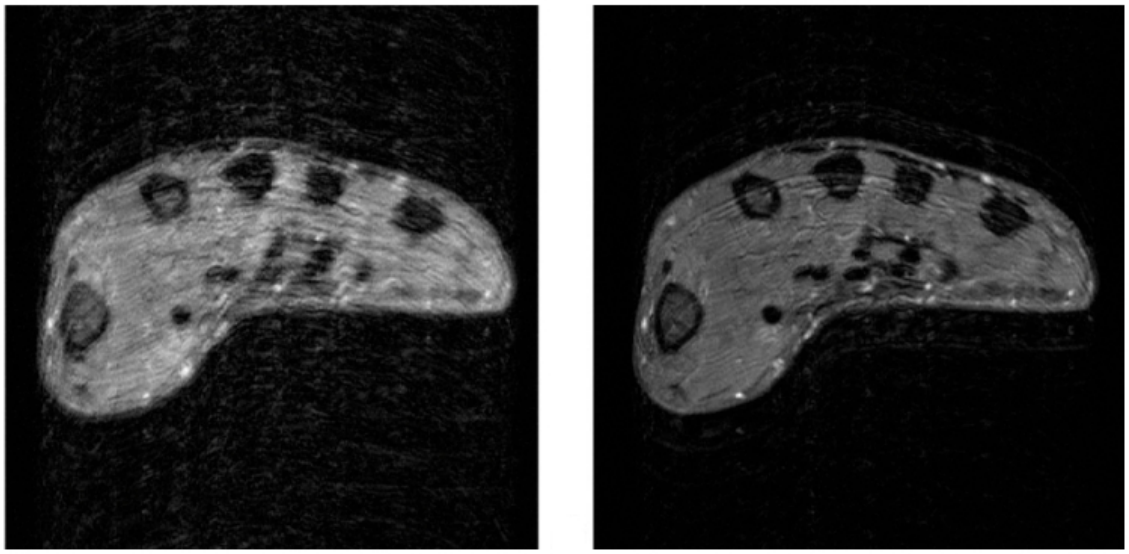

(a) (b)

Figure 3.8: A single axial slice from a 22-slice T2w TSE images of the hand. Motion that occurred during acquisition caused severe blurring and some ghosting in (a). An image obtained from the same measurement data of the same slice using the correction method described in this work is shown in (b).

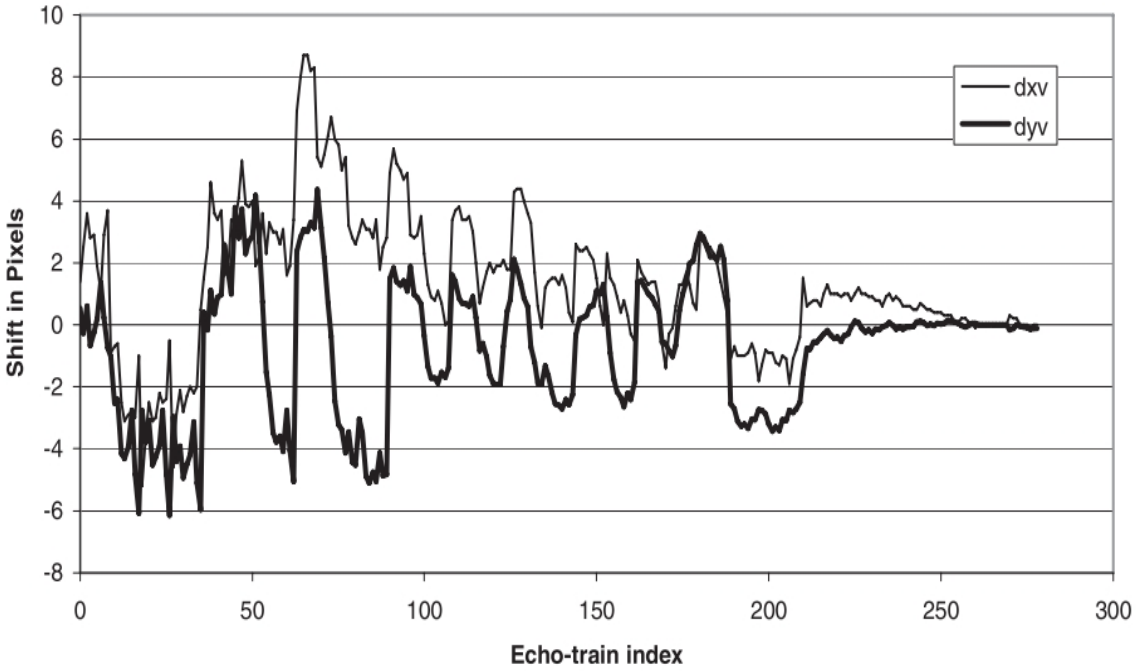

Figure 3.9: A plot of the x and y offsets in chronological order for 9 of the 11 interleaved slices where the SNR was strong enough for the correlation technique to be applied.

navigators encode motion in the phase encoding direction with one navigator at one k-space offset position. That offset position is a compromise to maintain a high enough SNR while avoiding aliasing in the measurement of any motion. On the other hand, this self navigator technique spreads the measurements across k-space allowing a small window in which the motion can be uniquely determined. The technique of Kadah, et al. also has a small window in which the phase can be determined uniquely:

$$\varphi = \frac{\varphi_o \pm 2n\pi}{2\pi k_f} \qquad [3.15]$$

where k_f is the FNAV frequency offset from 0 and n is a positive integer.

Although it has been shown that self-navigation can be applied successfully, a few questions remain as to the limitations of the technique. First, the effect of the echo train length has not been fully studied. We note that this method applies nicely to T2w TSE data where an echo train length of at least 11 was used. However, the technique can also apply to acquisition orders with shorter echo-trains if motion between adjacent and/or sequential echo trains is very small. Shorter echo trains would be generally used for T1 weighted studies. Additionally, if motion is minimal between two sequentially acquired echo trains, it is possible to acquire the data from both trains such that when combined they form one set of equally spaced lines in k-space. Self-navigation can then be applied by testing for motion between sets of combined echo trains that are adjacent in k-space. Thus, one combined echo train may be correlated with an adjacent combined echo train. Second, the effects of surface coils are not known. For example, when using an array of surface coils, the image support for each coil will be defined by the coil sensitivity, reducing the requirement for phase encoding oversampling.

Finally, self-navigation could work for nonuniform sampling of k-space and rather

than finding the delta-function location in image space, it would be possible to fit the phase surface with an inclined plane.

We note that this technique should work also for segmented EPI, GRASE pulse sequences, and any sequence where the order of acquisition allows minimal motion within the set, but the probability of motion is great between sets. It should be possible to configure the acquisition of most gradient echo sequences such that equally spaced sets of k-space are acquired in temporal proximity such that motion between the set of lines is minimal, and motion between adjacent sets can be detected by correlation.

Although we did not discuss correcting rotations, there are at least two extensions of this method that could allow small rotations to be detected and corrected. First, we have performed experiments showing that the correlation in the phase encoding direction can be performed as a function of position in the readout direction. The slope of the correlation as a function of "x" indicates the magnitude of rotation. Experiments to verify this observation are ongoing. Second, the use of arrays of surface coils provides many opportunities for spatial localized sensitivities for individual coil measurements. The distribution of translations observed for each local coil can then be combined to provide an estimate of the translation and rotation of the rigid body. It is entirely possible that these local coil motion measurements may allow non-rigid-body motions to be estimated and ultimately corrected.

3.6 Conclusion

This work provides a demonstration that rigid-body translational motion that occurs during the acquisition of MRI data can be detected, quantified and corrected using self navigation when subsets of k-space measurements are acquired closely spaced in time

such that motion occurs between subsets, and that there is sufficient support external to the object in the acquisition space that adjacent subsets of measurements are correlated.

3.7 Acknowledgments

This work has been supported by NIH grants HL48223 and HL57990, as well as grants from the Cumming Foundation, the Ben B. and Iris M. Margolis Foundation, and the Mark H. Huntsman Endowed Chair.

3.8 References

1. Hennig J, Nauerth A, Friedburg H. RARE imaging: a fast imaging method for clinical MR. Magn Reson Med 1986;3(6):823-833.

2. Mulkern RV, Wong ST, Winalski C, Jolesz FA. Contrast manipulation and artifact assessment of 2D and 3D RARE sequences. Magn Reson Imaging 1990;8(5):557-566.

3. Constable RT, Anderson AW, Zhong J, Gore JC. Factors influencing contrast in fast spin-echo MR imaging. Magn Reson Imaging 1992;10(4):497-511.

4. Constable RT, Gore JC. The loss of small objects in variable TE imaging: implications for FSE, RARE, and EPI. Magn Reson Med 1992;28(1):9-24.

5. Le Roux P, Hinks RS. Stabilization of echo amplitudes in FSE sequences. Magn Reson Med 1993;30(2):183-190.

6. Ehman RL, Felmlee JP. Adaptive technique for high-definition MR imaging of moving structures. Radiology 1989;173(1):255-263.

7. Butts K, de Crespigny A, Pauly JM, Moseley M. Diffusion-weighted interleaved echo-planar imaging with a pair of orthogonal navigator echoes. Magn Reson Med 1996;35(5):763-770.

8. Danias PG, McConnell MV, Khasgiwala VC, Chuang ML, Edelman RR, Manning WJ. Prospective navigator correction of image position for coronary MR angiography. Radiology 1997;203(3):733-736.

9. de Crespigny AJ, Marks MP, Enzmann DR, Moseley ME. Navigated diffusion imaging of normal and ischemic human brain. Magn Reson Med 1995;33(5):720-728.

10. Hu X, Kim SG. Reduction of signal fluctuation in functional MRI using navigator echoes. Magn Reson Med 1994;31(5):495-503.

11. Kyriakos WE, Panych LP, Zientara GP, Jolesz FA. Implementation of a reduced field-of-view method for dynamic MR imaging using navigator echoes. J Magn Reson Imaging 1997;7(2):376-381.

12. McConnell MV, Khasgiwala VC, Savord BJ, Chen MH, Chuang ML, Edelman RR, Manning WJ. Prospective adaptive navigator correction for breath-hold MR coronary angiography. Magn Reson Med 1997;37(1):148-152.

13. Taylor AM, Jhooti P, Wiesmann F, Keegan J, Firmin DN, Pennell DJ. MR navigator-echo monitoring of temporal changes in diaphragm position: implications for MR coronary angiography. J Magn Reson Imaging 1997;7(4):629-636.

14. Tyszka JM, Silverman JM. Navigated single-voxel proton spectroscopy of the human liver. Magn Reson Med 1998;39(1):1-5.

15. Wang Y, Rossman PJ, Grimm RC, Riederer SJ, Ehman RL. Navigator-echo-based real-time respiratory gating and triggering for reduction of respiration effects in three-dimensional coronary MR angiography. Radiology 1996;198(1):55-60.

16. Wirestam R, Salford LG, Thomsen C, Brockstedt S, Persson BR, Stahlberg F. Quantification of low-velocity motion using a navigator-echo supported MR velocity-mapping technique: application to intracranial dynamics in volunteers and patients with brain tumors. Magnetic resonance imaging 1997;15(1):1-11.

17. Sachs TS, Meyer CH, Irarrazabal P, Hu BS, Nishimura DG, Macovski A. The diminishing variance algorithm for real-time reduction of motion artifacts in MRI. Magn Reson Med 1995;34(3):412-422.

18. Crowe L, Keegan J, Gatehouse P, Mohiaddhin R, Varghese A, Symmonds K, Cannell T, Yang GZ, Firmin D. Improvement of 3D volume selective turbo spin echo imaging for carotid artery wall imaging with navigator detection of swallowing. J Cardiovasc Magn Reson 2005;7(1):203-205.

19. Anderson AW, Gore JC. Analysis and correction of motion artifacts in diffusion weighted imaging. Magn Reson Med 1994;32(3):379-387.

20. Ordidge RJ, Helpern JA, Qing ZX, Knight RA, Nagesh V. Correction of motional artifacts in diffusion-weighted MR images using navigator echoes. Magn Reson Imaging 1994;12(3):455-460.

21. Wang Y, Ehman RL. Retrospective adaptive motion correction for navigator-gated 3D coronary MR angiography. J Magn Reson Imaging 2000;11(2):208-214.

22. Welch EB, Manduca A, Grimm RC, Ward HA, Jack CR, Jr. Spherical navigator echoes for full 3D rigid body motion measurement in MRI. Magn Reson Med 2002;47(1):32-41.

23. Fu ZW, Wang Y, Grimm RC, Rossman PJ, Felmlee JP, Riederer SJ, Ehman RL. Orbital navigator echoes for motion measurements in magnetic resonance imaging. Magn Reson Med 1995;34(5):746-753.

24. Li D, Kaushikkar S, Haacke EM, Woodard PK, Dhawale PJ, Kroeker RM, Laub G, Kuginuki Y, Gutierrez FR. Coronary arteries: three-dimensional MR imaging with retrospective respiratory gating. Radiology 1996;201(3):857-863.

25. Pipe JG. Motion correction with PROPELLER MRI: application to head motion and free-breathing cardiac imaging. Magn Reson Med 1999;42(5):963-969.

26. Larkman DJ, Atkinson D, Hajnal JV. Artifact reduction using parallel imaging methods. Top Magn Reson Imaging 2004;15(4):267-275.

27. Bydder M, Larkman DJ, Hajnal JV. Detection and elimination of motion artifacts by regeneration of k-space. Magn Reson Med 2002;47(4):677-686.

28. Pruessmann KP, Weiger M, Scheidegger MB, Boesiger P. SENSE: sensitivity encoding for fast MRI. Magn Reson Med 1999;42(5):952-962.

29. Sodickson DK, Manning WJ. Simultaneous acquisition of spatial harmonics (SMASH): fast imaging with radiofrequency coil arrays. Magn Reson Med 1997;38(4):591-603.

30. Bydder M, Larkman DJ, Hajnal JV. Generalized SMASH imaging. Magn Reson Med 2002;47(1):160-170.

31. Kadah YM, Abaza AA, Fahmy AS, Youssef AB, Heberlein K, Hu XP. Floating navigator echo (FNAV) for in-plane 2D translational motion estimation. Magn Reson Med 2004;51(2):403-407.

CHAPTER 4

ROTATION CORRECTION WITH SELF NAVIGATED MRI

This work provides a demonstration that in-plane rotational motion that occurs during the acquisition of MRI data can be quantified using a self-navigation technique. The proposed technique compares adjacent sets of measurement lines in k-space to detect and quantify object rotation. This method can be applied to any segmented sequence that samples k-space in sets of equally spaced lines. It does not require any patient preparation or the acquisition of separate navigator data. Additionally, the technique can be applied to the data postacquisition. The method does require a slightly increased FOV in the phase encoding direction but the increase is small enough that resolution or total scan time are not significantly affected. By measuring the rotation between all pairs of adjacent sets of lines in k-space the entire rotation history of an object can be determined. The success of the technique is demonstrated with head and phantom turbo-spin-echo images.

4.1 Introduction

Turbo/Fast spin echo (TSE/FSE) sequences (1-6) are now widely used in clinical applications as fast acquisition methods in Magnetic Resonance Imaging. TSE sequences measure multiple lines of k-space with a single excitation. Since k-space is acquired over

time in a segmented fashion, object motion must be considered in the image reconstruction. Typically, most of the object motion does not occur during the acquisition window, but instead occurs during the longer TR interval. We can therefore combine all in-plane rotations and translations that occur during a TR interval into a single rotation about the origin followed by a translation. It is not the purpose of this study to investigate the detection of object translation and only sufficient attention will be given to this topic as required. We will instead focus on the detection of in-plane rotation for a two dimensional object.

One method of measuring rotation is to use the projection width of an object (7). This method requires restrictive assumptions about the object shape and has limited success. Externally placed spatial-frequency tuned markers can be applied to track and reduce rotation artifacts but require patient preparation (8). Orbital navigators utilize a circular k-space trajectory to detect object rotation (9). Spherical navigators sample a spherical k-space shell to allow for motion correction in multiple directions (10, 11). PROPELLER is a type of self-navigated data acquisition technique in which k-space data are acquired in blades to produce oversampling at the center of k-space (12). The oversampled k-space center acts as an inherent navigator to allow correction for in-plane rotation. The use of moments of spatial projections in radial MRI has also been proposed for a method of motion correction (13).

In this work we explore a self-navigating technique that correlates adjacent sets of k-space lines to correct in-plane object rotations. The technique can be applied to any segmented sequence that acquires sets of equally spaced lines. The only requirement is that the field of view (FOV) be slightly larger than the object in the phase encoding

direction. In many instances the normally prescribed FOV is already slightly larger than the objects extent and no modifications are required. This technique can be applied to the data post acquisition and could be used to supplement many other translation detection and correction techniques. In this study we present the theory and experimental evidence of the success of self-navigated rotation correction. The detection of object rotation is demonstrated with 2D TSE head and phantom images.

4.2 Theory

Consider a continuous object described by a function $m_1(x,y)$ and Fourier transform $M_1(k_x,k_y)$. If $m_2(x,y)$ is a rotated version of $m_1(x,y)$ by angle θ, the Fourier transform of the rotated object is then:

$$M_2(k_x,k_y) = M_1(k_x \cos\theta - k_y \sin\theta, k_y \cos\theta + k_x \sin\theta). \quad [4.1]$$

One simple method to find the rotation between the objects is to counter rotate $M_2(k_x,k_y)$ by some test angle ϕ and compare it to $M_1(k_x,k_y)$ using the following weighted difference:

$$\Delta M(\phi) = \iint \left| \frac{|M_{2\phi}(k_x,k_y)| - |M_1(k_x,k_y)|}{|M_{2\phi}(k_x,k_y)| + |M_1(k_x,k_y)| + \varepsilon} \right| \cdot dk_x dk_y \quad [4.2]$$

where,

$$M_{2\phi}(k_x,k_y) = M_2(k_x \cos\phi + k_y \sin\phi, k_y \cos\phi - k_x \sin\phi) \quad [4.3]$$

is the counter rotated $M_2(k_x,k_y)$ and ε is some small constant to prevent a division by zero. Taking the absolute values of $M_1(k_x,k_y)$ and $M_{2\phi}(k_x,k_y)$ allows the detection of object rotation to be independent of any object translation. If the rotated object is not angularly symmetric, then the weighted difference function in Eq. [4.2] will exhibit a

minimum value when the test angle ϕ equals the object rotation θ.

The measurements made in MRI are, in general, discrete samples of the Fourier transform of the desired image. Consider a TSE sequence that subsamples k-space with each echo train by a set of equally spaced lines. The discrete k-space data sampled by the L^{th} echo train can be written:

$$M_L(n,m) = \sum_{j'=0}^{N-1} \sum_{j=0}^{N_e-1} M(n\Delta k_x, m\Delta k_y)\delta(m - L - jN_{et})\delta(n - j') \qquad [4.4]$$

where N is the number of samples in the k_x direction, N_e is the number of echoes in the echo train (or the echo train length) and N_{et} is the total number of echo trains used to acquire a full k-space. To find the amount of object rotation between two acquisitions of the same echo train, $M_{L1}(n,m)$ and $M_{L2}(n,m)$, we proceed in much the same way as the continuous case. We first counter rotate $M_{L2}(n,m)$ by a test angle ϕ and then re-grid the data to form $M_{L2\phi}(n,m)$. The data from the two echo trains are then compared with a weighted difference formula similar to Eq. [4.2]. However, in this case we only want to compare k-space points that contain information from both echo trains (whether the data is correlated or not). Figure 4.1 shows the acquisition of two identical echo trains with one of the data sets rotated. Only the data points located at the dots (Fig. 4.1c) contain

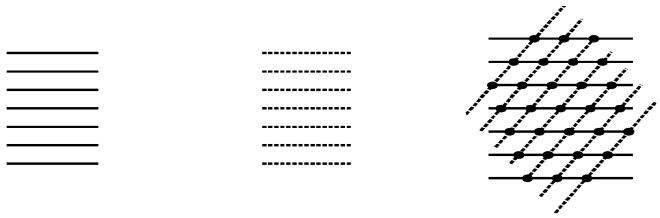

(a) (b) (c)

Figure 4.1: K-space trajectories of the same echo train acquired twice (a-b). The combined k-space trajectories (after the dotted lines are rotated by 45°) are shown in (c). The dots represent the points that contain information from both echo trains and should be included in the weighted difference formula.

information from both echo trains. To accomplish this selection task we define a weighting function *W(n,m)*, which is a set of delta functions, that zeros any data points that do not contain information from both echo trains. The weighted difference formula is then:

$$\Delta M_L(\phi) = \frac{1}{N_W} \sum_n \sum_m \left| \frac{|M_{L2\phi}(n,m)| - |M_{L1}(n,m)|}{|M_{L2\phi}(n,m)| + |M_{L1}(n,m)| + \varepsilon} \cdot W(n,m) \right| \qquad [4.5]$$

where

$$N_W = \sum_n \sum_m W(n,m) \qquad [4.6]$$

is the total number of points compared by the weighted difference function. If we then step through a range of test values for ϕ with the desired angular resolution, the rotation of the object can be found from the minimum of the weighted difference function in Eq. [4.6].

In this study we will go one step further to show that it is possible to detect rotation between two adjacent sets of k-space measurements as:

$$\Delta M_L(\phi) = \frac{1}{N_W} \sum_n \sum_m \left| \frac{|M_{(L+1)\phi}(n,m)| - |M_L(n,m)|}{|M_{(L+1)\phi}(n,m)| + |M_L(n,m)| + \varepsilon} \cdot W(n,m) \right|. \qquad [4.7]$$

However, when the test angle ϕ is too small for adjacent lines to overlap, then the weighted difference function given by Eq. [4.7] is always zero. To overcome this problem we make use of the fact that adjacent lines of k-space may contain correlated information. If an object fills less than the measured field of view in the phase encoding direction (i.e. an extended FOV is acquired), then it can be shown that there is at least some correlation between adjacent measurements in k-space. Another way to think of this is that an object having a finite region of support is equivalent to multiplication by a

rectangular window in image space, or convolution with a sinc-function in k-space. The width of the sinc-function in k-space is inversely related to the width of the image support. Therefore, as the measured FOV increases and the sinc-function broadens, the correlation between adjacent k-space lines increases. We therefore introduce a convolution function that allows us to not only compare points that exactly overlap, but also those points that are simply near each other in the phase encoding direction. The modified weighted difference formula then becomes:

$$\Delta M_L(\phi) = \frac{1}{N_W} \sum_n \sum_m \left| \frac{\left|M_{(L+1)2\phi}(n,m) \otimes C(m)\right| - \left|M_{L1}(n,m)\right|}{\left|M_{(L+1)2\phi}(n,m) \otimes C(m)\right| + \left|M_{L1}(n,m)\right| + \varepsilon} \cdot W(n,m) \right| \qquad [4.8]$$

where $\otimes_m$ is the one dimensional convolution operator in the direction of the variable *m* and *C(m)* is the convolution function. In this work the following 1x3 convolution function was used:

$$C(m) = [1 \quad 1 \quad 1]. \qquad [4.9]$$

This convolution function essentially states that we want the weighted difference to include correlations between samples that are up to one pixel away from each other. Using this technique to measure the incremental rotation between every pair of adjacent echo trains, the complete rotation history during a scan can be obtained. The absolute angle of the object at the time of each echo train is obtained by adding the incremental rotations:

$$\theta(t) = \sum_{L=1}^{t} \phi_L \qquad [4.10]$$

where ϕ_L is the test angle that minimized the weighted difference function $\Delta M_L(\phi)$. The original data can then be corrected for this rotation using a method such as the one

proposed by Atkinson and Hill (14). Finally the translation of the object can be found by making use of the linear phase difference between correlated points of the two sets of lines. We have shown in another study that the phase of adjacent sets of lines in k-space can be used to detect object translation (15).

4.3 Methods

Ten data sets of 2D TSE axial head images were obtained on a Siemens Trio 3T MRI scanner from a volunteer using a single channel head coil. Each data set was acquired at a different FOV but imaging parameters were selected to keep resolution, SNR and contrast as constant as possible across all data sets (Table 4.1). Five different slice locations were acquired in each data set. Each image has a resolution of 0.5mm x 0.5mm x 2mm, TR=3s, TE=13ms and 11 echoes per echo train. Rotation artifacts were introduced to each echo train post acquisition taking into account the slice interleaving and phase encoding order used to acquire the images.

Additionally, 2D TSE axial images of an American College of Radiology (ACR)

Table 4.1: Imaging parameters[a] used to acquire 2D TSE head images

Samples	FOV	% FOV (PE Direction)	BW/Pixel
418x418	209 mm^2	105	130
462x462	231 mm^2	116	144
506x506	253 mm^2	126	157
550x550	275 mm^2	138	172
594x594	297 mm^2	149	183
638x638	319 mm^2	160	196
682x682	341 mm^2	171	209
726x726	363 mm^2	182	222
770x770	385 mm^2	193	241
814x814	407 mm^2	204	256

[a]Parameters were selected to hold the resolution, SNR and contrast constant while allowing for a variable FOV in the phase encoding direction. Five interleaved slices were acquired with a 0.5mm x 0.5mm x 2mm resolution, ETL=11, TR=3s and TE=13ms.

MRI phantom were acquired. The ACR phantom contains a solution of nickel chloride and sodium chloride: 10 mM NiCl2 and 75 mM NaCl. The phantom has an inside diameter of 190 mm. The images had a TR/TE of 2000/13 ms and an echo train length of 16. The FOV was 224mm with 448x448 samples being collected, giving a resolution of 0.5mmx0.5mmx5mm. Several data sets were collected with the ACR phantom physically rotated by varying amounts.

All human studies were approved by the institutional review board and informed consent was obtained from the volunteers.

4.4 Results

It is first demonstrated that one can detect an object rotation between two acquisitions of the same echo train. The first echo train acquired from the object in Fig. 4.2a is compared to the first echo train of the same object rotated 4.6 degrees (Fig. 4.2b). The weighted difference in Fig. 4.2c shows a definite minimum located at 4.6 degrees. To

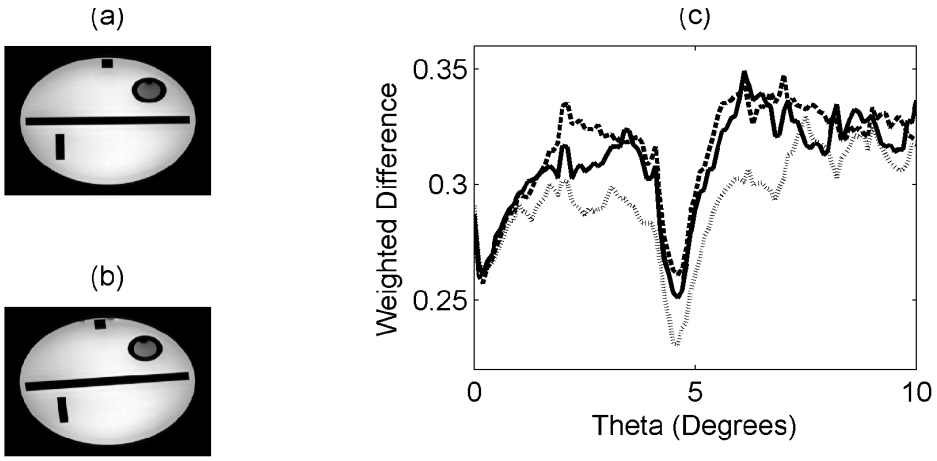

Figure 4.2: Weighted difference between two acquisitions of the same echo train (c). One of the echo trains is from the object in (a) and is compared to the same echo train from the same object rotated by 4.6° (b). The solid (L=1), dashed (L=2) and dotted (L=3) lines represent different subsets of k-space being acquired by the echo trains according to Eq. [4.4].

help show consistency, the experiment is repeated to compare the second echo train from each image and again comparing the third echo trains. The weighted difference functions from each identically show a minimum at the expected 4.6 degrees.

The results are then extended to show that object rotation can be detected between two adjacent echo trains. Figure 4.3 shows the comparison of adjacent echo trains from an object rotated by 4.6 degrees. The first echo train, acquired from the object in Fig. 4.3a, is compared to the second echo train of the same object rotated 4.6 degrees (Fig. 4.3b). Although the minimum is not as pronounced as for the case of the same echo train (Fig. 4.2c), it still has a minimum located at 4.6 degrees. The experiment is repeated comparing the second and third echo trains followed by the third and fourth echo trains with similar results. For the remainder of this study only adjacent data sets will be considered in detecting object rotations.

For a FOV the same size as the object, Figure 4.4 shows the average absolute error of the detected rotation angle. As the object rotation approaches zero there is a greater error

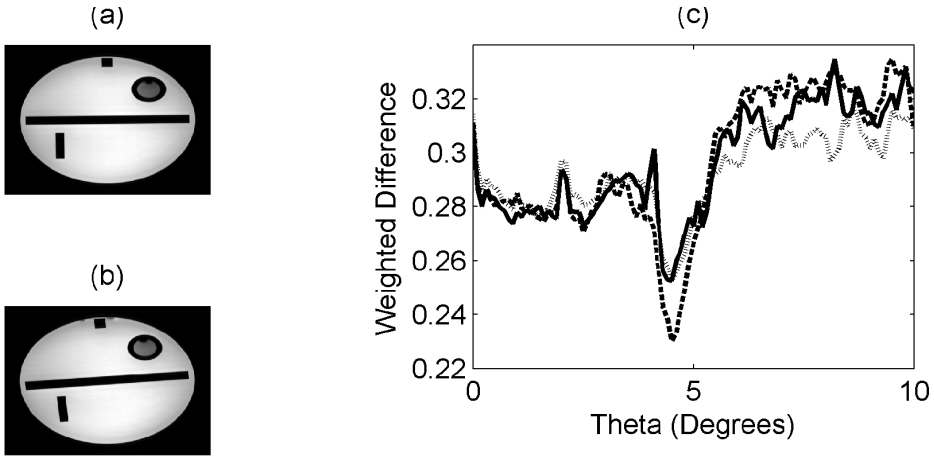

Figure 4.3: Weighted difference between two adjacent echo trains (c). One of the echo trains is from the object in (a) and is compared to the adjacent echo train from the same object rotated by 4.6° (b). The solid line compares the 1st and 2nd echo trains, the dashed line compares the 2nd and 3rd echo trains and the dotted line compares the 3rd and 4th.

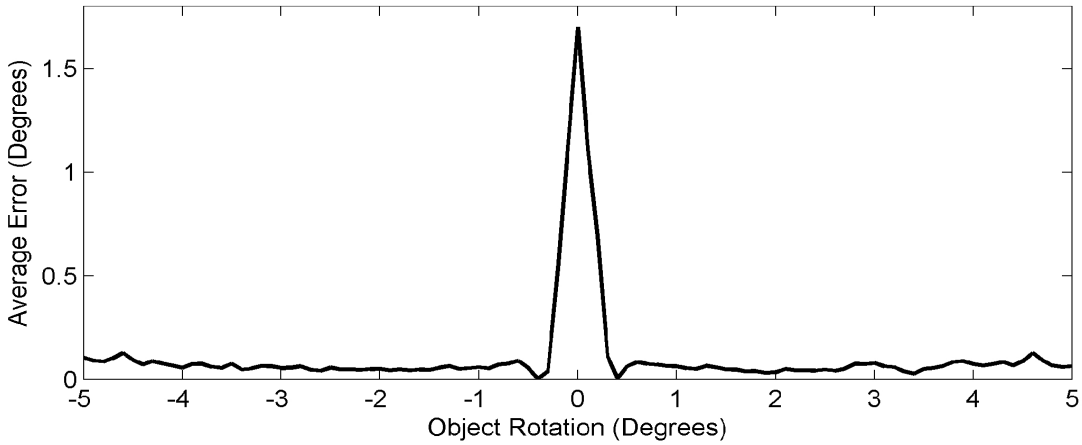

Figure 4.4: Average error in the detected angle for all sets of adjacent lines in a data set. An object was rotated by a constant angle (shown on the x-axis) between each echo train and the proposed self navigating technique was applied to detect the rotation. The error in the detected angle is about 0.1 degrees until the object rotation becomes close to zero.

in detecting the rotation angle. This error can be reduced by increasing the FOV, however, increasing the FOV is not desirable because it increases scan time or decreases resolution. The error in the detected angle for small object rotations can also be corrected with a smaller range of test angles. In Figure 4.4 the range of test angles was held constant (±10° in 0.1° intervals). For small rotation angles this large range often leads to errors in distinguishing the minimum caused by the object rotation (Fig. 4.5a). However, if we consider a reduced range of test angles then the correct minimum can be found and the rotation angle correctly quantified (Fig. 4.5b).

The results of applying the proposed self-navigating rotation correction are shown in Figures 4.6 and 4.7. Adjacent sets were correlated with a FOV of 105% the object size. Figure 4.6a shows the actual object motion with the gray solid line and the calculated rotation is indicated with the black dots. The bottom graph (Fig. 4.6b) shows the difference between the actual and detected rotation. Figure 4.7 shows the original image and the difference images without (Fig. 4.7b) and with correction (Fig. 4.7c). The

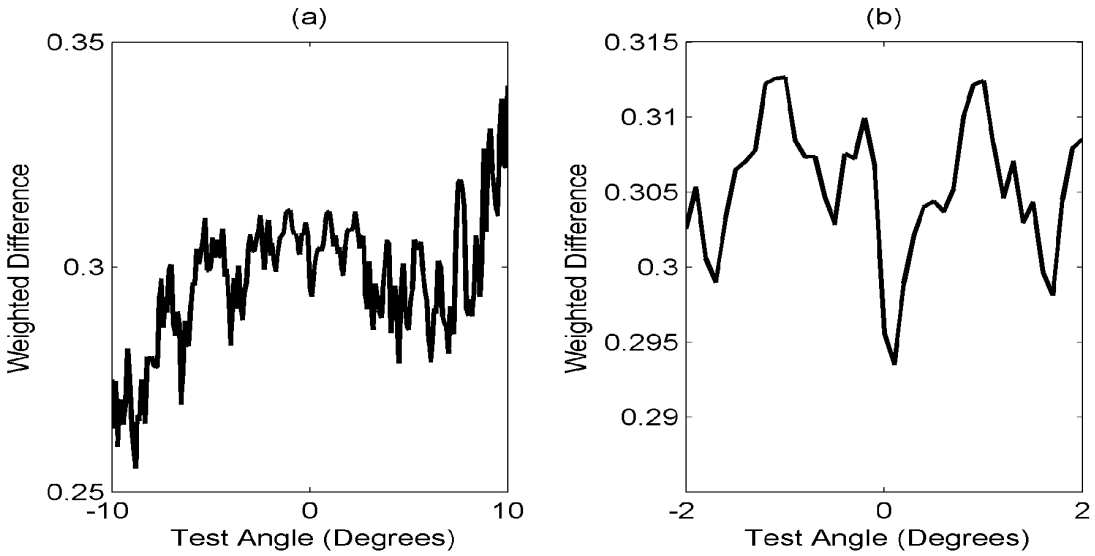

Figure 4.5: Weighted difference function comparing adjacent echotrains for a small angle of rotation of the object (0.1 degrees). When a large range of test values are evaluated (a), the minimum is incorrectly given at –8.8 degrees. However, a local minimum gives the correct rotation of 0.1 degrees when a limited range of angles in considered (b).

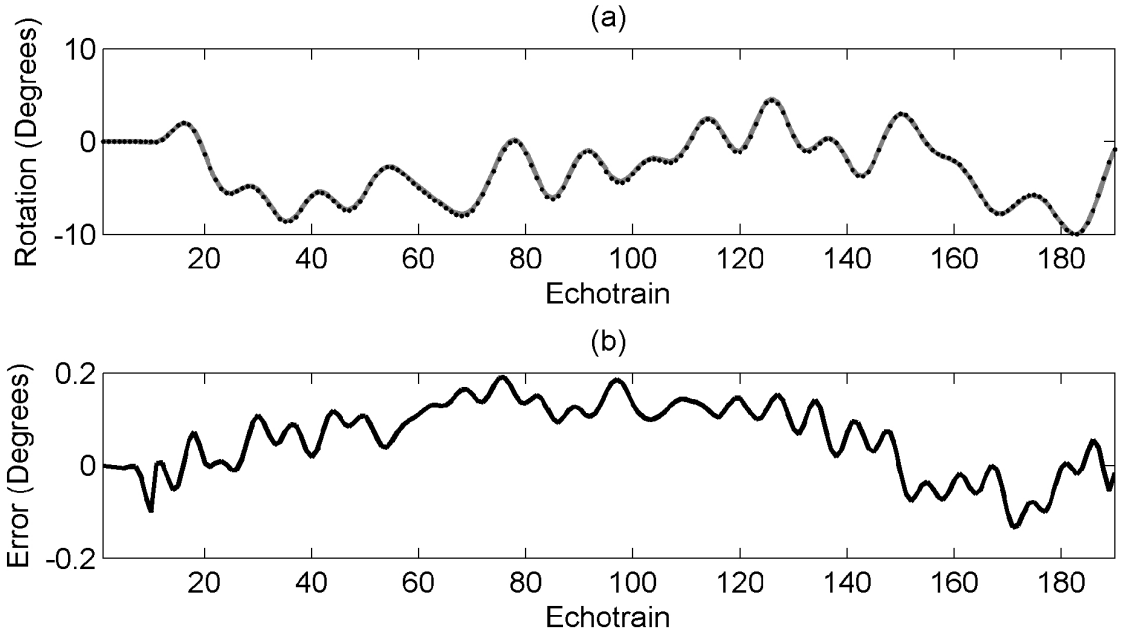

Figure 4.6: Graph of the actual and detected object rotation (a) and the difference between the two (b). The solid gray line in the top graph is the actual object rotation during the acquisition of five interleaved slices. The black dots in the top graph are the detected rotation angles using the proposed self-navigating technique.

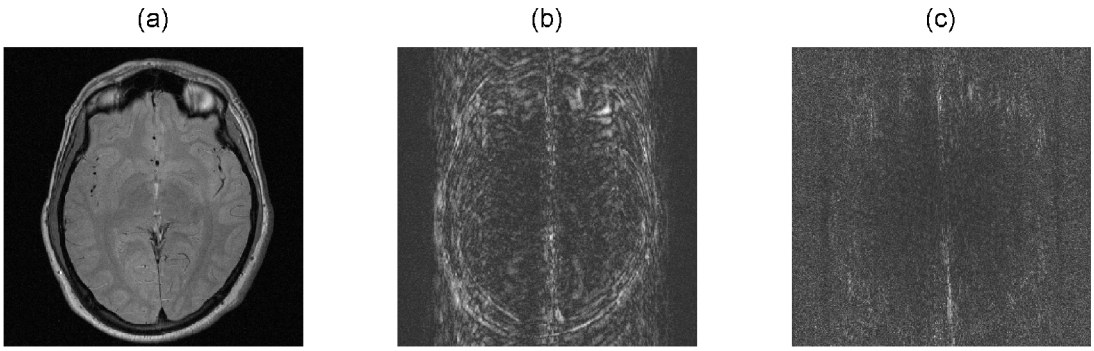

Figure 4.7: The original artifact free image is shown in (a). The difference image comparing the rotation corrupted and the original image is shown in (b). The difference image comparing the original image and the corrected image using the proposed self-navigating rotation correction is shown in (c). The rotation angles of the object and the detected rotation angles are shown in Fig. 4.6.

difference image comparing the corrected image to the original shows that most of the remaining artifact has a similar intensity to that of the surrounding noise.

4.5 Discussion

For most of this study we have focused on detecting object rotation by correlating adjacent sets of lines in a segmented sequence. While the proposed technique works more easily when comparing the same set of lines, it also requires twice as much data to be acquired. The feasibility of this technique comes from the fact that it can be applied to data acquired by segmented sequences already widely used and available on most MRI scanners and that it does not require a significant increase in scan time.

The proposed self-navigated rotation correction procedure can be described by the following steps. For each set of adjacent lines the weighted difference function is calculated with some set range of test angles. The range of test angles should be chosen large enough to cover the expected rotation but small enough to optimize reconstruction time. The minimum of the weighted difference function is used to calculate the objects

rotation. Also, a measure of confidence in the detected angle is taken using two different criteria. First, the number and magnitude of neighboring local minima in the weighted difference function is considered. For small object rotations when the detection error is greatest, there are typically multiple local minima over the test range with similar magnitudes to the minimum point of interest. Second, for small object rotations, when there is an error in the angle it is typically very large. That is, the minimum value of the weighted difference tends to occur at extreme values of the tested angle range. This can cause large jumps or discontinuities when looking at the rotation history of the object. Since the time between interleaved echo trains is kept at a minimum, we expect to be able to track rotation in a somewhat smooth fashion. The detected rotation angles are therefore compared with the detected angle from the previous and the next time frames. A large discontinuity is often due to an incorrectly detected angle. Taking into account these two criteria the algorithm then detects which points are likely to be incorrect. The algorithm then redetects the rotation angle for these points using a smaller range of test angles and knowledge of the object rotation in surrounding time frames. The process can be iterated if desired to continue to refine the detected rotation angles. Typically only two or three iterations are required to converge on a solution. Once the rotation history of the object is known the data can correctly placed in k-space. Then we must apply some sort of translation correction technique to completely quantify and correct the rigid-body motion of the object.

Although we do require a larger FOV it needs to be only slightly larger in the phase encode direction. The studies shown here of 2D TSE head images produced adequate results with a FOV of just 105% the object size (which was the smallest FOV

investigated). Often the normally prescribed FOV is already not fit tightly around the object and consequently no increase in the FOV will be required. Continuing to increase the FOV will increase the accuracy of the results and possibly decrease the number of iterations required, but the increased number of samples ultimately leads to a longer scan and reconstruction time. As a result, most cases will justify the use of a FOV only slightly larger than the object size.

The convolution function chosen in Eq. [4.9] essentially states that we want the weighted difference to include correlations between samples that are up to one pixel away from each other. Some preliminary work has shown that weighting those contributions according to the distance between correlated samples only marginally improves the results.

As the rotation of the object between echo trains increases, it is also possible to relax the requirement that we compare adjacent data sets. For large rotation angles, even a nonadjacent echo train will contribute points to the weighted difference formula (Fig. 4.8). As a result, it is possible to compare the echo train containing rotated data to several other echo trains rather than just a single one. This generates more accurate results but requires a way of determining when the object rotation is large enough to warrant such a variation.

4.6 Conclusion

This work provides a demonstration that in-plane rotational motion that occurs during the acquisition of MRI data can be quantified using a self-navigation technique. The proposed technique compares adjacent sets of measurement lines in k-space to detect and quantify object rotation. This method can be applied to any segmented sequence that

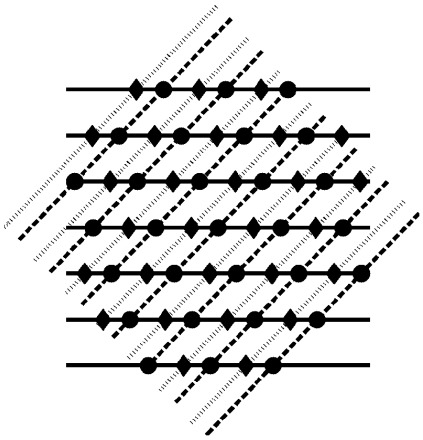

Figure 4.8: K-space trajectories of a selected echo train (solid lines) compared to an adjacent echo train (dashed lines) and a non-adjacent echo train (dotted lines). The circles represent points used in the weighted difference for the adjacent echo train and the diamonds are the points used for the non-adjacent echo train.

samples k-space in sets of equally spaced lines. It does not require any patient preparation or the acquisition of separate navigator data. The method only requires a slight increase in the field of view along the phase encoding direction, but the amount of increase required is small enough that resolution or total scan time are not significantly affected. By measuring the rotation between all pairs of adjacent sets of lines in k-space the entire rotation history of an object can be determined.

4.7 Acknowledgments

This work has been supported by NIH grants HL48223 and HL57990, as well as grants from the Cumming Foundation, the Ben B. and Iris M. Margolis Foundation, and the Mark H. Huntsman

4.8 References

1. Hennig J, Nauerth A, Friedburg H. RARE imaging: a fast imaging method for clinical MR. Magn Reson Med 1986;3(6):823-833.

2. Mulkern RV, Wong ST, Winalski C, Jolesz FA. Contrast manipulation and artifact assessment of 2D and 3D RARE sequences. Magn Reson Imaging 1990;8(5):557-566.

3. Constable RT, Anderson AW, Zhong J, Gore JC. Factors influencing contrast in fast spin-echo MR imaging. Magn Reson Imaging 1992;10:497-511.

4. Constable RT, Gore JC. The loss of small objects in variable TE imaging: implications for FSE, RARE, and EPI. Magn Reson Med 1992;28:9-24.

5. Le Roux P, Hinks RS. Stabilization of echo amplitudes in FSE sequences. Magn Reson Med 1993;30:183-190.

6. V. Rasche, D Holz, W Scheppeer. Radial turbo spin echo imaging. Magn Reson Med 1994;32:629-638.

7. Wood ML, Stanchev PL, Shivji MJ. Correction for planar rigid-body movements during MRI. J Magn Reson Imaging 1994;4(P):62.

8. Korin HW, Felmlee JP, Riederer SJ, Ehman RL. Spatial-frequency-tuned markers and adaptive correction for rotational motion. Magn Reson Med 1995;33:663-669.

9. Fu ZW, Wang Y, Grimm RC, Rossman PJ, Felmlee JP, Riederer SJ, Ehman RL. Orbital navigator echoes for motion measurements in magnetic resonance imaging. Magn Reson Med 1995;34:746-753.

10. Welch EB, Manduca A, Grimm RC, Ward HA, Jack CR. Spherical navigator Echoes for full 3D rigid body motion measurments in MRI. Magn Reson Med 2002;47:32-41.

11. Costa AF, Petrie DW, Yen YF, Drangova M. Using the axis of rotation of polar navigator echoes to rapidly measure 3D rigid-body motion. Magn Reson Med 2005;53:150-158.

12. Pipe JG. Motion correction with PROPELLER MRI: application to head motion and free-breathing cardiac imaging. Magn Reson Med 1999;42:963-969.

13. Welch EB, Rossman PJ, Felmlee JP, Manduca A. Self-navigated correction using moments of spatial projections in radial MRI. 2004;52:337-345.

14. Atkinson D, Hill DLG. Reconstruction after rotational motion. Magn Reson Med 2003;49:183-187.

15. Mendes JK, Kholmovski E, Parker DL. Rigid body motion correction with self navigation MRI. Magn Reson Med 2009;61:739-747.

CHAPTER 5

INTRINSIC DETECTION OF MOTION IN SEGMENTED SEQUENCES[1]

While many motion correction techniques for MRI have been proposed, their use is often limited by increased patient preparation, decreased patient comfort, additional scan time or the use of specialized sequences not available on many commercial scanners. For this reason we propose a simple self-navigating technique designed to detect motion in segmented sequences. We demonstrate that comparing two segments containing adjacent sets of k-space lines results in an aliased error function. A global shift of the aliased error function indicates the presence of in-plane rigid-body translation while other types of motion are evident in the dispersion or breadth of the error function. Since segmented sequences commonly acquire data in sets of adjacent k-space lines, this method provides these sequences with an inherent method of detecting object motion. Motion corrupted data can be reacquired proactively or in some cases corrected or removed retrospectively.

5.1 Introduction

Patient motion is one of the dominant sources of artifact in MRI. Techniques developed to detect and correct motion include those that utilize specialized hardware to

---

[1]Reprinted with Permission from Magnetic Resonance in Medicine (In Press)

detect patient motion, those that utilize special k-space trajectories with some inherent motion correction ability, those that acquire additional navigator data for the purpose of motion correction and those considered to be self-navigating.

Motion detection techniques that rely on specialized hardware include reflecting laser beams off specialized markers (1), optical tracking with one or more cameras (2-5), tracking using small receiver coils (6-8), infrared tracking systems (9, 10) and using spatial-frequency tuned markers(11).

Techniques that use specialized trajectories for motion correction include acquiring rotated sets of overlapping parallel lines (12), interleaving spiral trajectories (13, 14), acquiring data in some sort of hybrid Radial-Cartesian fashion (15-17) or using alternating frequency/phase encode directions (18-20).

Other techniques acquire additional navigator data as a Cartesian projection in the absence of either phase or frequency encoding (21) or with a floating navigator (22, 23). Orbital navigators utilize a circular k-space trajectory to detect object motion (24) while spherical navigators sample spherical k-space shells (25, 26). When multiple receive coils are used the complementary data can be used to detect and replace motion corrupted data (27). In particular, spatial harmonics in SMASH reconstruction (28) can be utilized to compare newly measured data with predictions calculated from previously sampled data (29). Alternatively, a SENSE based reconstruction (30) can be used to replace motion detected from low resolution images (31). While all these techniques have shown success in their respective applications, their use is often limited by one or more of the following: increased complexity in patient preparation, decreased patient comfort, additional scan time or the required use of specialized sequences not available on many

commercial scanners. For this reason there has always been marked interest in the category of motion detection with self-navigation.

Several proposed self-navigating techniques address a specific type of motion (typically in-plane and rigid-body) but none seem to address both rigid and nonrigid body motion that can occur both in and out of plane. For example, motion in the readout direction has been detected by taking the Fourier Transform of a line of acquired data and trying to determine the edges of the object's profile (32, 33). The edges become increasingly difficult to determine from lines encoded near the edges of k-space and high contrast markers are often added to the patient to overcome this problem. Motion in the phase encode direction can be detected using a symmetric density constraint along the phase encoding axis (33). However, the algorithm is restrictive on the object type and may not perform well for large motion in the phase encode direction (34). Another approach is to apply a spatial constraint to the object and then use an iterative phase retrieval algorithm to calculate the desired phase of the object (35). The calculated phase is compared to the measured phase to simultaneously find motion in the readout and phase encode directions. The algorithm performs well for subpixel motions but is unable to correct an artifact caused by large translations (34). Combinations of these self navigating methods have also been proposed to overcome some of their pitfalls (34, 36). Motion may also be determined by iteratively minimizing the entropy of motion induced ghosts and blurring in an otherwise dark region of an image (37, 38). Alternatively, data correlations between adjacent data lines can provide information about in-plane rigid body translation(39, 40). Radial sequences can provide a self-navigating method for rigid-body motion correction using moments of spatial projections (41) or the phase

properties of radial trajectories (42). Motion correction in the slice direction has also been explored by monitoring amplitude modulations of the acquired data (43, 44). A combination of some of these proposed techniques can be utilized to fully correct in-plane rigid-body motion but does not include the ability to address other types of motion. It may not be possible to correct out-of-plane motion or motion that is not rigid-body, but it is necessary and may be sufficient to at least be able to detect which data lines are corrupt.

The focus of this work is the detection of data that is corrupted by out-of-plane or non-rigid body motion. The proposed technique was designed and implemented in a carotid imaging application; however, the principles are easily adapted to other imaging applications.

5.2 Theory

Two adjacent (closely spaced) points in k-space will typically show some degree of correlation. This correlation will occur when the object being imaged does not fill the entire FOV or when the object's signal intensity is modified by the receive coil's sensitivity profile. In the latter case, the k-space data are convolved with the Fourier transform of the receive coil's sensitivity profile which introduces correlations between data points.

These data correlations can be exploited with a proposed self-navigating technique to detect various types of object motion. Consider an image acquisition that is divided into N_{Seg} segments that each sample a set of equally spaced k-space lines with a sampling function:

$$S_L\left(k_x,k_y\right)=\sum_{j=0}^{N_{Line}-1}\delta\left(k_y-\left(L+jN_{Seg}\right)\Delta k_y\right) \qquad [5.1]$$

where L is the current segment, N_{Line} is the number of lines sampled per segment and Δk_y is the distance between adjacent phase encode lines in the fully sampled k-space. The number of lines per segment is kept small enough that the object can be assumed to be approximately stationary during the acquisition of a single segment. Now consider the correlation of two adjacent data segments. Since each segment samples a different set of k-space lines, to compare the L^{th} and the $(L+1)^{th}$ segments, the k-space data of the $(L+1)^{\text{th}}$ segment is shifted by Δk_y. A weighted cross correlation is then taken as:

$$C_L\left(k_x,k_y,t\right)=\frac{F_L\left(k_x,k_y,t\right)F_{L+1}^{*}\left(k_x,k_y+\Delta k_y,t+\Delta t\right)}{\left|F_L\left(k_x,k_y,t\right)\right|\cdot\left|F_{L+1}\left(k_x,k_y+\Delta k_y,t+\Delta t\right)\right|} \qquad [5.2]$$

where $F_L(k_x,k_y,t)$ is the Fourier transform of the object's image weighted by the sampling function $S_L(k_x,k_y)$ given in Eq. [5.1]. The phase of the weighted cross correlation function is separated into a linear term, representing rigid-body translation (40), and a non-linear term for motion not classified as rigid-body translation. The cross correlation function with the new phase separation is:

$$C_L\left(k_x,k_y,t\right)=e^{i\left[k_x dx(t)+k_y dy(t)\right]}e^{i\varphi\left(k_x,k_y,t\right)}S_L\left(k_x,k_y\right) \qquad [5.3]$$

where $\varphi(k_x,k_y,t)$ is the nonlinear portion of the phase and $dx(t)$ and $dy(t)$ quantify the rigid-body translation between the acquisition at time t and the acquisition at $t+\Delta t$. If an error function is defined as:

$$\varepsilon\left(x,y,t\right)=\Im\left[e^{i\varphi\left(k_x,k_y,t\right)}\right] \qquad [5.4]$$

then the weighted cross correlation in image space is similar to the previously published result (40), except it is modified by the error function as:

$$c_L(x,y,t) = N_{Line} \sum_{j=0}^{N_{Seg}-1} e^{i\pi\left(\frac{2L}{N_{Seg}}+N_{Line}-1\right)j} \varepsilon\left[x - dx(t), y - dy(t) - jN_{Line}\Delta y, t\right] \quad [5.5]$$

where Δy is the image space voxel size in the phase encoding direction. The basic result is an aliased set of error functions defined by Eq. [5.4] that are collectively shifted proportionally to the object's rigid-body translation. The error function $\varepsilon(x,y,t)$ is a measure of data correlation between the L^{th} and $(L+1)^{th}$ data segments. If there are enough echoes in the echo train, the aliased copies of $\varepsilon(x,y,t)$ will be spaced far enough apart for one to characterize the general shape of the error function (40). Our main postulate is that object motion can be correlated with the error function dispersion (a measure of how peaked or spread out the error function is).

5.3 Methods

All data sets were obtained on a Siemens Trio 3T MRI scanner. Human studies were approved by the institutional review board and informed consent was obtained from the volunteers.

TSE 2D axial neck images were obtained from two volunteers using a two element surface coil (one anterior and one posterior coil) and a third volunteer using a four element surface coil (45). Data from the first volunteer were acquired with 252x256 pixels, a resolution of 0.8mm x 0.8mm x 5mm, TR=1.5s, TE=6.8ms and seven echoes per echo train. Data from the second volunteer were acquired with 512x512 pixels, a resolution of 0.35mm x 0.35mm x 5mm, TR=1.5s, TE=8.6ms and 16 echoes per echo train.

For the third volunteer, reacquiring data prospectively was simulated by acquiring two complete data averages; the first data average is acquired with volunteer motion

while the second data average is acquired with no motion. Once the corrupt data segments are identified in the first average, they are replaced with data from the second average. This replaced data is similar to what we would have achieved if the data were reacquired. The data from the third volunteer were acquired with 264x256 pixels, a resolution of 0.6mm x 0.6mm x 2mm, 12 echoes per segment, 2 averages and a TR/TE of 2.5s/61ms.

To measure the dispersion of the error function, we first determine any rigid-body translation (*dx(t)* and *dy(t)* in Eq. [5.5]) by measuring the offset of the correlation function from the origin (40). The dispersion of the error function is then measured with a weighted summation such that pixels far from the error function's origin (expected to increase with error function broadening) contribute more significantly to the total summation. While several weighting schemes were tested, a simple linear weighting was found to give the most robust results. Additionally, since the maximum value of $c_L(x,y,t)$ varies depending on which two data segments are compared, $c_L(x,y,t)$ is normalized to unity prior to measuring dispersion. The error function is estimated as:

$$D_L(t) = \frac{\sum_{x=-n}^{n} \sum_{y=-n}^{n} \left| c_L\left(x - dx(t), y - dy(t), t\right) \right| \cdot x \cdot y}{\max_{x,y} \left| c_L(x, y, t) \right|} \qquad [5.6]$$

where n=ceil(0.5*N_{Line}*Δy) selects the central copy of the aliased error function which repeats every $N_{Line}\Delta y$ pixels. When data are analyzed from multiple receive channels, dispersion is calculated for each channel independently and the results are averaged. If there are just a few corrupt data segments, then the standard deviation of the dispersion will be low and any segments with a dispersion more than one or two standard deviations from the mean are identified as corrupt.

5.4 Results

Since the error function in Eq. [5.5] is aliased and two-dimensional, we only display the central portion of a profile through the origin of the error function (in the phase encode direction). While showing just a profile of a two-dimensional error function does not yield a complete picture, it is sufficient for display purposes to show a trend or general concept. The actual motion detection is based on the dispersion of the error function (Eq. [5.6]) and considers the two-dimensional error function rather than the profiles shown in the figures.

The average error function profile for a volunteer who swallowed during an axial 2D TSE neck scan is shown in Fig. 5.1. The data set contains 32 segments with one segment corrupted when the volunteer swallowed. The solid line shows the average error function profile found from comparing all adjacent data segments except the ones including the corrupt data segment. The deviation of the error function profiles are shown by the error

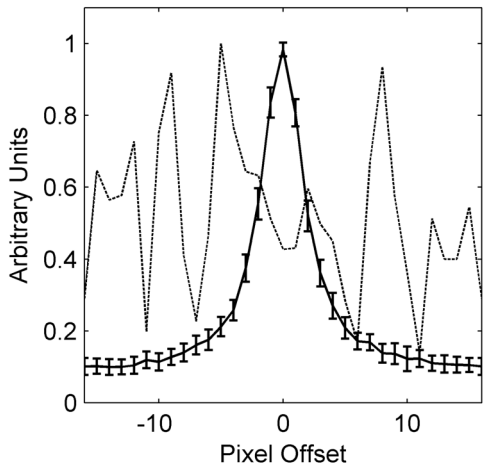

Figure 5.1: Error function dispersion for a volunteer who swallowed during an axial 2D TSE neck scan. The solid line shows a plot through the average error function obtained from comparing all sets of adjacent data segments excluding the segment where swallowing occurred. The error bars on the solid line indicate the standard deviation of all these error functions. The dashed line is a plot through the error function when the volunteer swallowed.

bars on the solid line. For comparison, the dashed line in Fig. 5.1 shows how much the error function changes when motion corruption, swallowing in this case, is present.

The results of two volunteer studies are summarized in Fig. 5.2. First a volunteer was asked to lie still during the first part of the scan and then to nod their head down, hold it for a few seconds and then return their head to the original position as best they could. The dispersion of the error function, as measured with Eq. [5.6], is shown in Fig. 5.2a. In the second study the volunteer was asked to slightly rotate their head for a second (about one degree), return to the original position and then swallow several times near the end of the scan (Fig. 5.2b). All instances of the motion are clearly discernable when

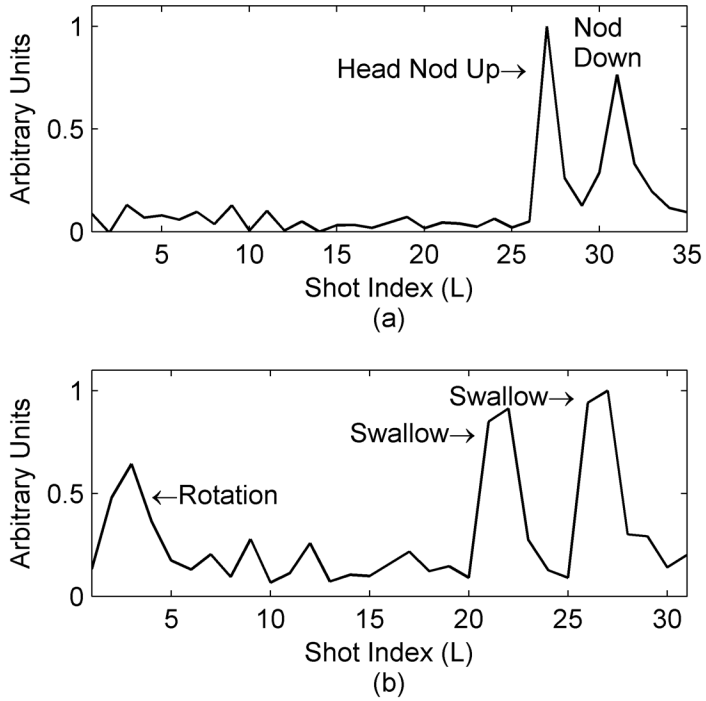

Figure 5.2: Detection of volunteer motion using the error function dispersion. Both plots are the error function dispersion for two different volunteers. The first volunteer (a) nodded their head down, held it for a few seconds and then returned to the original position near the end of the scan (TR/TE=1.5s/6.8ms, 7 echoes per echo train with 36 echo trains required to fill k-space). The second volunteer (b) slightly rotated their head and quickly returned to the original position near the start of the scan and then swallowed during later acquisitions (TR/TE=1.5s/8.6ms, 16 echoes per echo train with 32 echo trains required to fill k-space).

considering the dispersion of the error function.

The ability to detect object motion is also dependent on the sensitivity profile of the coil element being considered. The sensitivities of a two element coil are shown in Fig. 5.3. While both elements were almost equally sensitive to the volunteer rotating their neck (Fig. 5.3c), the anterior element (dashed line in Fig. 5.3b) was more sensitive to volunteer swallowing than the posterior element (solid line in Fig. 5.3b).

Finally, the proposed self-navigating correction technique is applied to a volunteer neck study as shown in Fig. 5.4. The motion corrupted image is shown in Fig. 5.4a with the corrected image shown in Fig. 5.4b. Several corrupt data segments appear in the original error function dispersion (dashed line in Fig. 5.4c). Once these corrupt data

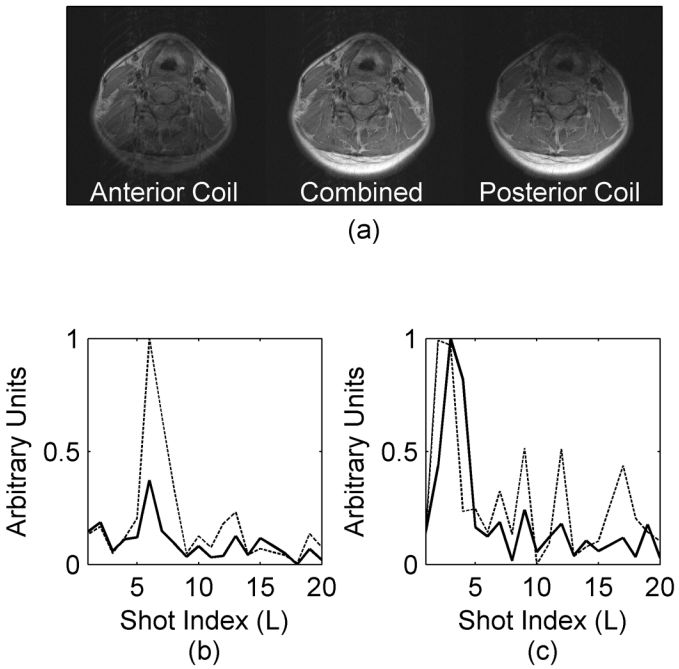

Figure 5.3: Receive coil dependence of error function dispersion. The images in (a) are the anterior coil only (left), both coils combined with a sum of squares (center) and the posterior coil only (right). The solid lines in the graphs are from the posterior receive coil while the dashed lines are from the anterior receive coil. The volunteer swallowed during the acquisition in (b) while the head was rotated during the acquisition in (c).

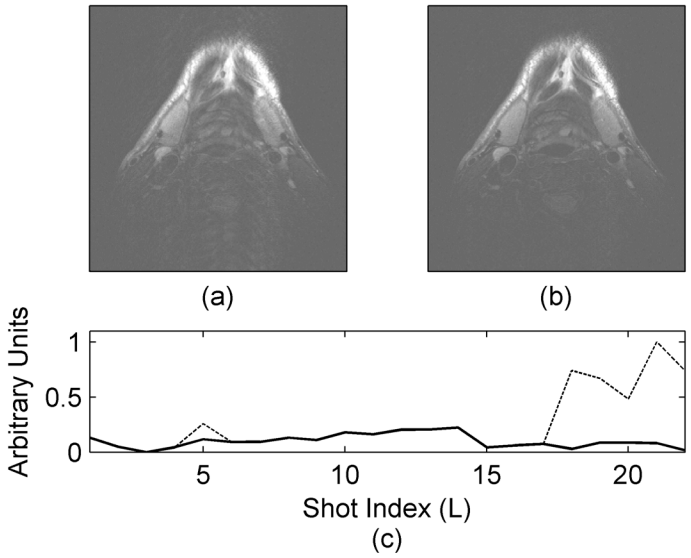

Figure 5.4: Motion artifact reduction using the proposed intrinsic detection technique. The motion corrupted image is shown in (a) with the corrected image shown in (b). The dashed line in (c) is the original error function dispersion. After corrupted data segments were identified and replaced, the resulting error function dispersion is shown in (c) by the solid line. Data was acquired with a 4 element receive coil, a resolution of 0.6mm x 0.6mm x 2mm, 12 echoes per segment, 22 segments to fill k-space and a TR/TE of 2.5s/61ms.

segments are replaced with reacquired data, the error function dispersion no longer shows the presence of the corrupted data segments (solid line in Fig. 5.4c).

5.5 Discussion

In our prior work we demonstrated that rigid-body translation can be detected and compensated using the correlation of adjacent data segments (40). This work deals primarily with the detection of data measurements corrupted by other types of motion. It does not solve the problem of correcting the corrupt data, but instead requires motion corrupted measurements to be reacquired or eliminated during reconstruction. This error function-based motion detection method is based on two enabling observations: First, in the absence of motion, the error function obtained from the correlation of any two

adjacent data segments remains strongly peaked near the origin. Second, when motion not classified as non-rigid-body translation occurs, the error function becomes spread or dispersed with a greatly diminished or missing peak.

We note that a combination of rigid-body translation with other types of object motion (such as out-of-plane motion or swallowing) may distort the error function appreciably so that it is not possible to quantify the rigid-body translation. However, even if the rigid-body translation could be quantified in this case, the data would still be corrupted with the other types of motion and a correction of just rigid-body translation would result in limited improvements.

Another limitation comes when the data are analyzed in a retrospective manner. In this case, even when the object's motion occurs over a single segment of data, two segment comparisons with correspondingly high measures of dispersion are observed. For example, in the second study in Fig. 5.2, where the volunteer swallowed during the acquisition of the 22^{nd} data segment (Fig. 5.2b), both the error functions at L=21 (comparing the 21^{st} and 22^{nd} data segments) and at L=22 (comparing the 22^{nd} and 23^{rd} data segments) show a large dispersion. Hence object motion will typically result in two or more closely spaced peaks in the measure of error function dispersion. In this case, the motion corrupted segment is detected as the only segment with high dispersion on both adjacent comparisons. Segments that have a high dispersion in only one adjacent comparison are likely not corrupted by motion. Motions over longer periods of time can involve more segments and require a more complicated analysis to determine which lines are corrupted.

The proposed technique detects in which segments motion is likely to have occurred,

but does not quantify the motion or discern the type. Additional information about the motion type can be discerned by analyzing individual coils. With the two channel coil utilized in this study, the posterior receive coil is less sensitive to swallowing than the anterior receive coil (Fig. 5.3b) because motion in the neck due to swallowing is mostly limited to the anterior portion of the neck. Conversely, both receive coils appear to be equally sensitive to the rotation (Fig. 5.3c) since the entire image is affected by that type of motion. One point of interest is that the anterior element appears to detect the rotation one segment earlier than the posterior element (Fig. 5.3c). We note that while lying on a table, a rotation of the neck tends not to be rigid-body and the rotation is about a point in the posterior of the neck rather than the middle. As a result, the anterior part of the neck moves more than the posterior during the rotation and may therefore be detected as moving first.

In most cases, the number of corrupted data segments is small and the corrupted lines can be reacquired, or can be recreated using parallel imaging techniques (46), a constrained reconstruction (47), or a variety of other methods being studied by our group and others to deal with motion corrupted data.

5.6 Conclusion

When segmented data are acquired in sets of adjacent lines in k-space (as it is often done in TSE and segmented GRE techniques), this work has demonstrated that correlations between data sets can be exploited to detect various types of motion. While in most cases the motion can not be fully quantified, the method provides a valuable and simple way to detect corrupted data so that it can be reacquired prospectively or removed from the data set retrospectively.

5.7 Acknowledgments

This work has been supported by NIH R01 HL48223, NIH R01 HL57990, Siemens Medical Solutions, the Mark H. Huntsman Endowed Chair, and the Ben B. and Iris M. Margolis Foundation.

5.8 References

1. Eviatar H, Schattka B, Sharp J, Rendell J, Alexander M. Real time head motion correction for functional MRI. In Proceedings of the International Society for Magnetic Resonance in Medicine, Philadelphia, Pennsylvania, 1999. p. 269

2. Zaitsev M, Dold C, Sakas G, Hennig J, Speck O. Magnetic resonance imaging of freely moving objects: prospective real-time motion correction using an external optical motion tracking system. Neuroimage 2006;31:1038-1050.

3. Speck O, Hennig J, Zaitsev M. Prospective real time slice-by-slice motion correction for functional MRI in freely moving subjects. MAGMA 2006;19:55-61.

4. Aksoy M, Newbould R, Straka M, Holdsworth S, Skare S, Santos J, Bammer R. A real time optical motion correction system using a single camera and 2D marker. In Proceedings of the International Society for Magnetic Resonance in Medicine, Toronto, Canada, 2008. p. 3120

5. Qin L, Geldersen P, Zwart J, Jin F, Tao Y, Duyn J. Head movement correction for MRI with a single camera. In Proceedings of the International Society for Magnetic Resonance in Medicine, Toronto, Canada, 2008. p. 1467

6. Chan CF, Gatehouse PD, Hughes R, Roughton M, Pennell DJ, Firmin DN. Novel technique used to detect swallowing in volume-selective turbo spin-echo (TSE) for carotid artery wall imaging. J Magn Reson Imaging 2009;29:211-216.

7. Krueger S, Schaeffter T, Weiss S, Nehrke K, Rozijn T, Boernert P. Prospective intra-image compensation for non-periodic rigid body motion using active markers. In Proceedings of the International Society for Magnetic Resonance in Medicine, Seattle, Washington, 2006. p. 3196

8. Derbyshire JA, Wright GA, Henkelman RM, Hinks RS. Dynamic scan-plane tracking using MR position monitoring. J Magn Reson Imaging 1998;8:924-932.

9. Tremblay M, Tam F, Graham SJ. Retrospective coregistration of functional MRI data using external monitoring. Magn Reson Med 2005;53:141-149.

10. Marxen M, Marmurek J, Baker N, Graham S. Correcting magnetic resonance k-space data for in-plane motion using an optical position tracking system. Med Phys 2009;36:5580-5585.

11. Korin HW, Felmlee JP, Riederer SJ, Ehman RL. Spatial-frequency-tuned markers and adaptive correction for rotational motion. Magn Reson Med 1995;33:663-669.

12. Pipe JG. Motion correction with PROPELLER MRI: application to head motion and free-breathing cardiac imaging. Magn Reson Med 1999;42:963-969.

13. Liu C, Bammer R, Kim D, Moseley ME. Self-navigated interleaved spiral (SNAILS): application to high-resolution diffusion tensor imaging. Magn Reson Med 2004;52:1388-1396

14. Glover GH, Lai S. Self-navigated spiral fMRI: interleaved versus single-shot. Magn Reson Med 1998;39:361-368.

15. Bookwalter C, Griswold M, Duerk J. Multiple overlapping k-space junctions for investigating translating objects (MOJITO). IEEE Trans Med Imaging 2009.

16. Mendes J, Roberts J, Parker D. Hybrid radial-cartesian MRI. In Proceedings of the International Society for Magnetic Resonance in Medicine, Berlin, Germany, 2007. p. 194

17. Lustig M, Cunningham C, Daniyalzade E, Pauly J. Butterfly: A self navigating cartesian trajectory. In Proceedings of the International Society for Magnetic Resonance in Medicine, Berlin, Germany, 2007. p. 194

18. Maclaren JR, Bones PJ, Millane RP, Watts R. MRI with TRELLIS: a novel approach to motion correction. Magn Reson Imaging 2008;26:474-483.

19. Zang LH, Fielden J, Wilbrink J, Takane A, Koizumi H. Correction of translational motion artifacts in multi-slice spin-echo imaging using self-calibration. Magn Reson Med 1993;29:327-334.

20. Welch EB, Felmlee JP, Ehman RL, Manduca A. Motion correction using the k-space phase difference of orthogonal acquisitions. Magn Reson Med 2002;48:147-156.

21. Ehman RL, Felmlee JP. Adaptive technique for high-definition MR imaging of moving structures. Radiology 1989;173:255-263.

22. Lin W, Huang F, Börnert P, Li Y, Reykowski A. Motion correction using an enhanced floating navigator and GRAPPA operations. Magn Reson Med 2009.

23. Kadah YM, Abaza AA, Fahmy AS, Youssef AM, Heberlein K, Hu XP. FNAV for in-plane 2D translational motion estimation. Magn Reson Med 2004;51:403-407.

24. Fu ZW, Wang Y, Grimm RC, Rossman PJ, Felmlee JP, Riederer SJ, Ehman RL. Orbital navigator echoes for motion measurements in magnetic resonance imaging. Magn Reson Med 1995;34:746-753.

25. Costa AF, Petrie DW, Yen Y, Drangova M. Using the axis of rotation of polar navigator echoes to rapidly measure 3D rigid-body motion. Magn Reson Med 2005;53:150-158.

26. Welch EB, Manduca A, Grimm RC, Ward HA, Jack CRJ. Spherical navigator echoes for full 3D rigid body motion measurement in MRI. Magn Reson Med 2002;47:32-41.

27. Larkman DJ, Atkinson D, Hajnal JV. Artifact reduction using parallel imaging methods. Top Magn Reson Imaging 2004;15:267-275.

28. Sodickson DK, Manning WJ. Simultaneous acquisition of spatial harmonics (SMASH): fast imaging with radiofrequency coil arrays. Magn Reson Med 1997;38:591-603.

29. Bydder M, Atkinson D, Larkman DJ, Hill DLG, Hajnal JV. SMASH navigators. Magn Reson Med 2003;49:493-500.

30. Pruessmann KP, Weiger M, Scheidegger MB, Boesiger P. SENSE: sensitivity encoding for fast MRI. Magn Reson Med 1999;42:952-962.

31. Bammer R, Aksoy M, Liu C. Augmented generalized SENSE reconstruction to correct for rigid body motion. Magn Reson Med 2007;57:90-102.

32. Felmlee JP, Ehman RL, Riederer SJ, Korin HW. Adaptive motion compensation in MR imaging without use of navigator echoes. Radiology 1991;179:139-142.

33. Tang L, Ohya M, Sato Y, Tamura S, Naito H, Harada K, Kozuka T. MRI artifact cancellation for translational motion in the imaging plane. In IEEE Nucl Sci Symp Med Imag Conf, 1993. p. 1489-1493

34. Zoroofi RA, Sato Y, Tamura S, Naito H, Tang L. An improved method for MRI artifact correction due to translational motion in the imaging plane. IEEE Trans Med Imaging 1995;14:471-479.

35. Hedley M, Yan H, Rosenfeld D. Motion artifact correction in MRI using generalized projections. IEEE Trans Med Imaging 1991;10:40-46.

36. Zoroofi RA, Sato Y, Tamura S, Naito H. MRI artifact cancellation due to rigid motion in the imaging plane. IEEE Trans Med Imaging 1996;15:768-784.

37. Atkinson D, Hill DL, Stoyle PN, Summers PE, Keevil SF. Automatic correction of motion artifacts in magnetic resonance images using an entropy focus criterion. IEEE Trans Med Imaging 1997;16:903-910.

38. Manduca A, McGee KP, Welch EB, Felmlee JP, Grimm RC, Ehman RL. Autocorrection in MR imaging: adaptive motion correction without navigator echoes. Radiology 2000;215:904-909.

39. Wood ML, Shivji MJ, Stanchev PL. Planar-motion correction with use of k-space data acquired in Fourier MR imaging. J Magn Reson Imaging 1995;5:57-64.

40. Mendes J, Kholmovski E, Parker DL. Rigid-body motion correction with self-navigation MRI. Magn Reson Med 2009;61:739-747.

41. Welch EB, Rossman PJ, Felmlee JP, Manduca A. Self-navigated motion correction using moments of spatial projections in radial MRI. Magn Reson Med 2004;52:337-345.

42. Shankaranarayanan A, Wendt M, Lewin JS, Duerk JL. Two-step navigatorless correction algorithm for radial k-space MRI acquisitions. Magn Reson Med 2001;45:277-288.

43. Hedley M, Yan H. Suppression of slice selection axis motion artifacts in MRI. IEEE Trans Med Imaging 1992;11:233-237.

44. Mitsa T, Parker KJ, Smith WE, Tekalp AM, Szumowski J. Correction of periodic motion artifacts along the slice selection axis in MRI. IEEE Trans Med Imaging 1990;9:310-317.

45. Hadley JR, Roberts JA, Goodrich KC, Buswell HR, Parker DL. Relative RF coil performance in carotid imaging. Magn Reson Imaging 2005;23:629-639.

46. Griswold MA, Jakob PM, Heidemann RM, Nittka M, Jellus V, Wang J, Kiefer B, Haase A. Generalized autocalibrating partially parallel acquisitions (GRAPPA). Magn Reson Med 2002;47:1202-1210.

47. Karniadakis GEM, Kirby II RM. Parallel scientific computing in C++ and MPI. Cambridge:Cambridge University Press;2003.

CHAPTER 6

CINE TURBO SPIN ECHO IMAGING[1]

While high resolution TSE images have demonstrated important details of carotid artery morphology, it is evident that pulsatile blood and wall motion related to the cardiac cycle are still significant sources of image degradation. Although ECG gating can reduce artifacts due to cardiac induced pulsations, gating is rarely used because it lengthens the acquisition time and can cause image degradation due to nonconstant TR. This work introduces a relatively simple method of converting a conventional TSE acquisition into a retrospectively ECG correlated cineTSE sequence. The cineTSE sequence generates a full sequence of ECG correlated images at each slice location throughout the cardiac cycle in the same scan time that is conventionally used by standard TSE sequences to produce a single image at each slice location. The cineTSE images exhibit reduced pulsatile artifacts associated with a gated sequence but without the increased scan time or associated nonconstant TR effects.

6.1 Introduction

Accurate identification of carotid atherosclerotic plaque composition can better identify those individuals at higher risk for subsequent cerebral embolization and

---

[1]Pending publication in Magnetic Resonance in Medicine.

neuralgic symptoms (1-4). MRI presents an advance over x-ray techniques, including Computed Tomography, because it produces images with a variety of different tissue contrasts. Because MRI can better discriminate soft tissue types, it offers improved discrimination of atherosclerotic plaque components such as hemorrhage, disrupted fibrous cap, lipid/necrotic core, calcification and ulceration. TSE (Turbo Spin Echo or Fast Spin Echo) pulse sequences, with efficient acquisition of T1, T2 and proton density weighted images, have become useful in the evaluation of cervical carotid artery disease (5-7). High resolution 3D TSE techniques would be valuable in carotid MRI, but motion artifacts that arise due to the relatively long data-acquisition time result in an unacceptable fraction of non-interpretable studies. As a result, nearly all clinical cervical carotid MRI studies are performed with 2D TSE techniques, with double inversion blood suppression, where motion artifacts corrupt a smaller fraction of studies and motion in one slice does not cause artifacts in an adjacent slice. However, in many subjects, even 2D TSE techniques result in obvious blurring or ghosting artifacts that greatly reduce the quality of the images.

Motion artifacts due to swallowing and other neck muscle movements can be reduced by applying parallel imaging techniques to reduce the acquisition time (8-10). Reduced field of view sequences with more efficient double inversion blood suppression have also shown reduced susceptibility to these types of motion artifacts (11, 12). Single shot sequences, such as Half Fourier Acquisition Single Shot Turbo Spin Echo, can also be used to reduce acquisition time and hence the susceptibility to certain motion artifacts (13). However, single shot techniques tend to have image blurring due to T2 decay. Navigators and dedicated motion detection RF coils have been shown to be successful in

detecting and rejecting data corrupted by swallowing (14, 15). Using average specific phase encoding ordering or comparing adjacent sets of k-space data lines are alternative methods for detecting data corrupted by patient motion (16-18).

Motion artifacts that are correlated to the cardiac cycle can be greatly reduced by synchronizing data acquisition with the heart cycle using electrocardiogram (ECG) gating. Cine sequences based on gradient echo or true fast imaging with steady state procession have shown the dynamic nature of the carotid artery and cyclic blood flow (19, 20). Gradient echo based pulse sequences typically have a very short repetition time (TR<30ms) and can therefore be efficiently designed as cine sequences to obtain complete image measurements at multiple cardiac phases in the same acquisition. However, because of the relatively long TR of TSE techniques (> 500ms), ECG gated acquisitions typically obtain only one image at a single cardiac phase. For example, ECG gated acquisitions have been used reduce the effect of cardiac motion by acquiring data during diastole (21-23). Reduced field of view GRASE with cardiac gating has been shown to generate reasonable images of carotid plaque (24). However, ECG gating can result in image degradation due to noncontrast TR times (25). This problem can be improved by limiting gating to just the central portion of k-space, however, the effect of a variable TR is still noticeable (26).

This work introduces a novel and relatively simple method of converting a conventional TSE acquisition into a retrospectively ECG correlated cineTSE sequence. Because the cineTSE images are ECG correlated they exhibit the reduced pulsatile artifacts obtained with gated sequences. Additionally, cineTSE generates a full sequence of ECG correlated images at each slice location throughout the cardiac cycle in the same

scan time that is conventionally used by standard TSE sequences to produce a single image at each slice location. Given that the data is acquired with the same timing as a standard TSE sequence, there are no nonconstant TR effects such as are typically associated with gated sequences. In this work, the basic theory of the cineTSE method is presented and supported with data from several patients with and without carotid disease.

6.2 Theory

Information about the patient's cardiac cycle is recorded during the MR scan utilizing ECG information or a pulse oximeter. Because the pulse oximeter is less susceptible to gradient induced noise and requires less patient preparation, it has been utilized exclusively in this work. Hence the term ECG correlation is applied generally to correlating MRI data to the patient's cardiac cycle, regardless of the method used to monitor the cardiac cycle. The acquired k-space data lines are sorted into N_t temporal bins according to the time elapsed since the last systolic trigger. The result is N_t undersampled data bins, each representing a different phase of the cardiac cycle. The undersampled images are reconstructed by simultaneously considering information encoded by the coil sensitivities as well as applying a temporal constraint. This is accomplished by minimizing the following objective function:

$$G = \left\| W(k_x, k_y, t) \cdot \Im_{xy}[s_n(x,y) \cdot m(x,y,t)] - d_n(k_x, k_y, t) \right\|_2^2 + \left\| \lambda(x,y) \cdot \nabla_t [m(x,y,t)] \right\|_2^2 \qquad [6.1]$$

where t is the time (bin number) in the cardiac cycle, $W(k_x,k_y,t)$ is a weight function specifying which lines in k-space have been acquired in each bin, $\Im_{xy}()$ is the 2D Fourier transform along the spatial coordinates, $s_n(x,y)$ is the coil sensitivity of the n^{th} coil, $d_n(k_x,k_y,t)$ is the actual data acquired from the n^{th} coil in a given bin, $\lambda(x,y)$ specifies the level of temporal constraint and $\nabla_t()$ is a temporal gradient. Since $m(x,y,t)$ is periodic in

time, we have found the following definition of $\nabla_t()$ to be optimal compared to methods that estimate the temporal gradient using only a few surrounding points in time.

$$\nabla_t\left[m(x,y,t)\right] = \Im_t^{-1}\left\{\Im_t\left[m(x,y,t)\right]\cdot\frac{2\pi i f}{N_t}\right\}. \qquad [6.2]$$

Equation [6.1] is minimized using the following gradient term:

$$\nabla_m G = -2\lambda^2\nabla_t^2(m) + 2\sum_n s_n^* \cdot \Im_{xy}^{-1}\left[W\cdot\Im_{xy}(s_n m) - d_n\right]. \qquad [6.3]$$

The images are then reconstructed using a non-linear conjugate gradient descent algorithm in conjunction with the objective function in Eq. [6.1] and the gradient term in Eq. [6.3] (27-29).

6.3 Methods

6.3.1 Data Acquisition

All studies were performed on a Siemens Trio 3T MRI scanner with custom designed four or 16-element phased array surface coils and a modified TSE sequence (30, 31). All human studies were approved by the institutional review board and informed consent was obtained from all subjects.

In this cineTSE technique, the cardiac cycle is divided into a number of bins and each individual echo in a TSE echotrain is assigned to a bin based upon its time in the cardiac cycle. Because the readout of an echotrain can require over 100ms (sometimes as much as 200ms), it is not uncommon for echoes from the same echotrain to be placed into different bins. To help ensure that each temporal data bin contains a sufficient number of lines near the center of k-space (where most of the image energy is found), the product TSE sequence was modified to more frequently sample the center of k-space and to record the patient's cardiac cycle utilizing a pulse oximeter. To prevent an increase in

scan time, this is accomplished at the cost of missing varying lines near the edge of k-space in each average. Every line of k-space is sampled at least once during the entire acquisition. Figure 6.1 shows a typical sampling density resulting from the modified TSE sequence where the equivalent of two averages is acquired.

Data used to generate T2 weighted images and plots were acquired with a T2 weighted cineTSE sequence with the four element coil, two averages, a resolution of 0.6mm x 0.6mm x 2mm, 12 echoes per train and a TR/TE of 2.5s/61ms. The T1 weighted data were acquired with a T1 weighted cineTSE sequence with the 16-element coil, two averages, a resolution of 0.5mm x 0.5mm x 2mm, 12 echoes per train and a TR/TE of 650ms/8ms. Twelve slices locations were imaged for both T1 and T2 weighted cineTSE acquisitions. Typical scan time for the T1 or T2 weighted cineTSE sequences is about 4.5 minutes.

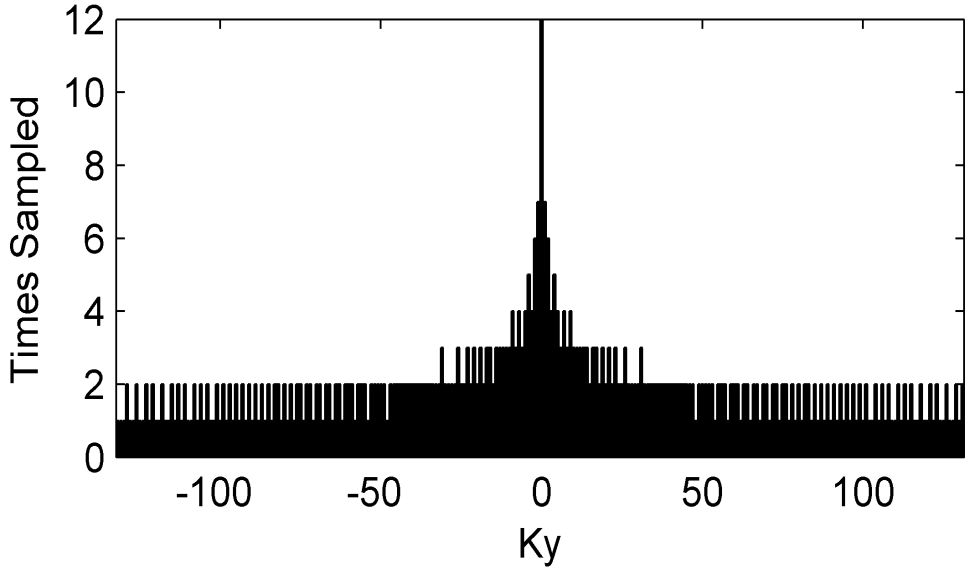

Figure 6.1 Typical sampling density with a TSE sequence used in this study. In this case 528 lines were sampled from a k-space spanning 264 lines. This corresponds to the same number of lines that would have been sampled with two full averages and a uniform sampling density.

6.3.2 Image Reconstruction

In this work we are reconstructing only magnitude images and it is sufficient to estimate the coil sensitivities, $s_n(x,y)$, as:

$$s_n(x,y) = \frac{m_n(x,y)}{\sqrt{\varepsilon + \sum_n m_n(x,y) m_n^*(x,y)}} \quad [6.4]$$

where ε is a small constant and $m_n(x,y)$ is the image estimate from the nth coil. In cases where phase information from the final images is required, a more specific measure of the coil sensitivities is required.

Since we are correlating our data to the cardiac cycle, it should be consistent to constrain pixels varying with frequencies unrelated to the heart rate more strongly than those varying at frequencies near the heart rate. This can be accomplished in our choice of the spatially varying temporal constraint, $\lambda(x,y)$, as:

$$\lambda(x,y) = \sum_f \Im_t[m(x,y,t)] \cdot \alpha(f) \quad [6.5]$$

where $\alpha(f)$ is a bandpass filter selecting the frequency components occurring near the patients average heart rate. In this study, $\lambda(x,y)$ is scaled to a range of 0 (where pixels vary near the patients heart rate) to ~0.1 (where the pixel variations seem uncorrelated to the cardiac cycle). In addition, we constrain the temporal map to be smooth by convolving the result of Eq. [6.5] with a Gaussian (FWHM of ~8 pixels). A representative image slice and the corresponding temporal constraint, $\lambda(x,y)$, are shown in Fig. 6.2. The acquired data, $d_n(k_x,k_y,t)$, is scaled so that our final image, $m(x,y,t)$, has a magnitude range of approximately 0~1.0.

Since missing data lines are calculated using coil sensitivities and a temporal

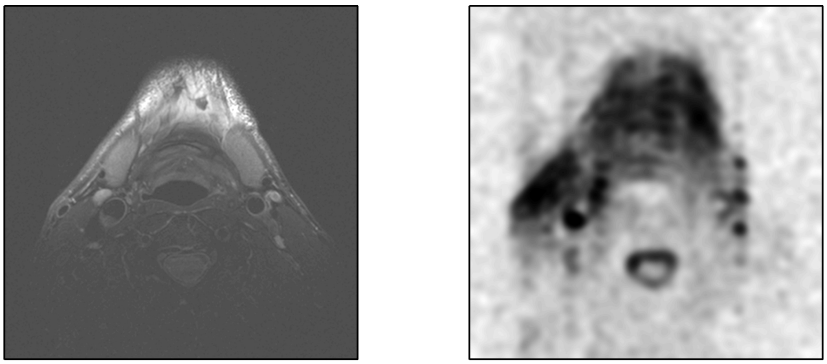

Figure 6.2: TSE data set with the corresponding spatially varying temporal constraint. The standard TSE image is shown in (a) along with $\lambda(x,y)$ (see Eq.[6.6]) shown in (b). The temporal constraint map (b) is a maximum in areas where pixel fluctuations have little correlation to the cardiac cycle and a minimum in areas where the fluctuations correlate highly with the cardiac cycle.

constraint, there is a practical limit on the number of temporal data bins the data should be sorted into. Two few data bins might not allow enough temporal resolution to observe important events in the cardiac cycle. Too many bins will impose a computational burden on the iterative reconstruction without yielding a significant increase in dynamic information. We have found that sorting data into more than 12 temporal data bins, when two data averages have been acquired, does not yield significant improvements to the results. Therefore, unless specified, all data are sorted into 12 temporal data bins.

The cineTSE sequence acquires data independent of the cardiac cycle and as a result some of the acquired data lines may occur on or near the dividing boundary of data bins in the cardiac cycle. These data may reasonably be sorted into more than one temporal data bin. Such an effect can be taken into account by allowing our data bins to overlap slightly. We have found that an overlap of 30% is enough to help ensure each data bin contains an adequate amount of data but not too much to blur results in the temporal

direction.

Finally, during the sorting process it is possible at times to sample a particular line of data in a given data bin multiple times. One way to include this effect is to allow $W(k_x,k_y)$ to assume values other than 0 or 1. Alternatively, we can average any line that is sampled more than once and keep the original definition of $W(k_x,k_y)$. It has been found that the averaging method yields similar results to the first but is less computationally demanding. As a result, any data line that is sampled multiple times in a particular bin (which does not typically occur very often) is simply averaged.

6.4 Results

Figure 6.3a displays a T2 weighted TSE image reconstructed in a standard way from a volunteer (four element coil and two data averages). The arrow in Fig. 6.3a shows a flow artifact in the carotid artery just below the bifurcation. Figure 6.3b shows six images, among 12 total images, obtained from the same data set as Fig. 6.3a but reconstructed using the cineTSE technique. These six images are selected with equal spacing in the cardiac cycle at the times shown on the average pressure pulse in Fig. 6.3c. The flow artifact is seen to come and go throughout the cardiac cycle and can easily be identified in the cineTSE images (arrows in Fig. 6.3b).

Improvement of vessel wall depiction using a T2 weighted cineTSE is shown in Fig. 6.4. Profiles through a carotid artery are observed in two orthogonal directions (location of profiles are indicated in Fig. 6.4a by the white lines). Figures 6.4b and 6.4c are the profiles along the horizontal (frequency encode) and vertical (phase encode) directions respectively. The dashed lines in Figs. 6.4b and 6.4c are the profiles measured when a standard TSE sequence with two averages is used while the solid line is the result from

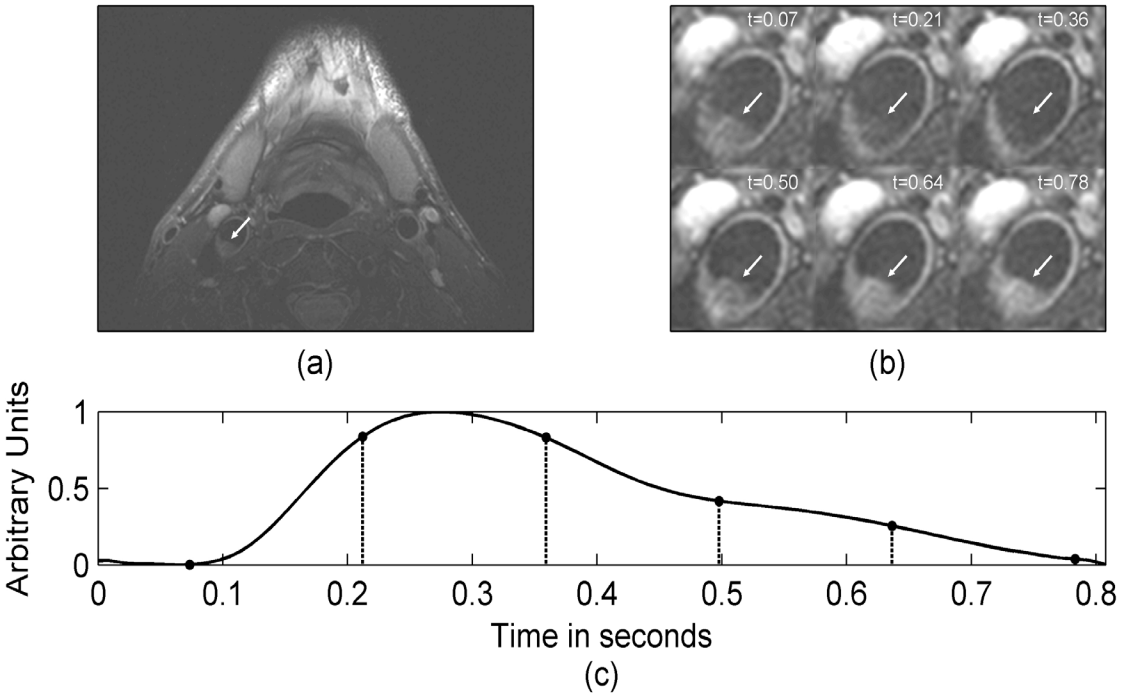

Figure 6.3: Flow artifact identification using a T2 weighted cineTSE reconstruction (4 channel receive coil and 2 data averages). The standard TSE image (a) exhibits a flow artifact indicated by the arrow. Six equally spaced images in the cardiac cycle (of 12 total images) from the cineTSE reconstruction are shown in (b). The time (in seconds) of each of the 6 images relative to the systolic trigger is indicated by the text on each image (b) as well as the dashed lines on the average pressure pulse waveform shown in (c).

a systolic image obtained by reconstructing the same data using the cineTSE technique. The discrepancy in vessel wall thickness is especially evident in the phase encode direction (Fig. 6.4c).

T1 weighted cineTSE images from a patient with an ulceration of plaque in their carotid artery are shown in Fig. 6.5. Each column contains images from the same three consecutive slices. Figure 6.5a contains the standard TSE images with two averages. Figures 6.5b and 6.5c show images reconstructed with the cineTSE technique in the systolic and diastolic phases respectively. Figure 6.5d shows the signal difference between the systolic and diastolic cineTSE images. The arrows on each slice indicate

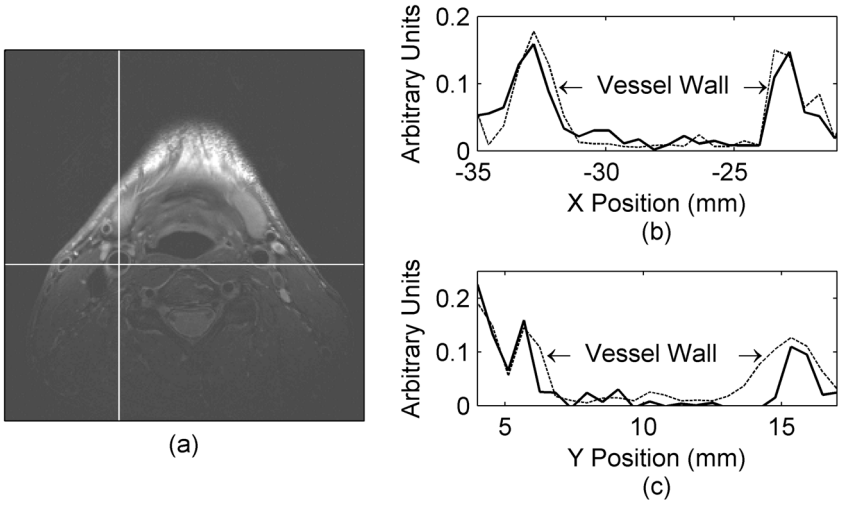

Figure 6.4: Improvement of vessel wall depiction using a T2 weighted cineTSE reconstruction (4 channel receive coil and 2 data averages). Two profiles are taken in orthogonal directions across a carotid artery as indicated by the white lines on the image in (a). The horizontal line is in the readout direction with the associated profiles shown in (b) while the vertical line is in the phase encode direction with the associated profiles shown in (c). The dashed lines in (b) and (c) represent the profile taken form the standard TSE image while the solid line is taken from a systolic image in the cineTSE reconstruction.

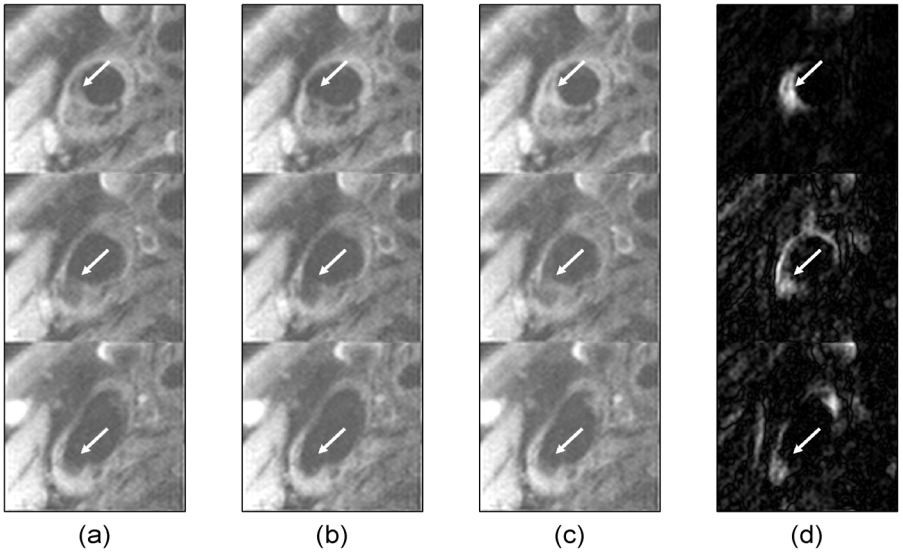

Figure 6.5: T1 weighted cineTSE images of carotid disease (16 channel receive coil, 2 averages). Each column contains the same three consecutive slices. Standard TSE images are shown in (a), systolic cineTSE images in (b), diastolic cineTSE images in (c) with the difference between systolic and diastolic images shown in (d).

areas where flow artifact might obscure the true nature of the plaque.

The motion of a valve in a facial vein is captured with a T2 weighted cineTSE reconstruction as shown in Fig. 6.6. Figure 6.6a shows the standard TSE image with the average pressure waveform shown in Fig. 6.6b. Twelve cineTSE images of the valve, obtained from the same data set in Fig. 6.6a but reconstructed using a cineTSE technique, are shown in Fig. 6.6c. The time of each cineTSE image in the cardiac cycle is indicated in Fig. 6.6b. Where a typical TSE gated sequence returns images at one or two time points, the cineTSE sequence delivers a whole set of images without an increase in scan time.

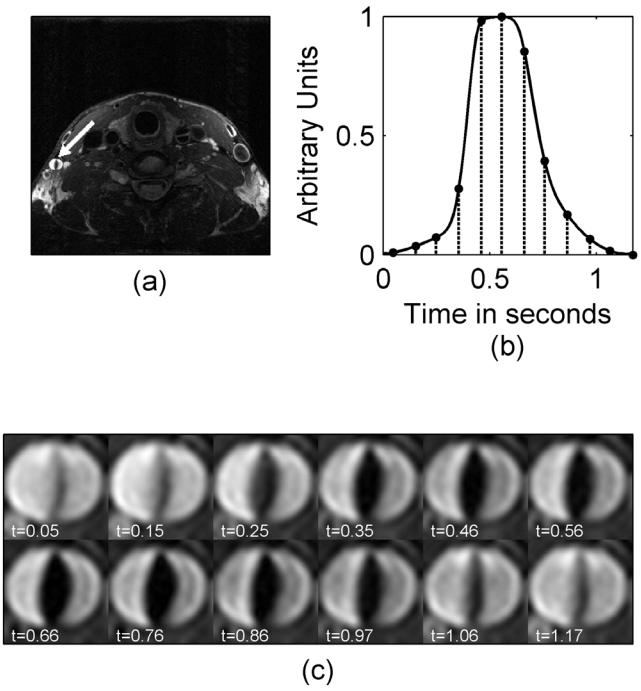

Figure 6.6: Depiction of a valve captured with a T2 weighted cineTSE reconstruction (four channel receive coil and two data averages). The location of the valve is indicated by the arrow on the standard TSE image in (a). Close up view of the valve for all 12 equally spaced images across the cardiac cycle is shown in (c). The time (in seconds) of each of the 12 images relative to the systolic trigger is indicated by the text on each image (c) as well as the dashed lines on the average pressure pulse waveform shown in (b).

While the cineTSE technique is designed to eliminate cardiac related motion artifacts, other motion such as swallowing, will still pose a problem. Figure 6.7a shows that two averages in a standard TSE image can help to reduce a swallowing artifact. However, this method eliminates any temporal cardiac information we hope to receive since only a single time frame is reconstructed. When the corrupted data are sorted into multiple temporal bins (Fig. 6.7b) the swallowing artifact returns. The corrupted lines can be detected using data from adjacent data lines or from the same set of lines acquired in different averages (16, 17). These lines can then be removed prior to the cineTSE reconstruction to reduce artifacts due to swallowing (Fig. 6.7c).

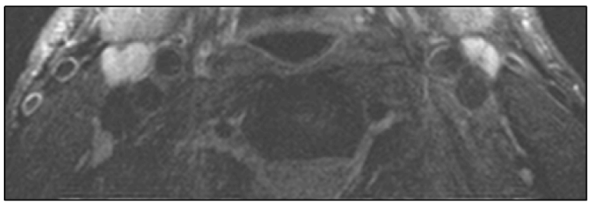

(a)

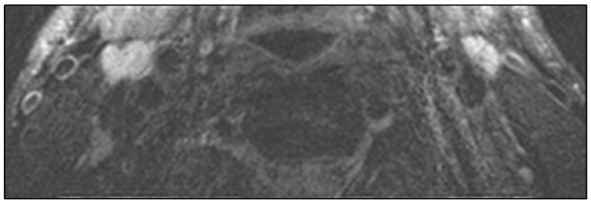

(b)

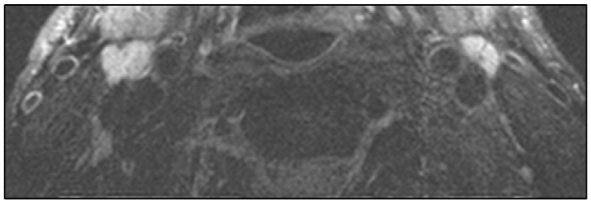

(c)

Figure 6.7: Correction of noncardiac related motion in a T2 weighted cineTSE reconstruction. A standard TSE image with two data averages and volunteer swallowing is shown in (a). A single time frame (of 12 cineTSE cardiac phases) from the motion corrupted data is shown in (b). The same time frame after corrupted data has been detected and removed is shown in (c).

6.5 Discussion

Although ECG gating can reduce artifacts due to cardiac induced pulsations, gating is rarely used because it also lengthens the acquisition time, resulting in increased susceptibility to swallowing and respiratory motion artifacts. In addition, many TSE protocols acquire two or more data averages to increase image signal to noise ratio and to help reduce the amount of motion artifact. One of the main advantages of the cineTSE sequence is that it requires no additional scan time over a standard two average TSE sequence. All the examples shown in this work utilized the equivalent of two data averages as described previously in the Methods section. While a degree of temporal information could be obtained from just a single average of cineTSE data, we have found that in most cases at least two averages are required to yield consistent and accurate temporal information.

A major advantage of the cineTSE sequence is the ability to resolve certain flow artifacts and to discriminate between image signal from tissue and recirculation of blood. This is evident in Figs. 6.3 and 6.5 where residual blood signal may be misinterpreted for tissue wall. In the middle slice of Fig. 6.5, the systolic and diastolic images clearly show the ulceration whereas the conventional image shows a lighter signal in the ulceration that might be interpreted as loose necrotic core. Additionally, it has been shown that in standard sequences pulsatile motion of vessels on the order of 1mm peak to peak can occur, causing major blurring of wall morphology (26). With a cineTSE sequence, it is possible to scroll through a dozen images at different time frames in the cardiac cycle and select the best image(s) with the least residual blood signal to best depict the vessel wall and plaque morphology. For example, Fig. 6.4 shows how using a systolic cineTSE

image, where fast moving blood gives no signal, can be expected to more accurately depicts vessel wall thickness compared to a standard TSE sequence.

T1 weighted images provide image contrast that is complementary to that of T2 weighted images and can therefore help discriminate plaque components. However, T1 weighted images have a short TE such that signal from moving blood is not eliminated completely by the spin echo sequence. To eliminate the signal from moving blood, T1 weighted sequences usually employ a double inversion preparation to eliminate the signal from flowing blood. Double inversion techniques are very time inefficient and require substantially longer acquisition times. Since cineTSE is able to distinguish flow artifacts, it appears that T1 weighted imaging can be performed without double inversion or other flow suppression techniques (Fig. 6.5). If blood signal can be detected and eliminated from analysis of T1 weighted cineTSE images, then the cineTSE technique will substantially decreases the scan time typically required for standard T1 weighted TSE sequences. In this case, substantially more information will be obtained in less time.

In many cases, flow artifacts can be identified by selecting one or two images from the array of cineTSE images. Since cineTSE produces images at several time points in the cardiac cycle, it is also well suited for applications that measure dynamic variables. Figure 6 shows how cineTSE can capture the dynamic nature of a valve. Because motion of the carotid wall can be more clearly seen with cineTSE than with cineGRE sequences, it is likely that cineTSE coupled with systolic and diastolic pressures will provide an improved mechanism for measuring arterial wall compliance. CineTSE also captures the dynamic motion of cerebrospinal fluid during the cardiac cycle.

An additional highlight of the cineTSE sequence is that the data acquisition is almost

identical to a standard TSE sequence. As a result, many of the motion correction techniques (for noncardiac related motion) developed for standard TSE sequences can be easily applied to the cineTSE sequence (32-38). Because many k-space lines have multiple averages, these data can be used to help detect corrupted data. Additionally, data from adjacent data lines can also be used to detect corruption from patient motion (16, 17). Since we are already dealing with undersampled data, it is not a significant problem if a few lines of data need to be discarded due to noncardiac related motion corruption. As with most sequences, significant amounts of noncardiac related motion will pose a problem. In Fig. 6.7, even though 20% of the data was discarded due to corruption, the cineTSE sequence produced images relatively free of cardiac motion artifact.

While this study focused on cineTSE of the neck, the sequence may easily be applied to other regions of the body, including the heart, where motion synchronized to the cardiac cycle is observed. In the case of cardiac imaging, it is possible to additionally monitor the patient's breathing cycle and correlate data to both cardiac and breathing phases. The concepts presented for 2D cineTSE can also be extended to high resolution 3D sequences.

6.6 Conclusion

In this work a method of converting a conventional TSE acquisition into a retrospectively ECG correlated image sequence was demonstrated. The cineTSE sequence requires no more scan time than conventionally gated TSE sequences. Because cineTSE acquisition is asynchronous with the cardiac cycle, it does not have the problems caused by non-constant TR periods of gated sequences. CineTSE generates a full

sequence of ECG correlated images at each slice location throughout the cardiac cycle in the same scan time that is conventionally used by standard TSE sequences to produce a single image at each slice location. The images show that cineTSE can more accurately identify and allow for measurements of carotid artery plaque components by improving tissue visualization, allowing for identification and exclusion of artifacts and enhancing image quality.

6.7 Acknowledgments

This work has been supported by NIH grants HL48223 and HL57990, as well as grants from the Cumming Foundation, the Ben B. and Iris M. Margolis Foundation, and the Mark H. Huntsman Endowed Chair.

6.8 References

1. Executive Committee for the Asymptomatic Carotid Atherosclerosis Study. Endarterectomy for asymptomatic carotid artery stenosis. JAMA 1995;273:1421-1428.

2. Fox AJ. How to measure carotid stenosis. Radiology 1993;186:316-318.

3. North American Symptomatic Carotid Endarterectomy Trial Collaborators. Beneficial effect of carotid endarterectomy in symptomatic patients with high-grade carotid stenosis. N. Engl. J. Med. 1991;325:445-453.

4. European Carotid Surgery Trialists' Collaborative Group. MRC European carotid surgery trial: interim results for symptomatic patients with severe (70-99%) or with mild (0-29%) carotid stenosis. Lancet 1991;337:1235-1243.

5. Edelman RR, Mattle HP, Wallner B, Bajakian R, Kleefield J, Kent C, Skillman JJ, Mendel JB, Atkinson DJ. Extracranial carotid arteries: evaluation with "black blood" MR angiography. Radiology 1990;177:45-50.

6. Fayad ZA, Fuster V, Nikolaou K, Becker C. Computed tomography and magnetic resonance imaging for noninvasive coronary angiography and plaque imaging: current and potential future concepts. Circulation 2002;106:2026-2034.

7. Edelman RR, Chien D, Kim D. Fast selective black blood MR imaging. Radiology 1991;181:655-660.

8. Griswold MA, Jakob PM, Heidemann RM, Nittka M, Jellus V, Wang J, Kiefer B, Haase A. Generalized autocalibrating partially parallel acquisitions (GRAPPA). Magn Reson Med 2002;47:1202-1210.

9. Pruessmann KP, Weiger M, Scheidegger MB, Boesiger P. SENSE: sensitivity encoding for fast MRI. Magn Reson Med 1999;42:952-962.

10. Sodickson DK, Manning WJ. Simultaneous acquisition of spatial harmonics (SMASH): fast imaging with radiofrequency coil arrays. Magn Reson Med 1997;38:591-603.

11. Kim S, Kholmovski EG, Jeong E, Buswell HR, Tsuruda JS, Parker DL. Triple contrast technique for black blood imaging with double inversion preparation. Magn Reson Med 2004;52:1379-1387.

12. Parker DL, Goodrich KC, Masiker M, Tsuruda JS, Katzman GL. Improved efficiency in double-inversion fast spin-echo imaging. Magn Reson Med 2002;47:1017-1021.

13. Zhang L, Kholmovski EG, Guo J, Choi SK, Morrell GR, Parker DL. HASTE sequence with parallel acquisition and T2 decay compensation: application to carotid artery imaging. Magn Reson Imaging 2009;27:13-22.

14. Chan CF, Gatehouse PD, Hughes R, Roughton M, Pennell DJ, Firmin DN. Novel technique used to detect swallowing in volume-selective turbo spin-echo (TSE) for carotid artery wall imaging. J Magn Reson Imaging 2009;29:211-216.

15. Crowe LA, Keegan J, Gatehouse PD, Mohiaddin RH, Varghese A, Symmonds K, Cannell TM, Yang GZ, Firmin DN. 3D volume-selective turbo spin echo for carotid artery wall imaging with navigator detection of swallowing. J Magn Reson Imaging 2005;22:583-588.

16. Mendes JK, Parker DL. Intrinsic detection of corrupted data. In Proceedings of the International Society for Magnetic Resonance in Medicine, Stockholm, Sweden, 2010. p. 3076

17. Mendes J, Kholmovski E, Parker DL. Rigid-body motion correction with self-navigation MRI. Magn Reson Med 2009;61:739-747.

18. Zhang L, Kholmovski EG, Guo J, Parker DL. TSE with average-specific phase encoding ordering for motion detection and artifact suppression. J Magn Reson Imaging 2007;25:1271-1282.

19. Chow TY, Cheung JS, Wu Y, Guo H, Chan KC, Hui ES, Wu EX. Measurement of common carotid artery lumen dynamics during the cardiac cycle using magnetic resonance TrueFISP cine imaging. J Magn Reson Imaging 2008;28:1527-1532.

20. Honda T, Yano K, Matsuoka H, Hamada M, Hiwada K. Evaluation of aortic distensibility in patients with essential hypertension by using cine magnetic resonance imaging. Angiology 1994;45:207-212.

21. Steinman DA, Rutt BK. On the nature and reduction of plaque-mimicking flow artifacts in black blood MRI of the carotid bifurcation. Magn Reson Med 1998;39:635-641.

22. Saloner D, Selby K, Anderson CM. MRA studies of arterial stenosis: improvements by diastolic acquisition. Magn Reson Med 1994;31:196-203.

23. Crowe LA, Gatehouse P, Yang GZ, Mohiaddin RH, Varghese A, Charrier C, Keegan J, Firmin DN. Volume-selective 3D turbo spin echo imaging for vascular wall imaging and distensibility measurement. J Magn Reson Imaging 2003;17:572-580.

24. Luk-Pat GT, Gold GE, Olcott EW, Hu BS, Nishimura DG. High-resolution three-dimensional in vivo imaging of atherosclerotic plaque. Magn Reson Med 1999;42:762-771.

25. Narumi S, Sasaki M, Ohba H, Ogasawara K, Hitomi J, Mori K, Ohura K, Ono A, Terayama Y. Altered carotid plaque signal among different repetition times on T1-weighted magnetic resonance plaque imaging with self-navigated radial-scan technique. Neuroradiology 2010;52:285-290.

26. Al-Kwifi O, Kim JK, Stainsby J, Huang Y, Sussman MS, Farb RI, Wright GA. Pulsatile motion effects on 3D magnetic resonance angiography: implications for evaluating carotid artery stenoses. Magn Reson Med 2004;52:605-611.

27. Karniadakis GEM, Kirby II RM. Parallel scientific computing in C++ and MPI. Cambridge:Cambridge University Press;2003.

28. Adluru G, Dibella EVR. Reordering for improved constrained reconstruction from undersampled k-space data. Int J Biomed Imaging 2008.

29. Adluru G, Awate SP, Tasdizen T, Whitaker RT, Dibella EVR. Temporally constrained reconstruction of dynamic cardiac perfusion MRI. Magn Reson Med 2007;57:1027-1036.

30. Tate Q, Bell LC, Kim SE, Minalga E, Parker DL, Hadley JR. A 16 channel radio frequency anterior neck coil for imaging of the cervical carotid bifurcation. In Proceedings of the International Society for Magnetic Resonance in Medicine, Stockholm, Sweden, 2010. p. 3841

31. Hadley JR, Roberts JA, Goodrich KC, Buswell HR, Parker DL. Relative RF coil performance in carotid imaging. Magn Reson Imaging 2005;23:629-639.

32. Tang L, Ohya M, Sato Y, Tamura S, Naito H, Harada K, Kozuka T. MRI artifact cancellation for translational motion in the imaging plane. In IEEE Nucl Sci Symp Med Imag Conf, 1993. p. 1489-1493

33. Felmlee JP, Ehman RL, Riederer SJ, Korin HW. Adaptive motion compensation in MR imaging without use of navigator echoes. Radiology 1991;179:139-142.

34. Hedley M, Yan H, Rosenfeld D. Motion artifact correction in MRI using generalized projections. IEEE Trans Med Imaging 1991;10:40-46.

35. Zoroofi RA, Sato Y, Tamura S, Naito H, Tang L. An improved method for MRI artifact correction due to translational motion in the imaging plane. IEEE Trans Med Imaging 1995;14:471-479.

36. Wood ML, Shivji MJ, Stanchev PL. Planar-motion correction with use of k-space data acquired in Fourier MR imaging. J Magn Reson Imaging 1995;5:57-64.

37. Atkinson D, Hill DL, Stoyle PN, Summers PE, Keevil SF. Automatic correction of motion artifacts in magnetic resonance images using an entropy focus criterion. IEEE Trans Med Imaging 1997;16:903-910.

38. Zoroofi RA, Sato Y, Tamura S, Naito H. MRI artifact cancellation due to rigid motion in the imaging plane. IEEE Trans Med Imaging 1996;15:768-784.

CHAPTER 7

CONCLUSIONS

Currently, in clinical practice, there is a low diagnostic utility of MRI to examine carotid disease. According to one study, 15-30% of carotid MR scans are not interpretable for a number of reasons including the inability for the patient to remain motionless for the length of the scan (1). This unacceptable fraction of noninterpretable studies can be reduced with the motion detection and correction techniques in this thesis.

7.1 Summary of Work

Patient motion can be differentiated into one of two categories. The first is voluntary motion which includes all types of motion that could be avoided if the patient was completely compliant. The second type is physiological motion which will always be present for clinical invivo MRI regardless of patient compliance.

One type of voluntary motion is described as in-plane rigid body motion. An example might be the motion of the neck if a patient moves their head. In reality, this type of motion accounts for a small fraction of carotid motion artifacts, but is still an important type to consider. The main reason to consider this type of motion is that corrupt data can be corrected rather than thrown out. However, the correction is only feasible if it requires little to no increase is scan time and is not a computational burden on the reconstruction algorithm. Chapter 3 and 4 demonstrated a self-navigating

technique to quantify both translational and rotational in-plane rigid body motion. Both techniques require no additional scan time but do require a modest increase in reconstruction time.

More commonly, carotid motion artifacts are those caused by patient swallowing or other nonrigid body motions (such as head nodding). These artifacts are difficult or impossible to correct and corrupt data is most often simply discarded. The missing data must then be reacquired or calculated using the other acquired data. Chapter 5 demonstrated a self-navigating technique that was able to detect these types of voluntary patient motion. Again, since the technique is self-navigating it requires no additional scan time but does require a modest increase in the reconstruction time.

In most cases, the ability to calculate small amounts of missing data is simple and trying to correct motion-corrupted data may not be feasible. In clinical carotid MRI it may not be feasible to quantify in-plane rigid body motion, but rather employ the technique from Chapter 5 to simply detect when motion has occurred. However, in other applications (such as extremity imaging) rigid-body translations will account for a larger portion of motion artifacts and the techniques of Chapters 3 and 4 would prove very useful.

Even with all voluntary motion accounted for, the pulsatile motion of vessels and blood remains. Rather than correct the corrupt data, one method is to reconstruct a series of images throughout the cardiac cycle which effectively freezes the pulsatile motion in each frame. Analogous to other motion detection techniques, this method is only feasible if it does not require a significant increase in scan time or image reconstruction time. The ability to meet those demands with a TSE sequence was demonstrated in Chapter 6. This

novel cineTSE technique has great implications for carotid imaging applications. First, because the conventional TSE sequence groups data from different phases in the cardiac cycle, objects that move during the cardiac cycle are blurred in the reconstructed image. The cineTSE sequence does not suffer from this because data are grouped over only a short time interval rather than the entire cardiac cycle. Second, the data that most strongly influences the image contrast is acquired at a random time in the cardiac cycle using the conventional TSE sequence. As a result, the conventional TSE sequence can be run twice with the same parameters and produce two different looking images. In particular, one image might show no blood signal in a vessel while another has blood signal present. Since the cineTSE sequence controls when data is acquired in the cardiac cycle, these ambiguities are eliminated. The cineTSE will therefore produce more consistent and reliable images of pulsatile vessels. If one were to ignore the artifacts and consistency problems of the conventional TSE sequence, the cineTSE sequence still offer one important feature. It provides dynamic information unavailable from the conventional TSE images. Even if the conventional TSE sequence happened to produce an artifact free image, it still lacks dynamic information. The cineTSE sequence can provide information about how vessels are moving throughout the cardiac cycle. For example, even if one can detect that there is calcification in a carotid artery (which could be difficult since there is little signal from calcified tissue), no information is available about vessel compliance in the conventional TSE image. But the cineTSE images show how the vessel changes throughout the cardiac cycle and would clearly show how compliant a vessel wall is. Another benefit of cineTSE, as described in the section on future work, is the potential to eliminate the need for blood suppression. These

suppression techniques not only suffer from incomplete blood suppression at times, but serve to increase scan time significantly. However, the ability to discriminate blood in carotid images is an important quality. Residual blood signal that can mimic abnormal carotid wall tissue in conventional TSE sequences, exhibits cyclic intensity variations in the cineTSE images, and can thereby be distinguished from the more constant signal intensity of plaque and artery wall.

Because stroke management in the United States is estimated to range from $35 to $50 billion per year, it is important that the number of non interpretable MR scans be reduced (2). The methods demonstrated in this thesis have a real potential to accomplish this task. The result is not only a reduction in health care costs, but more importantly an increase in the quality and consistency of information available to the clinician caring for the patient.

7.2 Future Work

7.2.1 Elimination of Blood Suppression Methods

Turbo spin echo is an important technique in the discrimination of atherosclerotic plaque components such as hemorrhage, disrupted fibrous cap, lipid/necrotic core, calcification and ulceration. To distinguish between stationary tissue and flowing blood, several techniques such as Double Inversion Recovery (DIR), Quadruple Inversion Recovery (QIR) or Motion-Sensitized Driven-Equilibrium (MDSE) have been proposed (3-5). These suppression techniques involve various combinations of inversion pulses over a large volume outside the slice(s) of interest. This prevents efficient interleaving of multiple slices and results in a dramatic increase in total scan time. It is proposed that analogous information to blood suppression techniques is available with cineTSE without

the need for an increase in scan time over a typical (noninversion prepared) TSE protocol.

In many applications, blood suppression may not be necessary if we can identify blood signal using dynamic information throughout the cardiac cycle. The cineTSE sequence generates a full sequence of cardiac cycle correlated images at each slice location throughout the cardiac cycle in the same scan time that is conventionally used by standard TSE sequences to produce a single image at each slice location. With the cineTSE sequence, magnitude and phase variations of flowing blood during the cardiac cycle are easily distinguishable from surrounding tissue.

Some preliminary data are shown in Fig. 7.1. With informed consent, data for six slices of T1w QIR TSE and T1w cineTSE were acquired before and after Gadolinium contrast injection on one subject using a Siemens Trio 3T MRI scanner with custom designed 16-element phased array surface coils. Data sets are all 256x264, 12 echoes per train, 0.5x0.5x2mm resolution, TR/TE=800/9.2ms and two averages worth of data. For QIR, both inversion delays were 300ms.

The standard T1w TSE images suffer from flow artifacts in both pre and post contrast data sets (arrow in Fig. 7.1). The QIR eliminated most of the flow effects in the pre contrast data, but the postcontrast still had some residual flow, which could be the result of not optimizing inversion times. The QIR will also suffer from some motion artifacts since it is not gated. If the cineTSE images are observed, it is evident that the suspected flow artifact in the T1w images (arrow in Fig. 7.1) is indeed blood signal. The signal is seen to come and go throughout the cardiac cycle. In this case, just a single frame of the cineTSE images (star in Fig 7.1) could be used to distinguish the flow artifact, however,

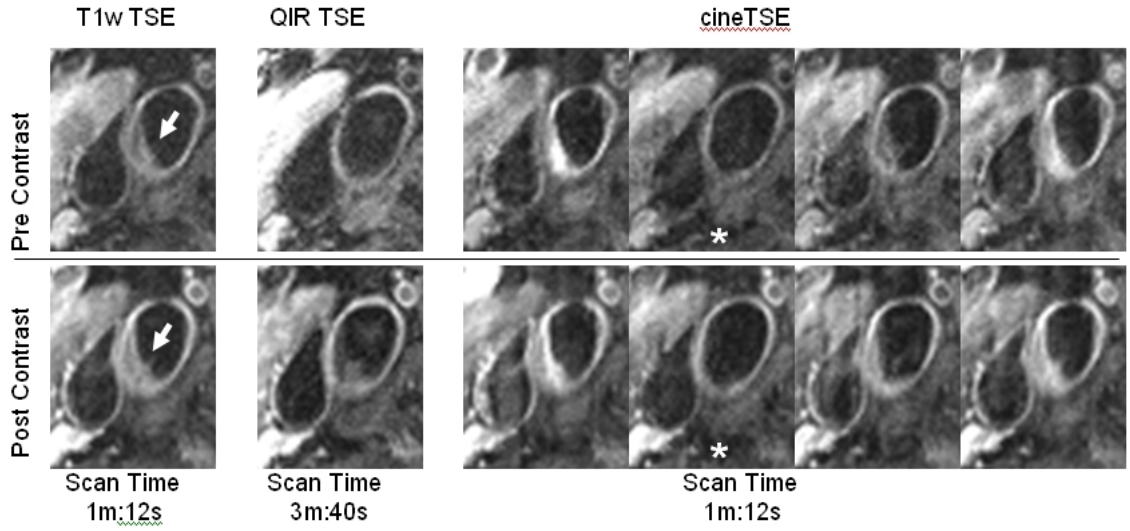

Figure 7.1: 2D TSE images of the common carotid artery before and after contrast. Multihance contrast agent was administered as a rapid bolus at a concentration of 0.1 mmol/kg. Immediately after injection, the cineTSE data was acquired followed by the QIR data. Only 4 (of 12) equally spaced cardiac phases are shown for the cineTSE.

in general the entire dynamic sequence will be necessary. CineTSE has the added benefit of providing tissue information that is not blurred by the cardiac motion. The major benefit in this application is that the acquisition time was about a third of that required for the QIR sequence. The cineTSE sequence can provide analogous information to blood suppression techniques without substantial increases in scan time.

7.2.2 Extension to Other Sequences

Although this thesis focused on a conventional TSE sequence, there are other sequences that would benefit from the basic theory. In addition, only a 2D TSE sequence was investigated in this work. A 3D TSE sequence has proven benefits in carotid imaging, including increased resolution in the slice direction. The main challenge of implementing the techniques on a 3D cineTSE is the computational burden of image reconstruction. To make the implementation clinically feasible, some optimizations need

to be made to the reconstruction algorithms.

7.2.3 Online Implementation

The analysis of data presented in this work was all performed offline. That is, data were acquired on a clinical MRI scanner and then transported to a personal computer where analysis was performed. While this is fine for preliminary results, to be clinically viable, the data needs to be available on the MR scanner a short time after the scan.

7.3 References

1. Wallis de Vries BM, van Dam GM, Tio RA, Hillebrands JL, et al. Current imaging modalities to visualize vulnerability within the atherosclerotic carotid plaque. J. Vasc. Surg. 2008;48:1620-1629.

2. Chu B, Ferguson MS, Underhill H, Takaya N, Cai J, Kliot M, Yuan C, Hatsukami TS. Images in cardiovascular medicine. Detection of carotid atherosclerotic plaque ulceration, calcification, and thrombosis by multicontrast weighted magnetic resonance imaging. Circulation 2005;112:e3-4.

3. Wang J, Yarnykh VL, Hatsukami T, Chu B, Balu N, Yuan C. Improved suppression of plaque-mimicking artifacts in black-blood carotid atherosclerosis imaging using a multislice motion-sensitized driven-equilibrium (MSDE) turbo spin-echo (TSE) sequence. Magn Reson Med 2007;58:973-981.

4. Yarnykh VL, Yuan C. T1-insensitive flow supression using quadruple inversion-recovery. Magn Reson Med 2002;48:899-905.

5. Edelman RR, Chien D, Kim D. Fast selective black blood MR imaging. Radiology 1991;181:655-660.